INVESTIGATION OF MECHANISMS GOVERNING CHARGE TRANSFER IN REDOX–ACTIVE ORGANIC MOLECULES

by

NORA A. SHAHEEN

Submitted in partial fulfillment of the requirements for the degree of Doctor of Philosophy

Thesis Advisor: Professor Rohan Akolkar

Department of Chemical & Biomolecular Engineering

CASE WESTERN RESERVE UNIVERSITY

January, 2023

CASE WESTERN RESERVE UNIVERSITY

SCHOOL OF GRADUATE STUDIES

We hereby approve the dissertation of

Nora A. Shaheen

Candidate for the Doctor of Philosophy degree*

(signed) Rohan Akolkar

(chair of the committee)

Robert F. Savinell

Burcu E. Gurkan

Lydia Kisley

Date of defense: July 28, 2022

*We also certify that written approval has been obtained for any proprietary material contained therein.

Copyright

Parts of this work have been published in the following manuscripts:

1. N. A. Shaheen, M. Ijjada, M. B. Vukmirovic, and R. Akolkar. "Mechanism of Electrochemical Oxidation of Nitroxide Radicals in Ethaline Deep Eutectic Solvent," *J. Electrochem. Soc.*, **167** (2020) 143505. (Chapter 2)

2. N. A. Shaheen, W. Dean, D. Penley, B. Kersten, J. Rintamaki, M. B. Vukmirovic, B. E. Gukan, R. Akolkar. "Electro–Oxidation of Nitroxide Radicals: Adsorption–Mediated Charge Transfer Probed Using SERS and Potentiometry," *J. Electrochem. Soc.*, **169** (2022) 053511. (Chapter 3)

3. N. A. Shaheen, I. Mahesh, M. B. Vukmirovic, and R. Akolkar. "Hysteresis effects and roughness suppression efficacy of polyethylenimine additive in Cu electrodeposition in ethaline," *Electrochem. Commun.*, **115** (2020) 106721. (Appendix A)

Dedication

For my Teta who spoke life into this dissertation,
my Seedo for sacrificing everything for his children and grandchildren,
my Teta who never failed to ease stress away with a tearful belly laugh,
and my Jedo for always making sure I had my chocolate fix, and
for Emma and Layla, for introducing a new dimension of joy to my life.

I love you.

Table of Contents

List of Tables

List of Figures

Acknowledgements

I first wanted to say alhamdillah for the opportunity to share my Ph.D. research with the broader scientific community. I would like to also thank the DOE for funding this research through the BEES–EFRC and the SCGSR fellowship.

I am immensely fortunate for the mentorship and guidance I have received from my advisor, Professor Rohan Akolkar over the last 4 years. He challenged me to be a critical and independent scientist, as well as a compassionate mentor. He truly invests the effort into teaching his students concepts and fundamentals, mentoring them, and advocating for their success.

I would also like to sincerely thank a former professor and good friend of mine, Dr. John D. Clay, for investing the time in mentoring me over the last 8 years. I will never forget: steam tables, Cox charts, Antoine's equation, and Henry's law. Thank you for everything.

Also integral to my professional growth are my mentors at Argonne National Laboratory: Drs. Venkat Srinivasan, Lynn Trahey, Zhenzhen Yang, and Emily Carino. A sincere thank you should also be extended to members of the Energy Conversion and Storage Group, and in particular Dr. Pietro P. Lopes for his support.

I would also like to acknowledge current and former members of the EMF laboratory at Case: Bethany, Ruwani, Theodore, Badri, Vaishnavi, Roland, Ben, Dai, Adam, Kailash, Xinyu (Sherry), Yan, Mahesh, Yukun (Jack), and Katie. I am also grateful for the professors and graduate students in the Department of Chemical & Biomolecular Engineering at Case Western Reserve University for fostering a strong sense of community.

I want to thank my parents, who as immigrants, have done so much for me. My dad, the O.G. Dr. Shaheen who fled the violence of 2nd Nakba, taught me the value of hard work and perseverance; and my mother, who spent countless hours with me practicing concepts and presentations, taught me much more than written words can express. I love you both dearly. I suppose I should also acknowledge my siblings: Mahdey, Nadia (also my illustrator), Tareck, Josie and Shahn, and my two precious nieces, Emma and Layla. Also a big part of the cheerleading club is my family in Jordan and Canada, especially my Tetas and Seedo who I miss deeply, and my Jedo who always checks in on my research. This thesis is for them.

Last, but not least, I want to extend a heartfelt appreciation to my closest friends for all the love and support they have given me: Bethany, Mickey, Anjelica, Mike, Jeff, Jacob, Nick, Evan, Solo, Laura, and Maura.

It takes a village to reach such a milestone, and I am indebted to my village for being the best support system I could have asked for.

List of Symbols

C	Concentration, mM
D	Diffusion coefficient, $\mathrm{cm^2\ s^{-1}}$
E_{eq}	Equilibrium potential, V
E_{i}	Initial potential, V
$E_{\mathrm{p}}^{\mathrm{a}}$	Anodic peak potential, V
F	Faraday's constant ($96485\ \mathrm{C\ mol^{-1}}$)
g	Interaction parameter
I	Current, A
i	Current density, $\mathrm{mA\ cm^{-2}}$
i_1	Current density in step 1 (Chapter 3), $\mathrm{mA\ cm^{-2}}$
i_{L}	Limiting current density, $\mathrm{mA\ cm^{-2}}$
$i_{\mathrm{p}}^{\mathrm{a}}$	Anodic peak current density, $\mathrm{mA\ cm^{-2}}$
i_0	Exchange current density, $\mathrm{mA\ cm^{-2}}$
i_{k}	Kinetic current density, $\mathrm{mA\ cm^{-2}}$
$\mathrm{K_{eq}}$	Equilibrium rate constant, $\mathrm{cm^3\ mol^{-1}}$
k_{des}	Desorption rate constant, $\mathrm{mol\ cm^{-2}\ s^{-1}}$
k_0	Heterogeneous rate constant, $\mathrm{cm\ s^{-1}}$
m_{diff}	Diffusion–limited slope, V
m_{des}	Desorption–limited slope, V
n	Number of electrons
P_{ads}	Passivating product adsorbed to electrode
R_Ω	Ohmic resistance, Ω
R	Universal gas constant ($8.314\ \mathrm{J\ mol^{-1}\ K^{-1}}$)
R_{u}	Reactant
r	Electrode radius, cm
r_{ox}	Rate of oxidation
r_{red}	Rate of reduction
V	Voltage, V
x	Distance, cm
t	Time, s
t^*	Time, dimensionless
T	Temperature, K

Greek

α	Charge transfer coefficient
δ	Diffusion boundary layer thickness, cm
η_s	Surface overpotential, V
θ	Fractional surface coverage of HT^+
κ	Electrolyte conductivity, mS cm^{-1}
μ	Viscosity, cP
υ	Scan rate, V/s
ρ	Density, g cm^{-3}
ω	RDE rotation speed, rad s^{-1}

Subscripts

a	Anodic
ads	Adsorbed
b	Bulk
c	Cathodic
diff	Diffusion
des	Desorption
eq	Equilibrium
HT	4–hydroxy–TEMPO
k	Kinetic
L	Limiting
ox	Oxidation
p	Peak
red	Reduction
ref	Reference
0	Initial
1	Step 1
3+	$FeCl_3$

Investigation of Mechanisms Governing Charge Transfer in Redox–Active Organic Molecules

Abstract

by

NORA A. SHAHEEN

Organic compounds containing nitroxide radicals such as 4–hydroxy–2,2,6,6–tetramethylpiperidine–1–oxyl (4–hydroxy–TEMPO) are redox–active and are of interest for potential applications in redox flow batteries. The mechanisms governing charge–transfer reactions of such compounds are not well understood. Specifically, the anodic charge transfer coefficient (α_{a}) corresponding to the electro–oxidation of 4–hydroxy–TEMPO in an aqueous and non–aqueous electrolyte is ~ 0.9, *i.e.*, α_{a} deviates considerably from the expected value (0.5) for a symmetric single–step one–electron transfer redox reaction. To explain this observation, a two–step oxidation mechanism is proposed wherein the nitroxide–containing species undergo fast charge transfer at an electrode surface followed by slow rate–limiting desorption of the adsorbed oxidized species. Numerical simulations are reported to characterize how the proposed two–step mechanism manifests in transient cyclic voltammetry behavior of the 4–hydroxy–TEMPO oxidation reaction, and good agreement with experiments is noted.

In the present contribution, supporting evidence is provided for the aforementioned mechanism. *In situ* surface–enhanced Raman spectroscopy is employed to confirm the presence of surface–adsorbed species at a Au electrode during electro–oxidation of 4–

hydroxy–TEMPO. Furthermore, chronopotentiometry is used to track the gradual re–equilibration of the electrode–electrolyte interface following the electro–oxidation of 4–hydroxy–TEMPO. Analysis of the chronopotentiometry data further suggests the presence of adsorbed species. Electrochemical cycling and spectroscopic evidence are presented to investigate the passivating effect of surface films that form following the electro–oxidation of 4–hydroxy–TEMPO.

1.1. Motivation: High energy density redox–flow batteries

As the effects of climate change intensify and geopolitical instability threatens global energy supplies, there is an urgent need to decarbonize the electric grid through renewable energy such as wind and solar. Load–leveling devices such as redox flow batteries (RFBs) to mitigate the intermittency of renewable energy sources. In a RFB (charging cycle illustrated in **Fig. 1.1**), the positive and negative electrolytes are stored in external tanks and pumped through the electrode compartments to facilitate the appropriate redox reaction. This allows for the decoupling of power (controlled by electrode area) and energy (controlled by the concentration of electro–active species).[1]

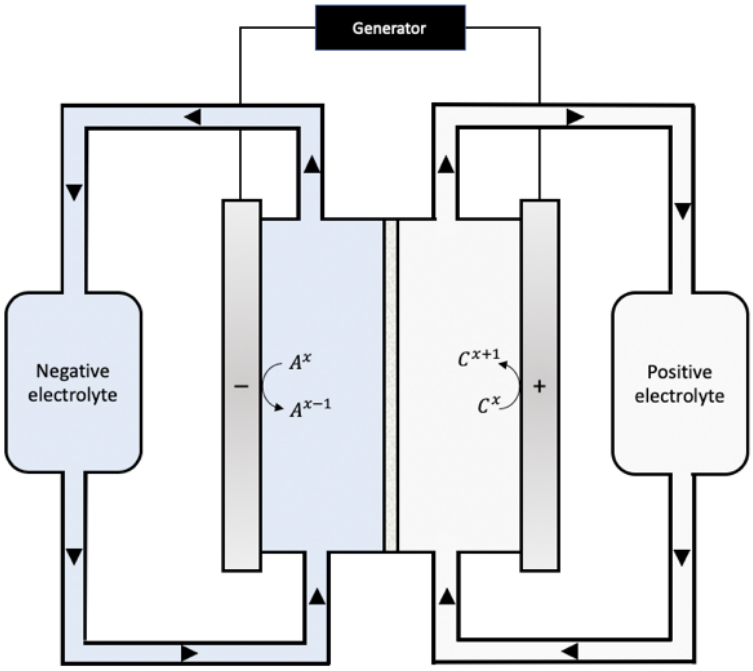

Figure 1.1. Schematic representation of a redox flow battery during the charge cycle.

A variety of chemistries have been considered for RFB applications, including iron/chromium (Fe/Cr),[2,3] zinc/bromine (Zn/Br),[4] and all–vanadium.[5–7] However, widespread commercial adoption of these chemistries is limited for a variety of reasons. For example, the sluggish kinetics of the Cr redox reaction lowers the energy efficiency of Fe/Cr RFBs;[1] the relatively low open circuit potential of the Zn/Br RFBs (~1.7 V) and limited solubility of V in all-vanadium RFBs further hinders achieving high energy density.

Redox–active organic molecules (ROMs) have gained increasing attention as electro–active materials for RFBs.[8–13] Chemical and electrochemical properties of ROMs, *i.e.*, their solubility, redox potential, and chemical stability can be tailored through molecular engineering of the base molecule.[14–16] Nitroxide–radical containing ROMs such as 2,2,6,6–tetramethylpiperidine–1–oxyl (TEMPO) are known to be stable under ambient conditions due to the resonance across the $N-O^{\cdot}$ moiety and the steric protection offered by nearby functional groups.[17,18]

1.2. Previous work

1.2.1. Electrochemical investigations of nitroxide–containing ROMs

TEMPO–based ROMs have been the focus of extensive electrochemical investigations in both aqueous[9,14,15,19] and non–aqueous[11,16,20–22] electrolytes. In 2016, Liu et al.[9] reported on the oxidation of 4 mM of 4–hydroxy–2,2,6,6–tetramethylpiperidine–1–oxyl (4–hydroxy–TEMPO, abbreviated here as 'HT') as a catholyte in a flow battery. Through cyclic voltammetry, they showed that the oxidation of HT is a reversible reaction. Further studies by Suga et al.[17] reported a relatively high standard rate constant for TEMPO

in acetonitrile (on the order of $\sim 10^{-2}$ cm s^{-1}). Wei et al.[22] reported that the oxidation and reduction of TEMPO/$TEMPO^+$ is a reversible one–electron transfer reaction. However, fundamental understanding of mechanisms governing charge transfer of TEMPO–based ROMs is limited, particularly at high concentrations needed for practical flow battery applications.

1.2.2. Unusual α: analogies to gas evolution reactions

Numerous studies have investigated electrochemical reactions involving gas evolution.[23–28] For brevity, only the case of the hydrogen evolution reaction (HER) is presented wherein the hydronium ion is reduced through the Volmer–Tafel mechanism:

$$\text{(Volmer)} \qquad H_3O^+ + e^- + S \rightleftharpoons S-H + H_2O \qquad [1.1]$$

$$\text{(Tafel)} \qquad 2S-H \rightleftharpoons H_2 + 2S \qquad [1.2]$$

where S denotes a vacant site on the electrode.

When the electron–transfer step is rate determining (reaction 1.1), electrochemical kinetics may be reliably extracted using classical rate equations, *i.e.*, the Butler–Volmer equation or the Tafel approximation. However, when the rate determining step does not involve electron–transfer (reaction 1.2), a new rate expression must be derived. In the Volmer–Tafel case, a coverage–dependent rate expression has been derived wherein the apparent value of $\alpha = 1$.[27] In Chapter 2 of this thesis, an analogous mechanism is proposed to explain $\alpha \to 1$ for the electrochemical oxidation of a model TEMPO–based ROM: 4–hydroxy–TEMPO (HT).

1.3. Brief introduction to deep eutectic solvents

Deep eutectic solvents (DESs) are a new class of electrolytes that have gained attention for their potential applicability as electrolytes in large–scale energy storage applications such as flow batteries.[29–31] These electrolytes are formed by mixing a hydrogen bond donor and acceptor at a eutectic ratio such that the mixture exhibits freezing point depression ΔT_f,[32] rendering it liquid–like at room temperature (**Fig. 1.2**). As electrolytes in flow batteries, DESs offer several advantages over traditional organic and ionic liquid electrolytes including superior environmental friendliness,[32] low–cost,[33,34] large electrochemical stability window,[35] and non–flammability.[30] However, despite these advantages, technological applications of DESs are rather limited because they typically possess high viscosity and thus low ionic conductivity and diffusivity.

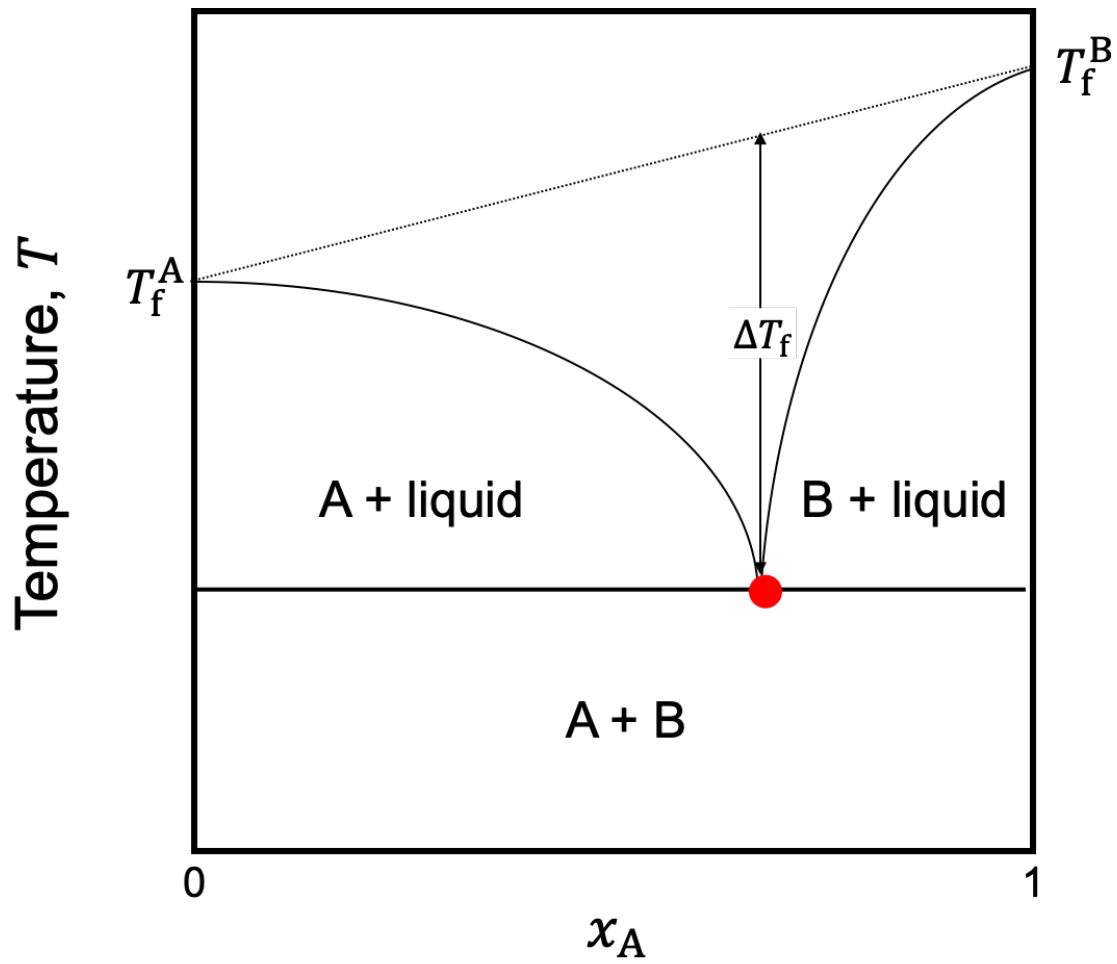

Figure 1.2. Schematic representation of a deep eutectic solvent phase diagram. Two components A and B are mixed at a eutectic ratio (*red*) such that the mixture exhibits a freezing point depression ΔT_f. Figure modified from Ref. 32.

Ethaline, a widely investigated DES, is formed by mixing choline chloride (ChCl) and ethylene glycol (EG) in a 1:2 molar ratio. This DES contains approximately 4.5M ChCl and 9M EG. Relative to other DESs, ethaline has rather low viscosity (~50 cP) and high ionic conductivity (8 mS cm^{-1}) at room temperature.[16] A variety of electroactive species can be dissolved in ethaline to facilitate redox reactions at the electrode–electrolyte interface. To date, substantial work has been conducted on characterizing electrochemical reactions involving inorganic redox species in ethaline[30,36–42] with only very few

publications discussing the behavior of organic redox–active species.[43] In Chapter 2 of this thesis, a thorough electrochemical study is presented of HT electro–oxidation in ethaline.

1.4. Objectives

The objectives of this work are to:

1. Develop a deeper understanding of the mechanism of electrochemical oxidation of a model ROM, *i.e.*, HT, by extracting kinetic parameters from pseudo steady–state voltammograms collected on a rotating disk electrode and microelectrode;
2. Present supporting evidence for the proposed mechanism involving a surface adsorbed species through a combination of electrochemical, and spectroscopic evidence; and
3. Characterize the chemical structure of the surface film that passivates the electrode using electrochemical experiments, optical imaging, and spectroscopy.

Discussions of these objectives can be found in Chapters 2–5 followed by a summary of the key conclusions and future outlook in Chapter 6.

In Chapter 2, the anodic charge transfer coefficient α_{a} corresponding to the electrochemical oxidation of HT was determined using a variety of analysis methods: Tafel, Koutecky–Levich, and the extended Butler–Volmer[44] equations. An adsorption–mediated and desorption–limited mechanism is proposed to explain the deviation of $\alpha_{\mathrm{a}}(\rightarrow 1)$ from the expected value of 0.5 for a symmetric, one–electron reaction involving a soluble–soluble transition.[45–47]

In Chapter 3, a two–step electrochemical technique is used to probe the electrode–electrolyte interface and confirm the presence of surface–adsorbed species. The results of this technique are discussed in the context of two cases: (i) diffusion–limited ($FeCl_2/FeCl_3$), and (ii) desorption–limited (HT/HT^+). At short time scales, the slope of the potential–transient for case (ii) is lower than the predicted slope of case (i). At long time scales, the potential returns to the open circuit potential at a much longer time scale than the diffusion–limited case. The electrochemical data is supported with spectra collected using *in situ* surface enhanced Raman spectroscopy.

In Chapter 4, evidence of a surface passivating film is presented using electrochemical cycling and steady–state amperometry. The chemical structure of the film is characterized through Fourier transform infrared spectroscopy.

Chapter 2. Mechanism of electrochemical oxidation of nitroxide radicals in ethaline deep eutectic solvent

---

As previously discussed, ROMs containing nitroxide radicals have gained increasing attention as redox–active materials in electrochemical energy storage technologies. In this chapter, a model electrochemical reaction (Eq. 2.1) is investigated wherein 4–hydroxy–TEMPO (HT) is oxidized to the corresponding oxoammonium cation (HT^+). The reaction is studied at low (50 mM) and high (200 mM) concentrations, and in aqueous and organic electrolytes.

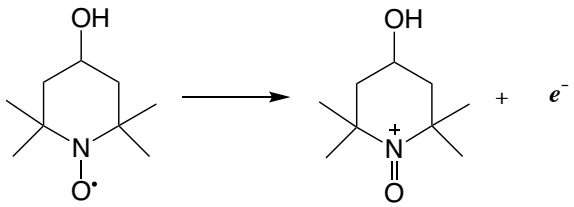

HT HT^+ [2.1]

In this chapter, the charge transfer coefficient (α_a) corresponding to reaction 2.1 is shown to significantly deviate from the expected value of 0.5 for symmetric single–step one–electron transfer redox reaction involving a soluble–soluble transition.[45–47] Steady–state polarization measurements on a Pt rotating disk electrode (RDE) and on a micro–electrode confirm that α_a deviates significantly from 0.5 and approaches values of ~0.9 in aqueous and non–aqueous electrolytes. To explain this deviation, a mechanistic model is presented here incorporating surface adsorption and desorption of intermediate species during the oxidation process. Implications of the proposed model to transient electrochemical measurements, *i.e.*, fast–scan voltammetry, are discussed and model

predictions are compared to experimental cyclic voltammetry (CV) data for high (200 mM) and low (50 mM) concentrations of HT in ethaline.

2.1. Experimental procedure

2.1.1. Materials

Choline chloride (ChCl, 99% purity, Acros Organics), ethylene glycol (EG, anhydrous, 99.8% purity, Sigma–Aldrich), sodium chloride (NaCl, ≥ 99% purity, Sigma Aldrich), 4–hydroxy–TEMPO (HT, $C_9H_{18}NO_2$, > 98% purity, Alfa Aesar), potassium ferricyanide ($K_3Fe(CN)_6$, > 99% purity, Acros Organics), and potassium ferrocyanide trihydrate ($K_4Fe(CN)_6 \cdot 3H_2O$, 98.5% purity, Acros Organics) were used as received. Ethaline was prepared by mixing ChCl and EG in a 1:2 molar ratio at 80°C until a homogeneous, colorless solution was obtained. The solution was then allowed to cool to room temperature. Solutions of HT (50 mM and 200 mM) in ethaline were prepared by adding appropriate amounts of HT to the freshly prepared DES. Aqueous solutions of $K_3Fe(CN)_6$ + $K_4Fe(CN)_6$ (10 mM each), and HT (50 mM) in 500 mM $NaCl_{aq}$ were prepared using Millipore ultrapure (18.2 MΩ · cm) deionized water.

2.1.2. Methods

Experiments were performed using a water–jacketed, glass–body electrochemical cell. Electrolyte temperature was maintained at 25 ± 0.5 °C. The aqueous solutions were de–aerated by purging Ar gas while ethaline–based electrolytes were not de–aerated. Absence of de–aeration in DES electrolytes did not alter experimental results as was confirmed by comparing voltammetry results in control experiments performed with and

without de–aeration. A standard three–electrode configuration was used. The working electrode was a 5 mm diameter polycrystalline Pt rotating disk electrode (RDE, Pine Research Instrumentation). Experiments were also carried out on a stationary 10 μm diameter Pt micro–electrode (BASi MF–2005) as the working electrode. For experiments in ethaline–based solutions, Ag/AgCl reference electrode was used. The reference electrode was prepared by anodizing Ag wire (99.9% purity, Sigma–Aldrich) in ethaline following the procedure described by Shen et al.[37] For experiments in aqueous solutions, Ag/AgCl in 3 M KCl was used as the reference electrode. The counter electrode was a graphite rod. A Princeton Applied Research PARSTAT–4000 potentiostat was used for all experiments. The voltammetric curves shown below were recorded immediately after the Pt electrode was immersed into the electrolyte solutions, *i.e.*, they present results of the first scan in linear sweep voltammetry or fast–scan CV experiments. Slow–scan linear sweep voltammetry curves were recorded by scanning the potential in the anodic direction at a scan rate of 1 mV/s to minimize transient effects and to maintain pseudo steady–state conditions.

On RDE, voltammetry was performed at various rotation speeds in the range 100 – 900 RPM. From these measurements, anodic transfer coefficients were extracted through Tafel analysis (section 2.2.1), Koutecky–Levich analysis (section 2.2.2), and the extended Butler–Volmer[44] equation (section 2.2.3). CV curves were recorded on RDE at rotation speeds in the 500 – 1500 RPM range. The ohmic resistance R_Ω for each electrolyte and cell configuration was measured using electrochemical impedance spectroscopy. On RDE, R_Ω for the DES was 103 Ω and that for aqueous electrolyte was

15 Ω. IR_Ω–correction was applied to all steady–state polarization data during post–processing; however, CV data was acquired under conditions of "live" IR_Ω–compensation.[30]

2.2. Determination of the anodic transfer coefficient

2.2.1. Tafel analysis

To gain insights into the mechanisms underlying electrochemical reaction 2.1 above, slow–scan voltammetry was performed and provided pseudo steady–state polarization curves (**Fig. 2.1**). The anodic charge transfer coefficient α_a was extracted according to the Tafel equation:

$$i = i_0 \left(1 - \frac{i}{i_\mathrm{L}}\right) \exp\left(\frac{\alpha_\mathrm{a} F}{RT} \eta_\mathrm{s}\right) \qquad [2.2]$$

where i, i_0 and i_L are the measured, exchange and diffusion–limited current densities, respectively and η_s is the overpotential ($= V - IR_\Omega - E_\mathrm{eq}$). Here, the measured current density i represents the current per unit projected surface area of the electrode, and the diffusion–limited current density i_L corresponds to the limiting current plateau seen in **Fig. 2.1**.

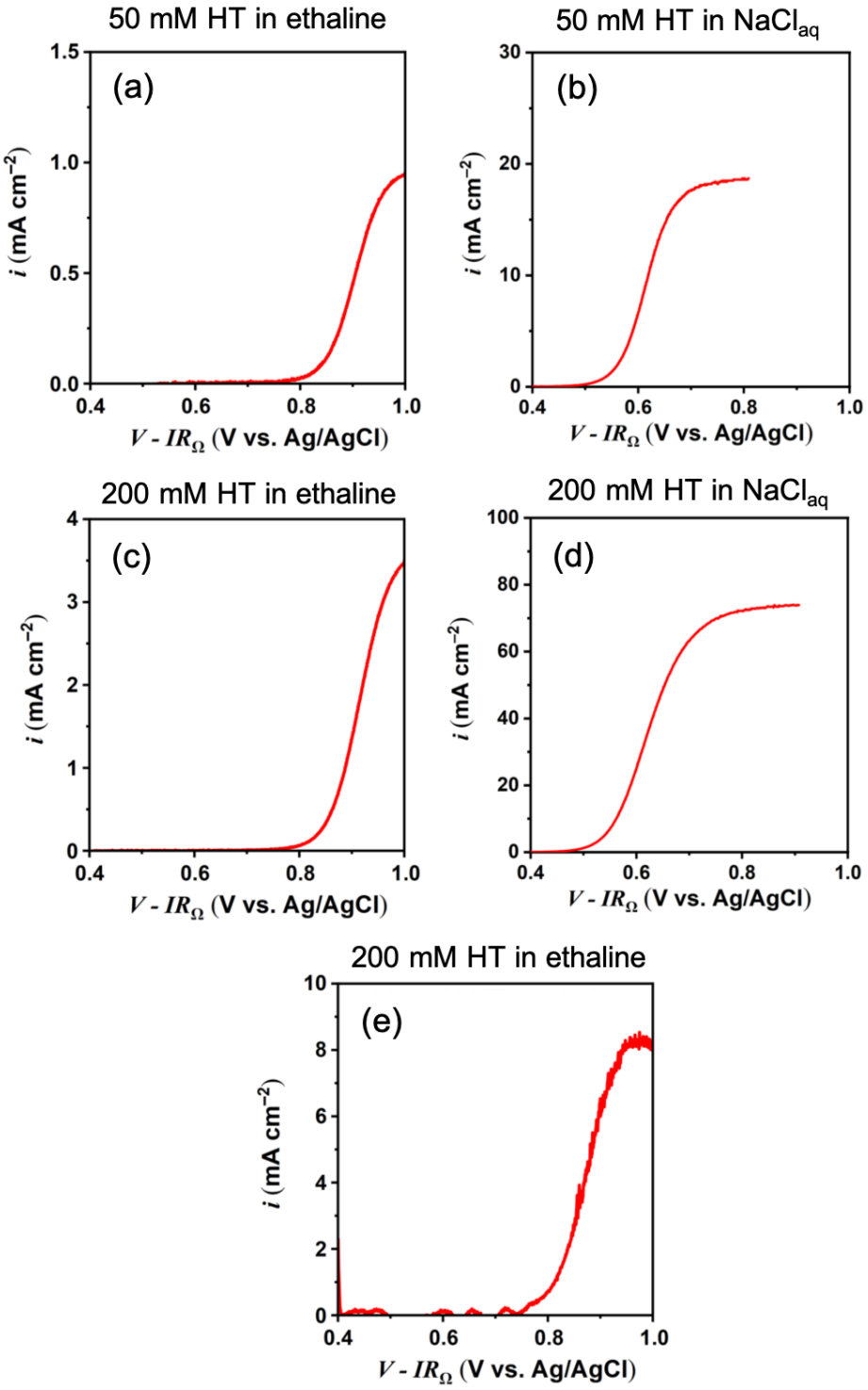

Figure 2.1. Polarization scans for HT oxidation collected on (a – d) a Pt RDE at 900 RPM and (e) a Pt microelectrode. The electrolytes contained: (a) 50 mM HT in ethaline, (b) 50 mM HT in 500 mM $NaCl_{aq}$, (c, e) 200 mM HT in ethaline and (d) 200 mM HT in 500 mM $NaCl_{aq}$. Data was collected at 25°C.

Tafel plots (**Fig. 2.2**) were generated where the "kinetic" current densities $i_{\mathrm{k}} = i \cdot [i_{\mathrm{L}}/(i_{\mathrm{L}} - i)]$ were plotted versus $V - IR_{\Omega}$. Under Tafel kinetics, semi–log plots of i_{k} versus $V - IR_{\Omega}$ must show linearity because:

$$\log_{10} i_{\mathrm{k}} = \log_{10} i_0 + \left[\frac{\alpha_{\mathrm{a}} F}{2.303RT}\right](V - IR_{\Omega} - E_{\mathrm{eq}}) \qquad [2.3]$$

It should be noted that the current range where Tafel behavior was observed is well below the limiting current i_{L}. Thus, $i \approx i_{\mathrm{k}}$ and mass–transport effects are negligibly small. From the Tafel slope, the anodic charge transfer coefficients (α_{a}) were determined for each condition tested. For a more direct comparison between aqueous electrolytes and their chloride–rich DES counterparts, we specifically chose to prepare aqueous electrolytes with high (500 mM) chloride concentration.

In experiments with Pt RDE, care was taken to ensure that the current distribution on the RDE was relatively uniform.[30] For electrolyte conductivity of ≈ 8 mS cm^{-1}, RDE radius of 0.25 cm, and an average current density of 1 mA cm^{-2}, the Wagner number (Wa) was estimated to be about 1.2; indicative of acceptably (but not highly) uniform current distribution. However, to be certain that current distribution effects do not introduce errors, we resorted to measurements of kinetics parameters using a micro–electrode, which provides a highly uniform secondary current distribution.[30]

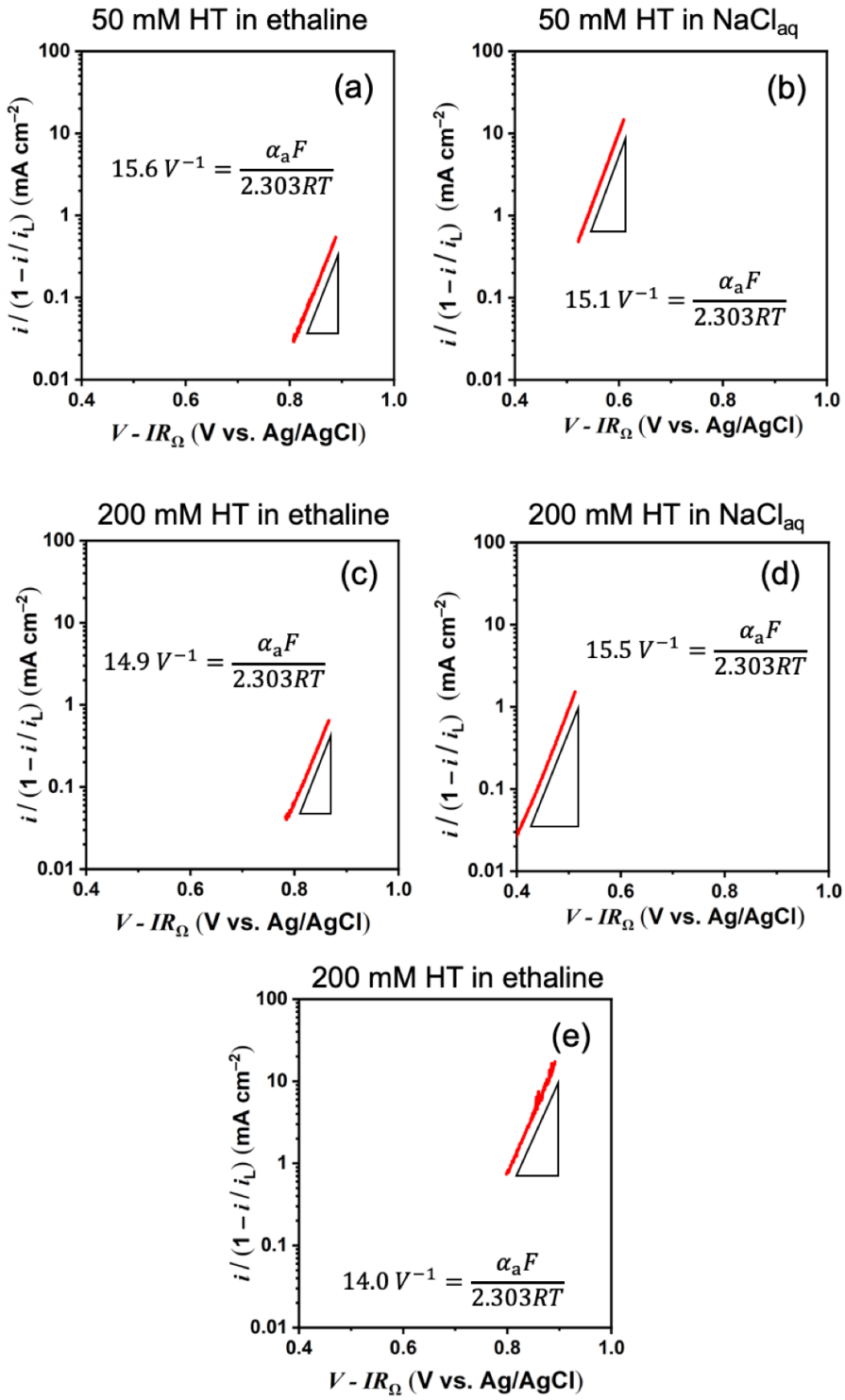

Figure 2.2. Tafel plots for HT oxidation collected on (a – d) a Pt RDE at 900 RPM and (e) a Pt microelectrode. The electrolytes contained: (a) 50 mM HT in ethaline, (b) 50 mM HT in 500 mM NaCl$_{aq}$, (c, e) 200 mM HT in ethaline, and (d) 200 mM HT in 500 mM NaCl$_{aq}$. In each case, the value of α_a deviates from the expected value of 0.5 and approaches unity

2.2.2. Koutecky–Levich analysis

Koutecky–Levich analysis was used to further confirm the unusual values of α_a measured in section 2.2.1. For brevity, only the case of low HT concentration (50 mM) in ethaline is presented here. On the RDE, steady–state voltammograms were collected at various rotation speeds in the range of 100 – 900 RPM (**Fig. 2.3**).

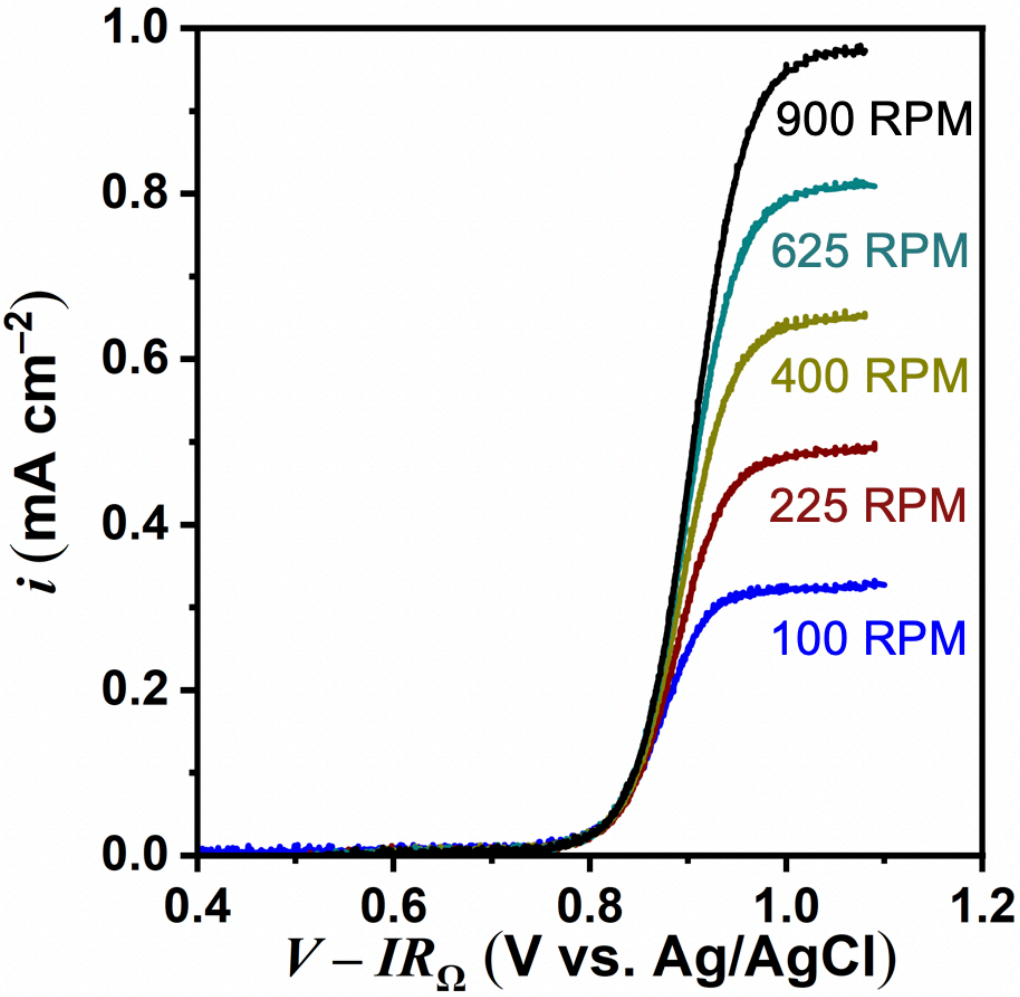

Figure 2.3. Slow–scan (1 mV/s) linear sweep voltammograms of 50 mM HT in ethaline DES collected on a Pt rotating disk electrode (various rotation speeds ω).

Under steady–state conditions, the kinetic and diffusion–limited current densities (i_{k} and i_{L}) contribute to the measured current density i according to the Koutecky–Levich equation:[48]

$$\frac{1}{i} = \frac{1}{i_{\mathrm{k}}} + \frac{1}{i_{\mathrm{L}}} \qquad [2.4]$$

Thus, a plot of i^{-1} versus $\omega^{-1/2}$ is linear because:

$$\frac{1}{i} = \frac{1}{i_{\mathrm{k}}} + \frac{1}{0.62\, nFD_{\mathrm{HT}}^{2/3} \left(\frac{\mu}{\rho}\right)^{-1/6} C_{\mathrm{b}}\, \omega^{1/2}} \qquad [2.5]$$

where n is the number of electrons participating in the reaction, F is Faraday's constant, D_{HT} is the diffusion coefficient of HT in ethaline (refer to **Fig. B.1**), μ and ρ are the viscosity and density of ethaline, respectively. The bulk concentration of HT is given by C_{b}, and the RDE rotation speed is ω. **Fig. 2.4** shows values of i^{-1} versus $\omega^{-1/2}$ at various overpotentials. It is important to note that the slope of the curves in **Fig. 2.4** is independent of the applied overpotential, as expected for an irreversible redox reaction.

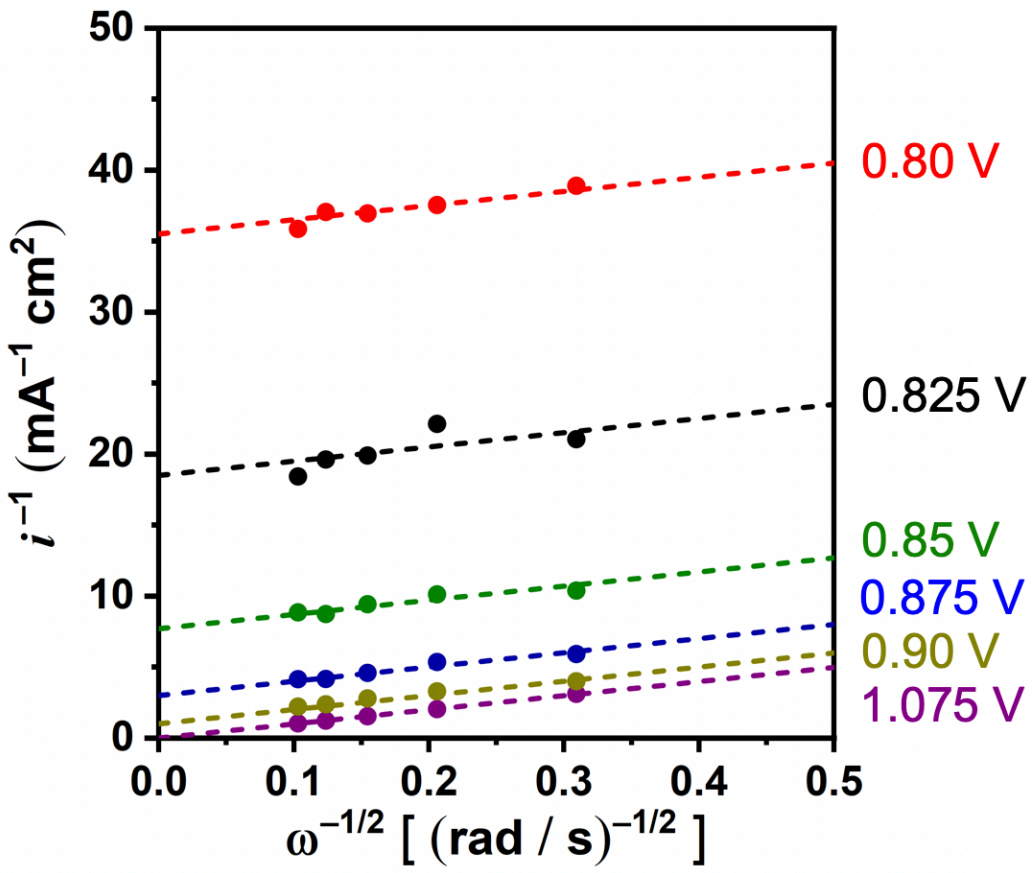

Figure 2.4. Koutecky–Levich plot of the inverse current density i^{-1} versus the inverse square root of RDE rotation speed $\omega^{-1/2}$. The y–intercept of each curve corresponds to i_k^{-1}, and is used for the analysis shown in **Fig. 2.5.**

The kinetic current density can be read directly from the y–intercept of the dashed curves in **Fig. 2.4**. The kinetic current density i_k can be defined as,[49]

$$i_k = Fk_0C_b \exp\left[\frac{\alpha_a F}{RT}\left(V - IR_\Omega - E_{eq}\right)\right] \quad [2.5]$$

where k_0 is the standard rate constant. Rearranging Eq. 2.5:

$$2.303[\log_{10} i_{\mathrm{k}} - \log_{10}(Fk_0C_{\mathrm{b}})] = \frac{\alpha_{\mathrm{a}}F}{RT}\left(V - IR_{\Omega} - E_{\mathrm{eq}}\right) \quad [2.6]$$

Thus, a semi–log plot of i_{k} versus $V - IR_{\Omega}$ may be generated (**Fig. 2.5**). From the slope, the anodic charge transfer coefficient α_{a} was calculated $= 0.92$. This is in excellent agreement with the value of α_{a} calculated in section 2.2.1 using Tafel analysis.

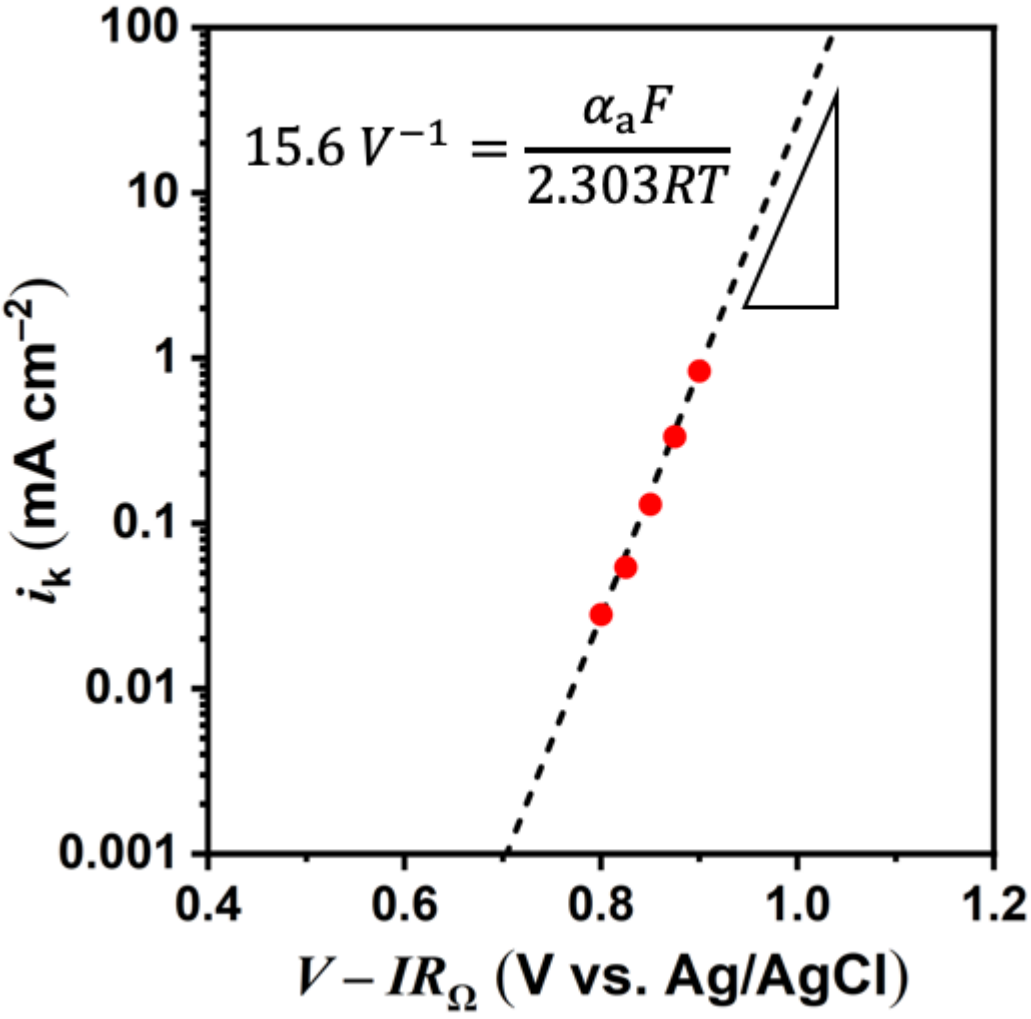

Figure 2.5. Semi–log plot of i_{k} versus $V - IR_{\Omega}$ for 50 mM HT in ethaline DES. The Tafel slope, and therefore α_{a}, is in excellent agreement with that provided by Tafel analysis shown in **Fig. 2.2**.

2.2.3. Full Butler–Volmer equation

In 2021, Shen et al.[44] reported on the electrochemical kinetics of the Fe^{3+}/Fe^{2+} redox reaction in ethaline DES. They show that use of the Tafel approximation may lead to erroneous kinetic parameters when i_L is low, such as in the case of deep eutectic solvents. To ensure the validity of α_a values calculated in sections 2.2.1 and 2.2.2, experimental voltammograms were fit with the full Butler–Volmer equation (Eq. 2.7):

$$i = \frac{\exp\left[\frac{\alpha_a nF}{RT}\eta_s\right] - \exp\left[-\frac{(1-\alpha_a)nF}{RT}\eta_s\right]}{\frac{1}{i_0} + \frac{1}{i_L^a}\exp\left[\frac{\alpha_a nF}{RT}\eta_s\right] - \frac{1}{i_L^c}\exp\left[-\frac{(1-\alpha_a)nF}{RT}\eta_s\right]} \quad [2.7]$$

Fig. 2.5 compares experiment (*red*) to simulated voltammograms for two cases of α: 0.5 (*blue*) and 0.92 (measured value from 2.2.1 and 2.2.2 – *black*). Here, E_{eq} is assumed as the onset potential ($\sim$0.7 V vs. Ag/AgCl), *i.e.*, when anodic current is first observed. Additionally, the magnitude of i_L^a and i_L^c are assumed to be equal ($\sim$0.98 mA cm^{-2}), and i_0 ($= 8 \times 10^{-4}$ mA cm^{-2}) is treated as a fitting parameter. Excellent agreement is noted between experiment and simulated voltammetry when $\alpha = 0.92$. However, it is important to note that the simulated voltammograms have multiple adjustable parameters (E_{eq}, α_a, and i_0). Nevertheless, it is clear that the value of the anodic charge transfer coefficient associated with reaction 2.1 deviates from the expected value of 0.5.

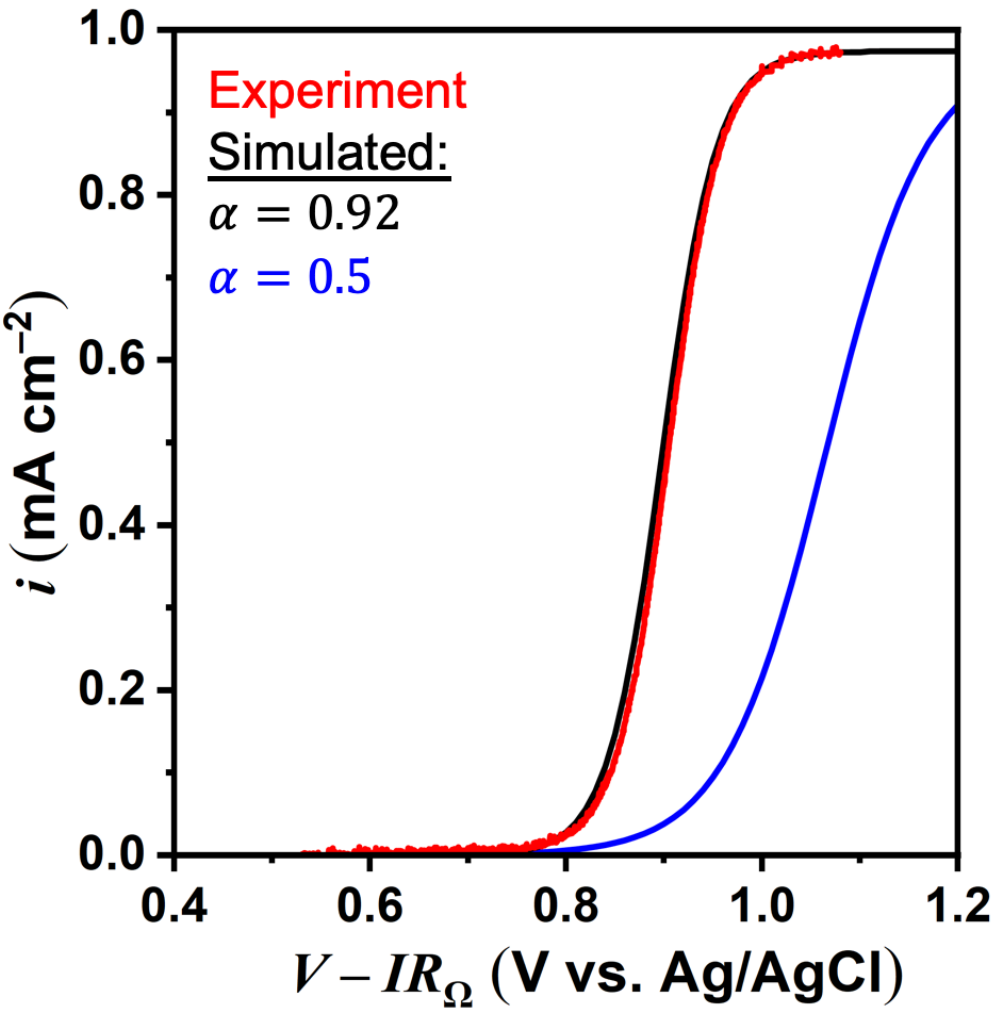

Figure 2.6. Experimental (*red*) and simulated (*black* and *blue*) slow–scan voltammetry of 50 mM HT in ethaline. Experimental data was collected on a Pt RDE rotating at 900 RPM. Scan rate was 1 mV/s. The reference electrode was a passivated Ag wire calibrated against Ag/AgCl and the counter electrode was a graphite rod. Each simulated voltammograms was produced by assuming E_{eq} = 0.7 V vs. Ag/AgCl and $i_0 = 8 \times 10^{-4}$ mA cm^{-2}. Excellent agreement between experimental data and simulated polarization curve is noted when α_a = 0.92.

Table 2.1 summarizes the anodic charge transfer coefficients determined for reaction 2.1 in ethaline and in an aqueous medium for $C_b = 50$ or 200 mM. As seen in

Table 2.1, the high value of α_a $(= 0.92 \pm 0.03)$ was reproducible in polarization measurements on a macro–and micro–electrode, analysis technique (Tafel, Koutecky–Levich, and full Butler–Volmer equation), and electrolyte.

Table 2.1. Summary of the measured anodic charge transfer coefficients for HT oxidation using a variety of measurement and analysis techniques.

Measurement technique	Analysis technique	Electrolyte	C_b	α_a
RDE	Tafel	500 mM $NaCl_{aq}$	50 mM	0.89
RDE	Tafel	500 mM $NaCl_{aq}$	200 mM	0.92
RDE	Tafel	Ethaline	50 mM	0.92
RDE	Koutecky–Levich	Ethaline	50 mM	0.92
RDE	Butler–Volmer	Ethaline	50 mM	0.92
RDE	Tafel	Ethaline	200 mM	0.88
Micro–electrode	Tafel	Ethaline	200 mM	0.83

2.3. Adsorption–Desorption model and the apparent transfer coefficient

As previously mentioned, many electrochemical reactions including gas–evolution[50,51] reactions and the oxidation of organic acids[52,53] occur via adsorbed intermediate species. In studies of such processes, the effects of adsorption or desorption of reactants and products on charge transfer kinetics, specifically the apparent charge transfer coefficient of an electrochemical reaction, have been widely discussed in the literature.[27] Here, we propose that HT oxidation reaction represented by Eq. 2.1 follow two elementary steps as shown schematically in **Fig. 2.7:**

(i) Electron transfer followed by adsorption of the oxidation product (oxoammonium cation);

(ii) Desorption of the adsorbed oxoammonium cation back into the electrolyte.

This two–step process collectively is referred to below as "adsorption–desorption" during charge transfer. Thus, for HT oxidation:

$$\text{step (i): } \mathrm{HT} + \mathrm{S} \rightleftharpoons [\mathrm{HT}^{+}_{\mathrm{ads}} - \mathrm{S}] + e^{-} \qquad [2.8]$$

$$\text{step (ii): } [\mathrm{HT}^{+}_{\mathrm{ads}} - \mathrm{S}] \rightarrow \mathrm{HT}^{+} + \mathrm{S} \qquad [2.9]$$

$$\text{overall reaction: } \mathrm{HT} \rightleftharpoons \mathrm{HT}^{+} + e^{-} \qquad [2.10]$$

In Eqs. 2.8 and 2.9, 'S' refers to an adsorption site available on the electrode surface and HT^{+} refers to the oxidation product (oxoammonium cation), which can be in the adsorbed state 'ads' as in Eq. 2.8.

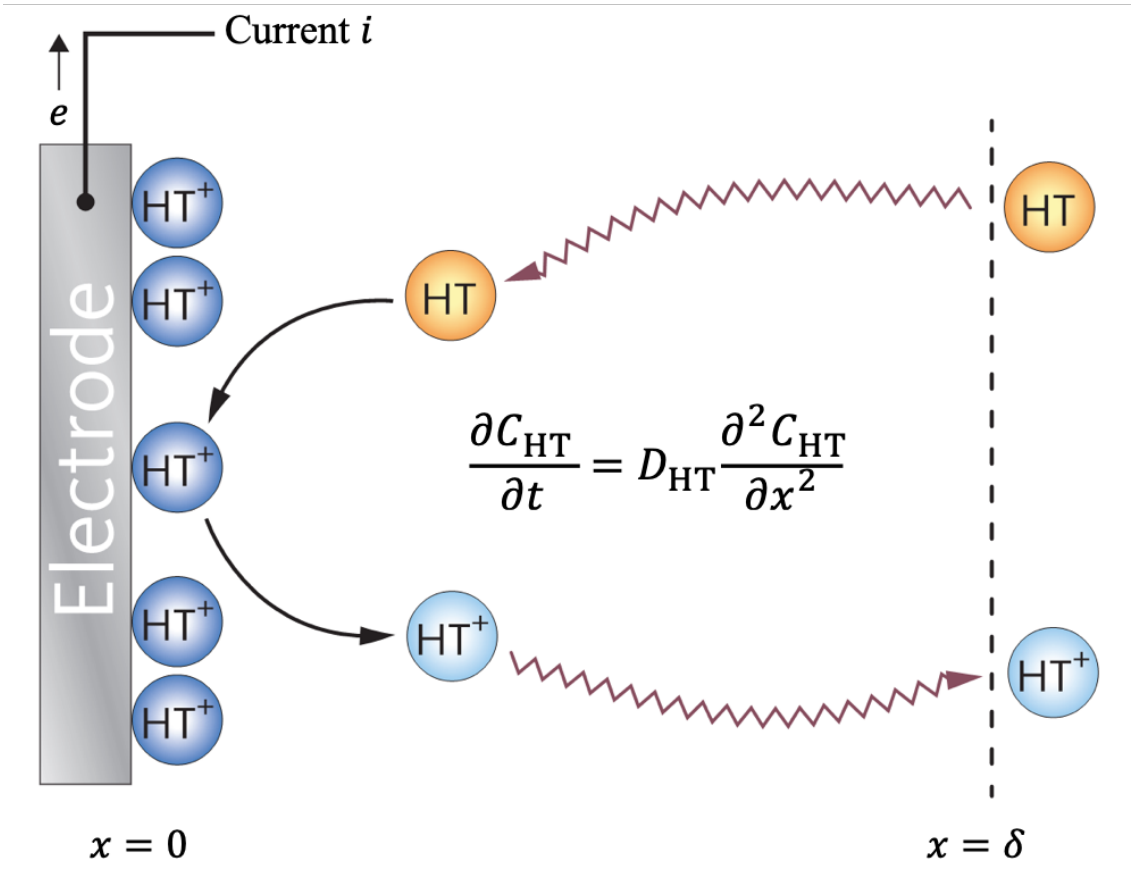

Figure 2.7. Schematic of the proposed adsorption–desorption model for HT oxidation involving (i) charge transfer and adsorption of product HT^+, followed by (ii) desorption of HT^+ which then diffuses away from the interface.

We now assume that the adsorption–charge–transfer step (i) (Eq. 2.8) is fast and thus near equilibrium, but the desorption step (ii) (Eq. 2.9) is slow and thus rate–determining. Equilibrium of step (i) can be represented by the well–known Frumkin adsorption isotherm,[54] which represents the dependence of the surface coverage (θ) of adsorbed HT^+, *i.e.*, fraction of the surface sites occupied by HT^+_{ads}, on the concentration of HT (C_{HT}) and the electrode potential (E):

$$\left(\frac{\theta}{1-\theta}\right)e^{g\theta} = \mathrm{K_{eq}}C_{\mathrm{HT}}e^{f(E-E_{\mathrm{eq}})} \qquad [2.11]$$

In Eq. 2.11, g is a constant representing lateral interactions between adsorbed species, $\mathrm{K_{eq}}$ is the equilibrium constant, E_{eq} is the equilibrium potential, and f $(= F/RT)$ is also a constant. For very low surface coverages, lateral interactions may be ignored and Eq. 2.11 takes the familiar form of the Langmuir adsorption isotherm:

$$\theta = \frac{\mathrm{K_{eq}}C_{\mathrm{HT}}e^{f(E-E_{\mathrm{eq}})}}{1+\mathrm{K_{eq}}C_{\mathrm{HT}}e^{f(E-E_{\mathrm{eq}})}} \qquad [2.12]$$

Also, at very low surface coverages, it is reasonable to assume: $\mathrm{K_{eq}}C_{\mathrm{HT}}e^{f(E-E_{\mathrm{eq}})} \ll 1$. Thus,

$$\theta \approx \mathrm{K_{eq}}C_{\mathrm{HT}}e^{f(E-E_{\mathrm{eq}})} \qquad [2.13]$$

Now, if step (ii), *i.e.*, desorption of $\mathrm{HT^{+}_{ads}}$, is the rate limiting step, then the overall reaction (Eq. 2.10) has the following rate expressed as current density (i_{k}):

$$\frac{i_{\mathrm{k}}}{nF} = k_{\mathrm{des}}\theta \qquad [2.14]$$

where n is the number of electrons transferred, k_{des} is the desorption rate constant. Combining Eq. 2.14 with Eq. 2.13, we get for $n = 1$:

$$i_{\mathrm{k}} \approx F k_{\mathrm{des}} \mathrm{K}_{\mathrm{eq}} C_{\mathrm{HT}} e^{f\left(E-E_{\mathrm{eq}}\right)} \qquad [2.15]$$

From Eq. 2.15, we obtain the apparent anodic transfer coefficient by applying its IUPAC definition:[46,55]

$$\alpha_{\mathrm{a}} = \left(\frac{RT}{nF}\right) \frac{d[\ln(i_{\mathrm{k}})]}{dE} \approx 1 \qquad [2.16]$$

Here, we refer to α_{a} as the "apparent" transfer coefficient because it does not completely resemble the transfer coefficient in a Butler–Volmer equation,[49] but simply represents an equivalent parameter for the newly derived rate expression in Eq. 2.15. The above discussion establishes that, for a one–electron transfer multi–step reaction pathway wherein desorption of the product is rate–limiting, apparent α_{a} approaches 1 at small coverages of the adsorbed intermediate. Thus, Eq. 2.8–10 (represented schematically in **Fig. 2.7**) can potentially explain the observed high values of α_{a} ($= 0.83-0.92$) in **Table 2.1**. This provides a clear hypothesis for the transient analysis presented below, *i.e.*, a multi–step reaction pathway involving a desorption–limited step (Eq. 2.9) is operational during the electrochemical oxidation of HT in ethaline and aqueous media.

2.4. Investigation of HT oxidation using fast–scan voltammetry

To obtain further evidence in support of reaction steps (i) and (ii) and the associated rate law, *i.e.*, Eqs. 2.11–16, we investigated the effects of adsorption–desorption during electrochemical oxidation of nitroxide radicals using fast–scan voltammetry (CV).

Following the guidelines provided by Shen et al.,[30] reproducible 'live' IR_Ω −compensated voltammograms were collected for the reaction: $\mathrm{HT} \rightleftharpoons \mathrm{HT}^+ + e^-$ in ethaline DES at various HT concentrations and scan rates. **Fig. 2.8** shows CVs acquired for 50 mM (**Fig. 2.8a–b**) and 200 mM (**Fig. 2.8c–d**) HT on a Pt RDE at 500 and 1500 RPM. From **Fig. 2.8a–b**, it is evident that at low bulk concentration (50 mM) of HT, the peak oxidation potential (E_p^a) is not a strong function of scan rate, suggesting the oxidation of HT is 'reversible'.[49] In contrast, at a bulk concentration of 200 mM, E_p^a shifts anodically by nearly 90 mV as the scan rate increases from 50 mV/s to 3 V/s. This suggests that, at high bulk concentrations, the oxidation of HT exhibits 'irreversible' behavior. For the present discussion, the definition that Nernstian processes are 'reversible' and those that deviate from Nernstian behavior are 'irreversible' is used.[49]

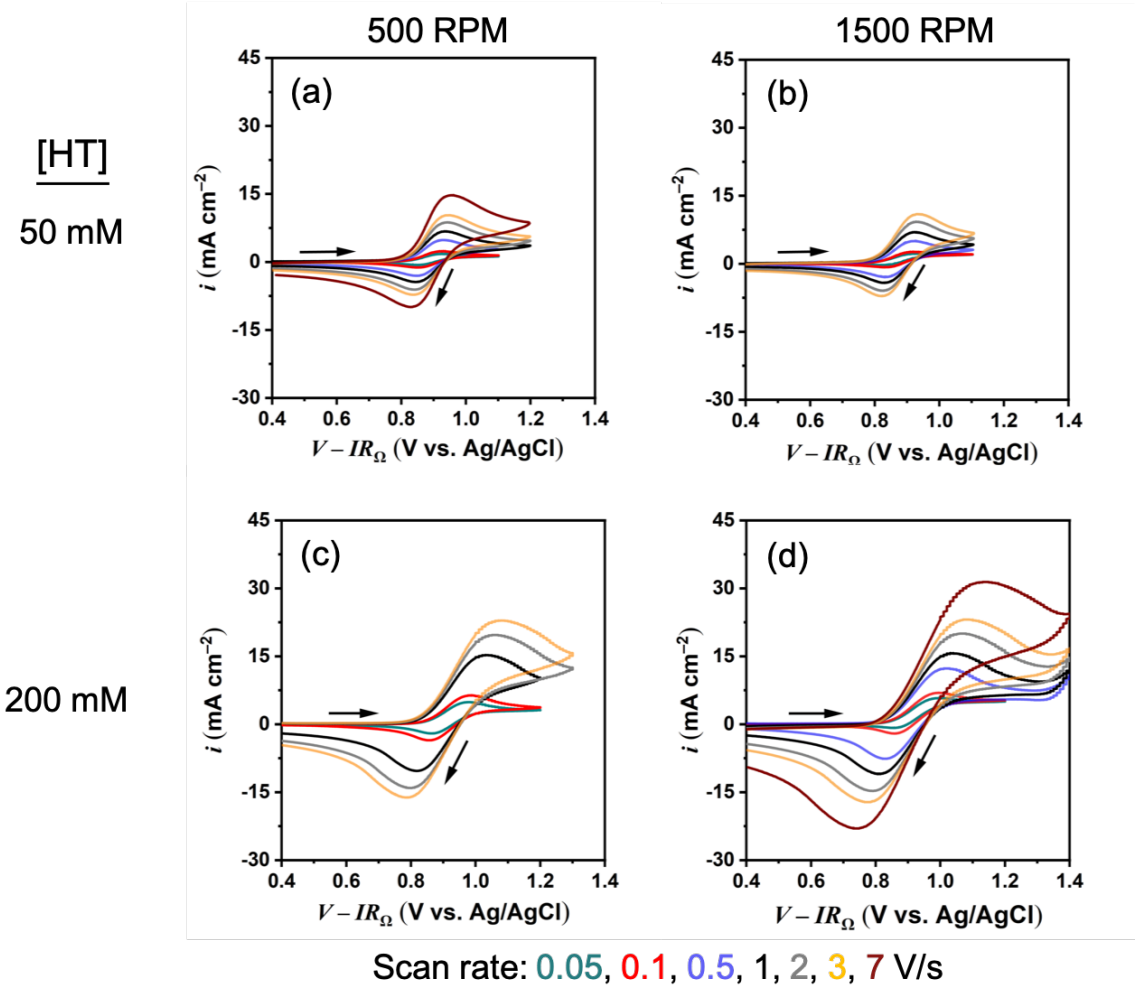

Figure 2.8. Cyclic voltammograms of (a, b) 50 mM HT and (c, d) 200 mM HT in ethaline, collected on a Pt RDE rotating at (a, c) 500 RPM and (b, d) 1500 RPM. The electrolyte was ethaline DES. The reference electrode was a passivated Ag wire calibrated against Ag/AgCl and the counter electrode was a graphite rod. The CV is reversible at low C_b and irreversible at high C_b.

The peak potentials E_p^a and peak current densities i_p^a measured from **Fig. 2.8** are plotted as a function of scan rate (ν or $\nu^{1/2}$) in **Fig. 2.9a** and **2.9b**, respectively. For 'reversible' processes, the anodic peak current density, i_p^a, in CV is given by the Randles–Sevcik equation:[56,57]

$$i_{\mathrm{p}}^{\mathrm{a}}\big|_{\mathrm{reversible}} = 0.4463\left(\frac{F^3}{RT}\right)^{1/2} n^{3/2}\, D_{\mathrm{HT}}^{1/2} C_{\mathrm{b}}\, \nu^{1/2} \qquad [2.17]$$

where n is the number of electrons transferred, D_{HT} is the HT diffusion coefficient ($= 1.6 \times 10^{-7}$ cm^2 s^{-1}, refer to **Fig. B.1**), C_{b} is the bulk concentration of HT, and ν is the scan rate. Solid lines in **Fig. 2.9b** show $i_{\mathrm{p}}^{\mathrm{a}}$ calculated using Eq. 2.17. At low HT concentration (50 mM), the Randles–Sevcik equation predicts $i_{\mathrm{p}}^{\mathrm{a}}$ values that are in good agreement with measurements reported in **Figs. 2.8a–b**. This is consistent with the ν–independent $E_{\mathrm{p}}^{\mathrm{a}}$ observed in **Fig. 2.9a**. However, when the HT concentration is high (200 mM), the value of $i_{\mathrm{p}}^{\mathrm{a}}$ measured experimentally is considerably lower than that calculated using Eq. 2.17. This observation, together with the observation of a stronger ν–dependence of $E_{\mathrm{p}}^{\mathrm{a}}$ observed in **Fig. 2.9a** for 200 mM HT, indicates deviation of system behavior from reversibility and the presence of irreversibility. For an 'irreversible' process, $i_{\mathrm{p}}^{\mathrm{a}}$ can be computed using the expression provided by Nicholson and Shain:[58]

$$i_{\mathrm{p}}^{\mathrm{a}}\big|_{\mathrm{irreversible}} = 0.4958\left(\frac{F^3}{RT}\right)^{1/2} \alpha_{\mathrm{a}}^{1/2}\, D_{\mathrm{HT}}^{1/2} C_{\mathrm{b}}\, \nu^{1/2} \qquad [2.18]$$

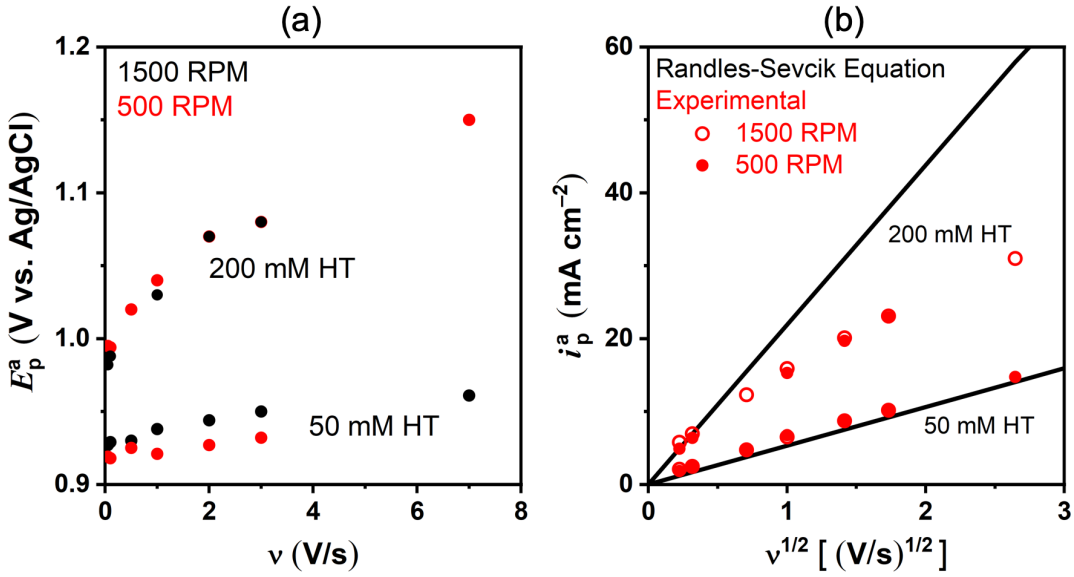

Figure 2.9. (a) Anodic peak potential E_p^a as a function of scan rate ν on a Pt RDE; (b) Experimentally measured i_p^a for 200 mM and 50 mM HT as a function of $\nu^{1/2}$. At higher C_b, experimental i_p^a data exhibits non–linearity and deviates substantially from predictions of Randles–Sevcik "reversible" theory.

Two observations can now be made to prove that the irreversible theory approach of Nicholson and Shain[58] (Eq. 2.18) is inadequate in describing data in **Fig. 2.9b** for high (200 mM) concentration of HT:

(i) Eq. 2.18 predicts a linear dependence of i_p^a on $\nu^{1/2}$; however, the non–linear behavior of the experimental data in **Fig. 2.9b** implies that the mechanism of irreversible HT oxidation is more complex than that described by simple Butler–Volmer or simplified Tafel kinetics; and

(ii) The ratio of anodic peak current density for an irreversible reaction (Eq. 2.18) to that for a one–electron transfer reversible reaction (Eq. 2.17) has a magnitude of roughly $1.1\alpha^{1/2}$. If α were 0.5 as for a simple symmetric charge transfer process, the peak current density ratio would be 0.79, *i.e.*, the observed i_p^a in **Fig. 2.9b** would be only

about 21% below the reversible theory solid line. However, in reality, the observed i_p^a is $>$ 35% lower in comparison to the reversible theory solid line, especially at high scan rates.

2.5. Comment on RDE rotation and cyclic voltammograms

Note, in **Figs. 2.8** and **2.9**, that the effect of the RDE rotation speed (in the range 500 – 1500 RPM) on E_p^a and i_p^a is rather small in fast–scan voltammetry. These results are expected when scan rates are sufficiently fast such that the concentration profile develops over a length scale much smaller than the steady–state diffusion boundary layer thickness. Under such conditions, the concentration gradient of a fast–scan CV collected on a rotating disk electrode resembles that of a stationary electrode.[59] This is represented schematically in **Fig. 2.10**.

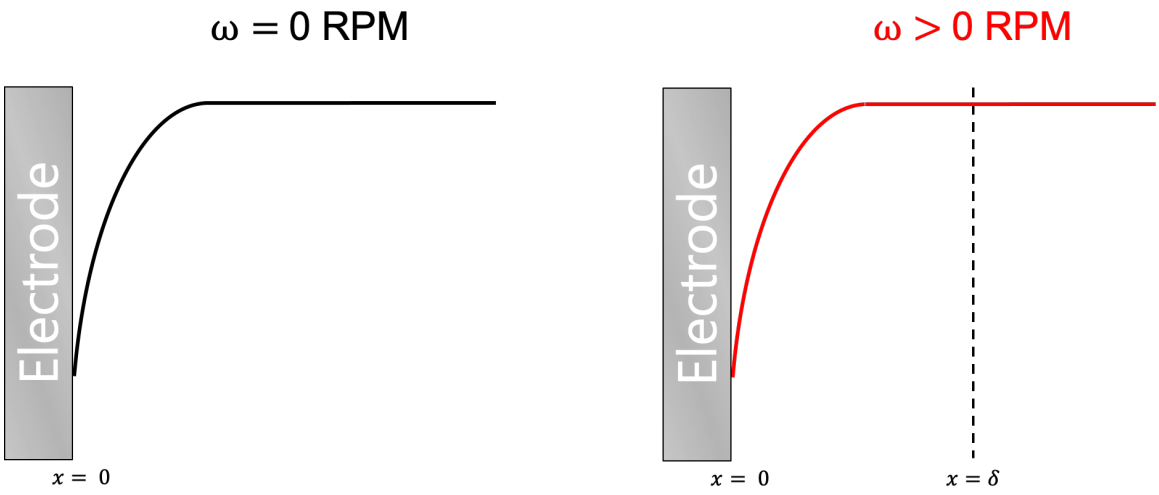

Figure 2.10. Schematic representation of the concentration profile during a fast–scan voltammogram collected on a stationary (ω = 0 RPM) and rotating (ω > 0 RPM) disk electrode. The concentration gradient develops very close to the electrode surface in both cases such that quiescent and semi–infinite diffusion assumptions remain valid.[59]

To further investigate the effect of rotation speed on voltammetry, fast–scan CVs were collected at a stationary (**Fig. 2.11a**) and rotating electrode (**Fig. 2.11b**) using the model reaction: $Fe(CN)_6^{4-} \rightleftharpoons Fe(CN)_6^{3-} + e^-$. The $Fe(CN)_6^{4-}/Fe(CN)_6^{3-}$ redox couple is well known to be an electrochemically reversible couple and is commonly used as a model couple for electroanalytical studies.[60,61] The anodic peak current density was then plotted as a function of $\nu^{1/2}$ in **Fig. 2.11c**. Note that when scan rates are sufficiently fast, the RDE rotation speed does not affect the measured peak current density.

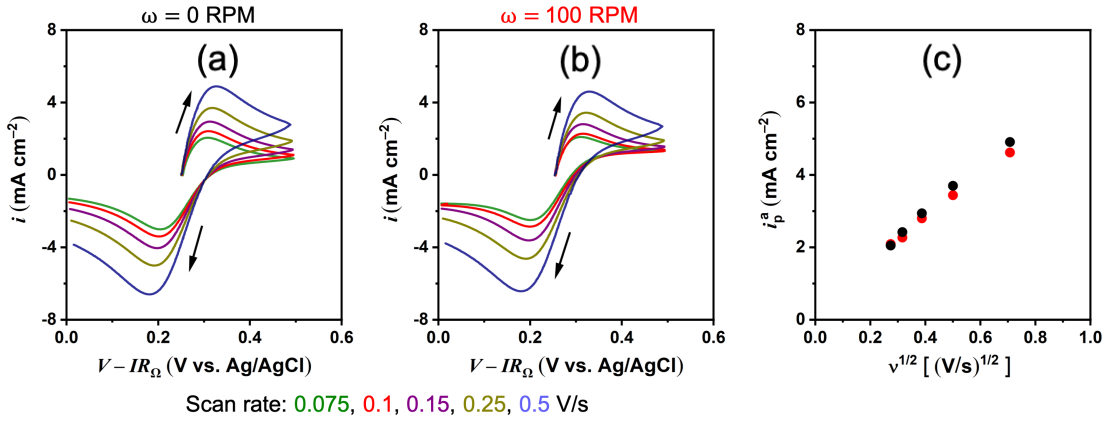

Figure 2.11. Cyclic voltammograms of a model system consisting of 10 mM $K_3Fe(CN)_6$ and $K_4Fe(CN)_6$ collected on a Pt RDE rotating at (a) 0 RPM and (b) 100 RPM at various scan rates. (c) Comparison between anodic peak current density i_p^a and square root of scan rate $\nu^{1/2}$ at different rotation speeds. When scan rates are sufficiently fast, the measured peak current density does not depend on rotation speed.

To ensure the effect of RDE rotation did not convolute transient measurements, CVs were collected for the $HT \rightleftharpoons HT^+ + e^-$ reaction at 0, 50, and 500 RPM (**Fig. 2.12a–c**). Again, here we note that RDE motion does not affect the measured peak current density at sufficiently fast scan rates (**Fig. 2.12d**).

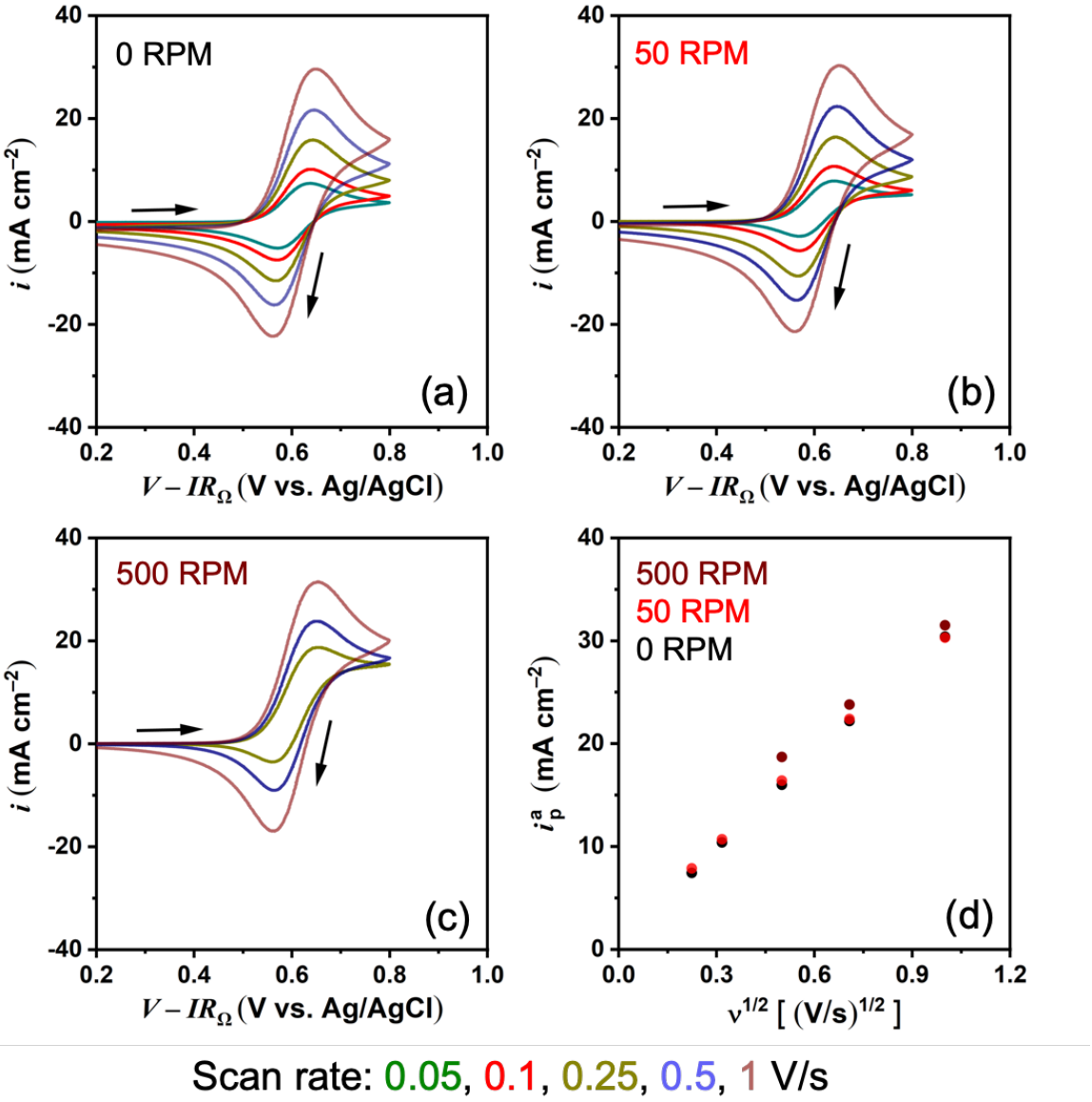

Figure 2.12. Cyclic voltammograms of 50 mM HT in 500 mM $NaCl_{aq}$ collected on a Pt RDE rotating at (a) 0 RPM, (b) 50 RPM, (c) 500 RPM and (d) comparison between anodic peak current density i_p^a and square root of scan rate $\nu^{1/2}$ at different rotation speeds. When scan rates are sufficiently fast, the measured peak current density does not depend on rotation speed.

2.6. Adsorption–desorption effects in fast–scan voltammetry – a numerical modeling study

To incorporate adsorption–desorption effects in fast–scan voltammetry, we resort here to numerical modeling of the transport and surface reaction during electrochemical oxidation of HT. Within close proximity of the electrode surface, *i.e.*, within the boundary layer (thickness δ), diffusion is the primary mode of species transport. Assuming one–dimensional diffusion, the concentration of HT (C_{HT}) within the boundary layer obeys Fick's second law (**Fig. 2.7**):

$$\frac{\partial C_{\mathrm{HT}}}{\partial t} = D_{\mathrm{HT}} \frac{\partial^2 C_{\mathrm{HT}}}{\partial x^2} \qquad [2.19]$$

where t is time and x is distance from the electrode surface. Initially, at $t = 0$, the concentration of HT is equal to the bulk concentration. Therefore:

$$t = 0: \quad 0 \leq x \leq \delta: \quad C_{\mathrm{HT}} = C_{\mathrm{b}} \qquad [2.20]$$

At the outer edge of the diffusion zone ($x = \delta$), the concentration of HT is fixed at its bulk value:

$$t > 0: \quad x = \delta: \quad C_{\mathrm{HT}} = C_{\mathrm{b}} \qquad [2.21]$$

At the electrode surface, the concentration of HT varies such that its rate of transport to the electrode surface always equates the electrochemical oxidation rate. Taking the latter oxidation rate from Eq. 2.14, we get:

$$t > 0: \quad x = 0: \quad D_{\mathrm{HT}} \frac{\partial C_{\mathrm{HT}}}{\partial x} = k_{\mathrm{des}} \theta \qquad [2.22]$$

where θ depends on electrode potential E per the Frumkin adsorption isotherm Eq. 2.11. Finally, in a potential scan experiment, E itself is time–dependent:

$$E = E_{\mathrm{i}} + \nu t \qquad [2.23]$$

where E_{i} is the initial potential. The diffusion–reaction problem outlined by Eqs. 2.11, 2.19–2.23 above was solved using the simulation software COMSOL®. Model parameters used for simulating the HT concentration profile are reported in **Table 2.2**. COMSOL® provided the concentration gradient for HT at the electrode surface ($x = 0$) from which the time–dependent current density (i) was determined:

$$i = F D_{\mathrm{HT}} \frac{\partial C_{\mathrm{HT}}}{\partial x} = F k_{\mathrm{des}} \theta \qquad [2.24]$$

Table 2.2. Model parameters used for simulating the adsorption–desorption mechanism for HT oxidation.

Parameter	Value(s)	Source
D_{HT}	1.6×10^{-7} cm^2 s^{-1}	**Fig. B.1**
δ	6 μm	Eq. B2
k_{des}	10^{-6} mol cm^{-2} s^{-1}	Selected to provide model agreement with experiments
K_{eq}	50 cm^3 mol^{-1}	
g	40	
ν	0.05 – 3 V/s	Chosen to match experimental conditions
C_{b}	200 mM	
E_{i}	0.4 V vs. Ag/AgCl	
E_{eq}	0.88 V vs. Ag/AgCl	

Fig. 2.13a shows the simulated i vs. E response for the oxidation of 200 mM HT at several scan rates. Similar to experimental CV response (**Figs. 2.8a–d**), the $E_{\mathrm{p}}^{\mathrm{a}}$ values shift anodically in the simulated voltammograms as the scan rate is increased. Simulated $i_{\mathrm{p}}^{\mathrm{a}}$ (solid *blue* line) values are plotted in **Fig. 2.13b**. As noted, significantly improved agreement with experimental data (*red* points) is observed compared to the reversible theory (solid *black* line). This agreement is partly expected because the model has several adjustable parameters (k_{des}, K_{eq}, and g in **Table 2.2**). Model agreement with experimental data was observed for parameters listed in **Table 2.2**; however, the range of acceptable values of k_{des}, K_{eq}, and g is rather large. Thus, values reported in **Table 2.2** should not be viewed as parameter sets uniquely representative of the HT oxidation process. Nonetheless, the key takeaway message here is that the proposed diffusion–reaction model incorporating adsorption–desorption effects during HT oxidation does capture the non–linearity of the $i_{\mathrm{p}}^{\mathrm{a}}$

on $\nu^{1/2}$ dependence and thus presents an advancement over the simplistic Nicholson–Shain model of irreversibility (Eq. 2.18).

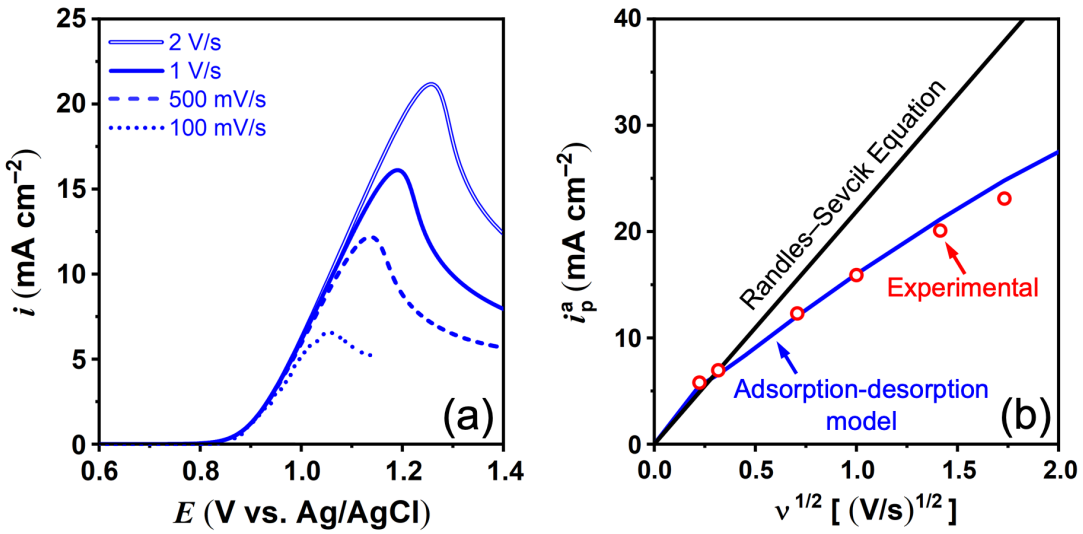

Figure 2.13. (a) Simulated fast–scan voltammograms of the oxidation of 200 mM HT at various scan rates. (b) Comparison between peak current density i_p^a from experiments, theory assuming "reversible" behavior, and numerical simulations incorporating proposed adsorption–desorption effects. Note that the proposed model agrees reasonably well with experimental data and predicts deviations of experimentally measured peak currents from those predicted using "reversible" theory.

2.7. Current distribution effects during fast–scan voltammetry

It was discussed above that, during slow–scan polarization measurements on Pt RDE, the current distribution as assessed by the Wagner number (Wa) at average current densities in the ≈ 1 mA cm^{-2} range is relatively uniform. However, during fast–scan polarization measurements, the Pt RDE experiences much higher average current densities of > 20 mA cm^{-2} at $\nu > 2$ V/s (**Fig. 2.8**). This raises the question of whether secondary current distribution non–uniformity may convolute the interpretation of the fast–scan

voltammetry results. So, we calculated the Wagner number at higher current densities using its standard definition for RDE geometry:[62]

$$\mathrm{Wa} = \frac{RT}{\alpha F i}\left(\frac{4\kappa}{\pi r}\right) \qquad [2.25]$$

where κ is the electrolyte conductivity ($\approx$ 8 mS cm^{-1}) and r is the disk radius (0.25 cm). To estimate α at high current densities, we revisit the adsorption–desorption model wherein:

$$i_{\mathrm{k}} = F k_{\mathrm{des}} \theta \qquad [2.26]$$

where θ obeys:

$$\left(\frac{\theta}{1-\theta}\right) e^{g\theta} = \mathrm{K}_{\mathrm{eq}} C_{\mathrm{HT}} e^{f\left(E - E_{\mathrm{eq}}\right)} \qquad [2.27]$$

Taking optimal parameter values in **Table 2.2**, we calculated the $i-E$ relationship from Eqs. 2.26 and 2.27. Note that, unlike conventional Tafel kinetics, the present adsorption–desorption approach leads to a potential– or current–dependent apparent α_{a}, which was computed as:

$$\alpha_{\mathrm{a}} = \left(\frac{RT}{F}\right)\frac{d[\ln(i_{\mathrm{k}})]}{dE} \qquad [2.28]$$

i_k and θ were calculated as a function of E from Eqs. 2.26 and 2.27, respectively, and are shown in **Fig. 2.14**. **Fig. 2.14** highlights the point mentioned above, *i.e.*, the apparent Tafel slope (and thus α) is not a fixed value and varies with the current or potential. For i_k in the vicinity of ~ 20 mA cm^{-2}, α_a is close to 0.1 (not to be confused with $\alpha_a \approx 0.9$ for the low current density regime), which provides Wa $\approx$ 0.5 from Eq. 2.25. As shown by Newman[62] and West,[63] this value of Wagner number although not representative of highly uniform current distribution, is acceptable for analysis of kinetics effects.

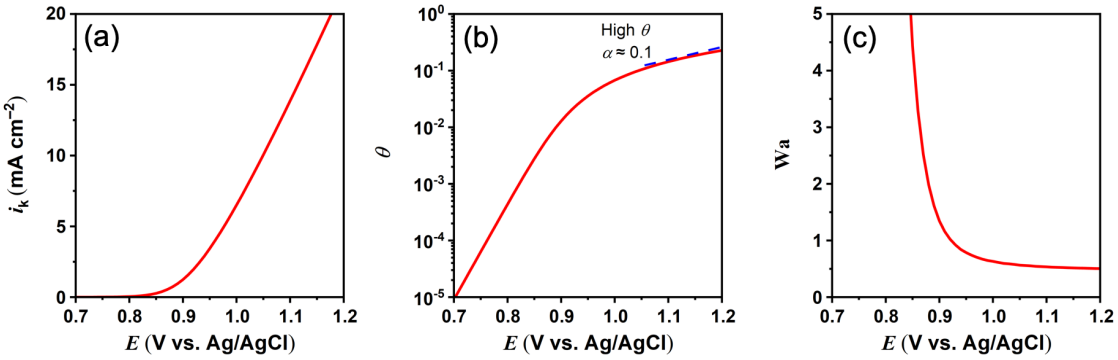

Figure 2.14. (a) Current density i, (b) adsorbed HT^+ coverage θ, and (c) Wa number as a function of the electrode potential E. The charge transfer coefficient α is high (~1) when i and θ are low, but it decreases as i and θ increase. The Wa number decreases as i increases, but is maintained at acceptably high values (> 0.5) due to a gradually decreasing α.

2.8. Conclusions

Oxidation of 4–hydroxy–TEMPO in ethaline DES and aqueous media was investigated using steady–state and transient voltammetry, and diffusion–reaction modeling. The following key conclusions can be drawn from the present work:

(i) The anodic charge transfer coefficient α for 4–hydroxy–TEMPO reaction (Eq. 2.1) approaches $\alpha_a \approx 0.9$ and is significantly higher than that expected for symmetric

one–electron transfer reactions. This observation is true for reactions in DES and in aqueous media.

(ii) A two–step mechanism (Eqs. 2.8, 2.9) is proposed for oxidation of 4–hydroxy–TEMPO. Per this mechanism, rate of oxidation is limited by the desorption of adsorbed oxidized product species (oxoammonium cations). It is shown that, at low surface coverages of the adsorbed species, *i.e.*, slow rates or currents, the proposed model predicts $\alpha \approx 1$ consistent with experiments.

(iii) Validity of the model was tested by incorporating adsorption–desorption effects into numerical simulations of transient effects during fast–scan cyclic voltammetry. Particularly at high concentration (200 mM) of 4–hydroxy–TEMPO, the simulations uniquely and quantitatively captured the extent of suppression of the peak current during cyclic voltammetry compared to the case of completely reversible reactions. This gives confidence that the proposed adsorption–desorption framework represents adequately the nature of irreversibility prevalent during oxidation of 4–hydroxy–TEMPO.

Chapter 3. Electro–oxidation of nitroxide radicals: Adsorption–mediated charge transfer probed using potentiometry and spectroscopy

---

In Chapter 2, the anodic charge transfer coefficient (α_a) corresponding to the electro–oxidation of HT in an aqueous medium is ~ 0.9, i.e., α_a deviates considerably from the expected value (0.5) for a symmetric single–step one–electron transfer redox reaction. To explain this unusual value of α_a, an adsorption–desorption mechanism was proposed wherein oxidation of HT leads to the adsorption of the oxidation product, which then undergoes slow rate–limiting desorption from the electrode surface.

In this chapter, electrochemical, spectroscopic, and gravimetric evidence is presented in support of the adsorption–desorption mechanism. Potentiometry is employed to track the gradual re–equilibration of the electrode–electrolyte interface following the electro–oxidation of HT. Analysis of the chronopotentiometry data further suggests the presence of adsorbed species. *In situ* measurements using surface enhanced Raman spectroscopy (SERS) is discussed.

3.1. Experimental procedure

3.1.1. Materials

Sodium chloride (NaCl, $\geq 99\%$ purity, Sigma–Aldrich), ferrous chloride ($FeCl_2$, 99.5% purity, Alfa Aesar), cuprous chloride (CuCl, anhydrous, 99% purity, Acros Organics), cupric chloride dihydrate ($CuCl_2 \cdot 2H_2O$, 99% purity, Acros Organics) and 4–hydroxy–TEMPO (HT, $C_9H_{18}NO_2$, $> 98\%$ purity, Alfa Aesar) were used as received.

3.1.2. Methods

Electrolyte preparation: Aqueous electrolytes containing 500 mM NaCl were prepared using Millipore ultrapure (18.2 MΩ · cm) deionized water and de–aerated by purging Ar gas. Appropriate amounts of the electroactive materials ($FeCl_2$ or HT, 200 mM) were added to the aqueous 500 mM NaCl electrolyte. To define a stable and reproducible equilibrium state of the electrode surface, a redox couple (1 mM each of CuCl and $CuCl_2$) was also present in the electrolyte during the chronopotentiometry experiments. The high concentration of chloride in the electrolyte stabilizes Cu^{1+} and prevents spontaneous disproportionation.[64,65]

Electrochemical measurements: Steady–state polarization and chronopotentiometry experiments were performed in a standard three–electrode configuration. The working electrodes were 5 mm diameter polycrystalline Au, Pt, and glassy carbon (GC) rotating disk electrodes (RDE, Pine Research Instrumentation). Prior to each electrochemical experiment, the exposed electrode surface was mechanically polished first using 0.3 μm followed by 0.05 μm alumina slurry, then sonicated in deionized water. The counter electrode was a graphite rod, and the reference electrode was saturated Ag/AgCl (Fisher Scientific). A Princeton Applied Research PARSTAT 4 was used for all electrochemical experiments. On the RDE, the ohmic resistance was measured using electrochemical impedance spectroscopy prior to each experiment and confirmed to be $R_\Omega = 20\ \Omega$. IR_Ω–correction was applied to steady–state polarization data during post–processing. For potentiometry experiments on the RDE, rotation was set to a low value (50 RPM) to minimize potential shearing of adsorbed species by fluid flow.

Electrochemical surface enhanced Raman spectroscopy (eSERS): A Renishaw® inVia Raman Microscope RE04 and AutoLab PGSTAT302N potentiostat were used to collect *in situ* Raman spectra. All Raman spectra reported in this chapter were collected at 532 nm excitation, 50% laser power ($\sim$1.35 MW cm^{-2}), 20 × magnification, 4 s exposure time, and 1800 nm grating. The reference electrode was a passivated Ag wire,[37] and the counter electrode was a coiled Au wire. To enhance the signature of species adsorbed to the electrode surface, a Au disk (6 mm diameter) was electrochemically roughened by cycling the electrode from 0 V to 1.2 V vs. Ag/AgCl at 1 V/s. This cycle was repeated 20 times. The roughening electrolyte contained 500 mM $NaCl_{aq}$. During the roughening procedure, the reference electrode was a saturated Ag/AgCl and the counter electrode was a graphite rod.

3.2. Determining the transfer coefficient on Au

Polarization of HT has been reported in literature, where slow–scan voltammetry showed a HT oxidation equilibrium potential of approximately 0.75 V vs. NHE,[9] or 0.53 V vs. Ag/AgCl for $C_b = 1$ mM. Using the Nernst equation to adjust for the concentration (200 mM) used in this work, we arrive at 0.39 V vs. Ag/AgCl and thus very close to the value ($\sim$0.33 V) observed in **Fig. 3.1**. To avoid Au dissolution in the chloride medium at anodic potentials, voltammetry on Au (*blue*) was limited to potentials only up to 0.6 V vs. Ag/AgCl. This ensured the potentials did not trigger Au dissolution, which occurs at potentials anodic to 0.7 V vs. Ag/AgCl.[66] The scan was also repeated on a Pt RDE (*black*).

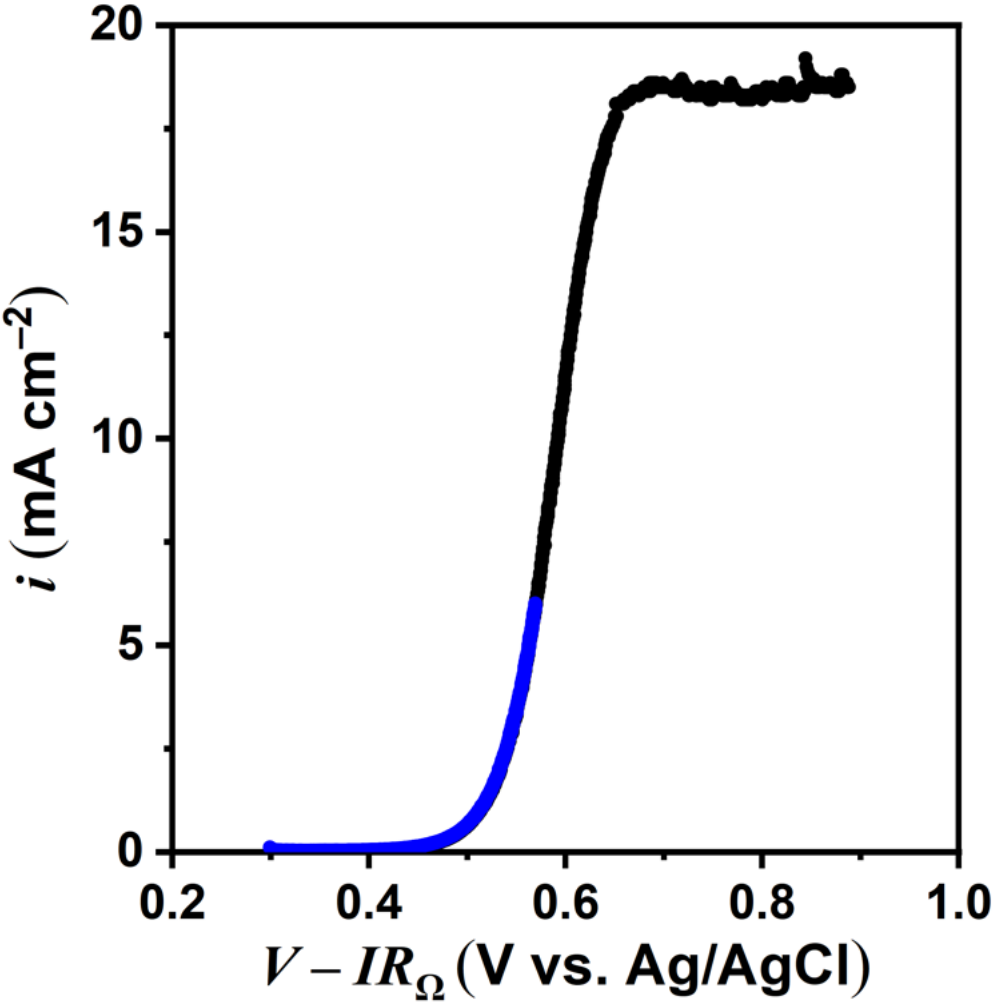

Figure 3.1. Slow–scan (10 mV/s) linear sweep voltammogram for 200 mM HT in 500 mM $NaCl_{aq}$ collected on a Pt (*black*) and Au (*blue*) RDE at ω = 50 RPM.

Assuming Tafel kinetics, the current–overpotential relationship can be expressed as:

$$i = i_0 \left(1 - \frac{i}{i_L}\right) \exp(\alpha_a f \eta_s) \qquad \text{[2.2] (revisited)}$$

where i, i_0 and i_L are the measured, exchange and limiting current densities, respectively, $f\,(=F/RT)$ is a constant, and η_s is the surface overpotential $(=V-IR_\Omega-E_{eq})$. Additionally, F is Faraday's constant, R is the universal gas constant, and T is the solution temperature. The current densities were calculated based on the geometric surface area of the electrode, and i_L was taken as the current density at the limiting plateau seen in **Fig. 3.1**. We assumed here that i_L is independent of the nature of the substrate and that its value on Au and Pt is similar because of the similar mass–transport conditions used. Because LSV was performed at slow scan rates such that diffusional relaxation is fast ($4\delta^2/\pi^2 D \sim 3$ s) compared to the duration of the LSV experiment (60 s), pseudo steady–state may be assumed. Here, δ and D are the boundary layer thickness and diffusion coefficient, respectively. Rearranging Eq. 2.2, a semi–log plot of the kinetic current density $i_k = i \cdot i_L/(i_L - i)$ versus $V - IR_\Omega$ was generated (**Fig. 3.2**). On such a semi–log plot, Tafel kinetics provide linearity as expressed in Eq. 2.3:

$$\log_{10}(i_k) = \left[\log_{10} i_0 - \left(\frac{\alpha_a f}{2.303}\right) E_{eq}\right] + \left(\frac{\alpha_a f}{2.303}\right)(V - IR_\Omega) \qquad \begin{matrix}[2.3]\\(\text{revisited})\end{matrix}$$

The slope $\alpha_a\, f/2.303$ was measured from the Tafel curve in **Fig. 3.2**, and the value of the charge transfer coefficient of HT oxidation was calculated on Au to be: $\alpha_a^{HT} = 0.88$. This is in good agreement with reported[20] $(= 0.89)$ and estimated[9] $(= 0.91)$ values of α_a^{HT} on Pt. This value of α_a^{HT} approaching unity can be explained using the 'adsorption–desorption' mechanism depicted in **Fig. 2.7** which comprises of: (step *i*) electron transfer followed by adsorption of the oxidation product (oxoammonium cation); and (step *ii*) desorption of the adsorbed oxoammonium cation back into the electrolyte. Now we assume

that the adsorption and charge–transfer step (i) is fast and thus near equilibrium, but the desorption step (ii) is slow and thus rate–determining.

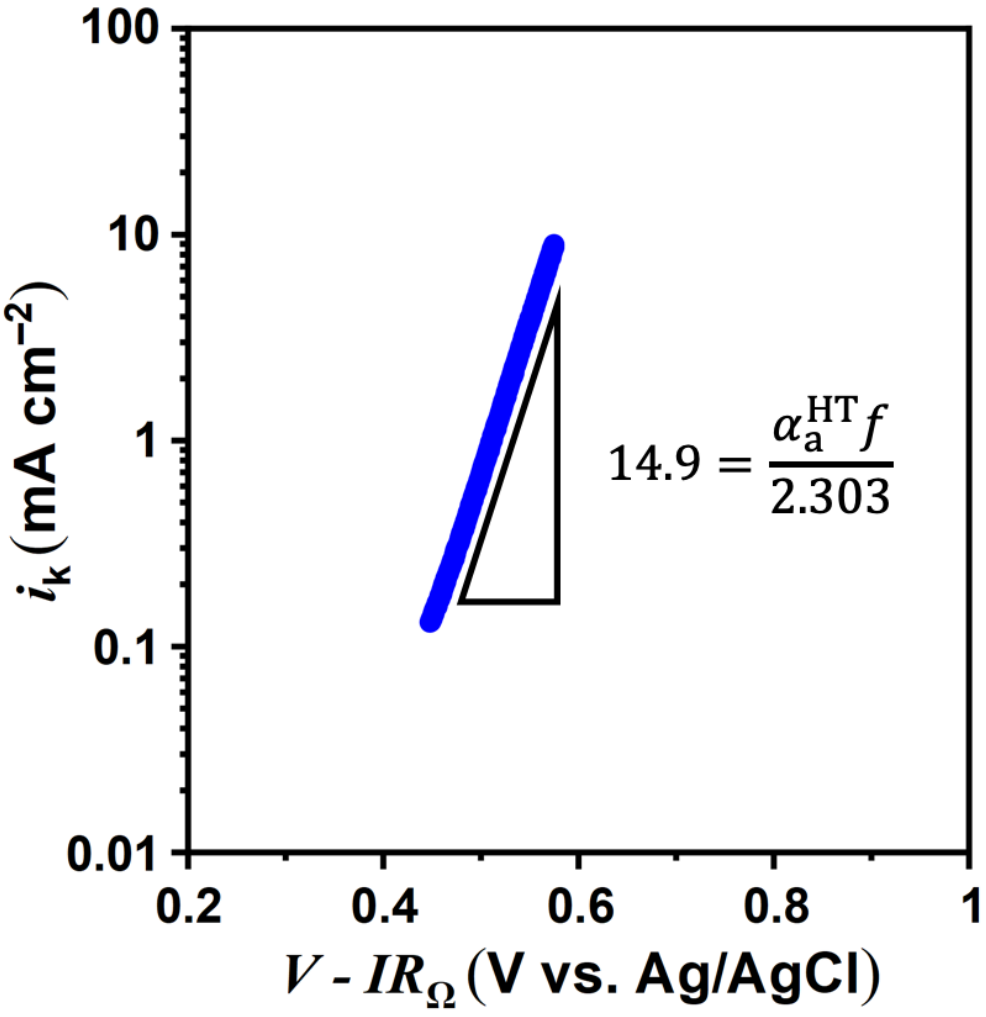

Figure 3.2. Tafel plot for the oxidation of 200 mM HT in 500 mM $NaCl_{aq}$ on a Au RDE at 50 RPM. Tafel slope provides α_a^{HT} = 0.88, which is in close agreement with the value of α_a^{HT} previously reported.[20]

3.3. Electrochemical surface–enhanced Raman spectroscopy

Fig. 3.3 shows the Raman spectra (*left*) collected of HT during the initial open circuit condition, $83\ \text{min}$ under an oxidative potential ($0.8\ \text{V vs. Ag/AgCl}$), and $23\ \text{min}$ after the electrode was released to open circuit conditions. When an oxidative potential was applied, a sharp Raman peak appeared at $1624\ \text{cm}^{-1}$ associated with the $\text{N}^{+}=\text{O}$ moiety present in the oxoammonium ion.[66,67] In a similar study, Shaheen et al.[66] studied the adsorption of HT^{+} on a roughened Au electrode using eSERS. Using a combination of experiments and density functional theory, they identified a peak at $1608\ \text{cm}^{-1}$ as that of the $\text{N}^{+}=\text{O}$ moiety. This is consistent with the peak observed at $1624\ \text{cm}^{-1}$ in **Fig. 3.3**. Also shown in **Fig. 3.3** are optical images (*right*) collected to show the time–evolution of the HT^{+} film (*black*) forming on the electrode (*yellow*) surface. It is noteworthy that the film is present even after releasing the electrode to open circuit conditions for $25\ \text{min}$.

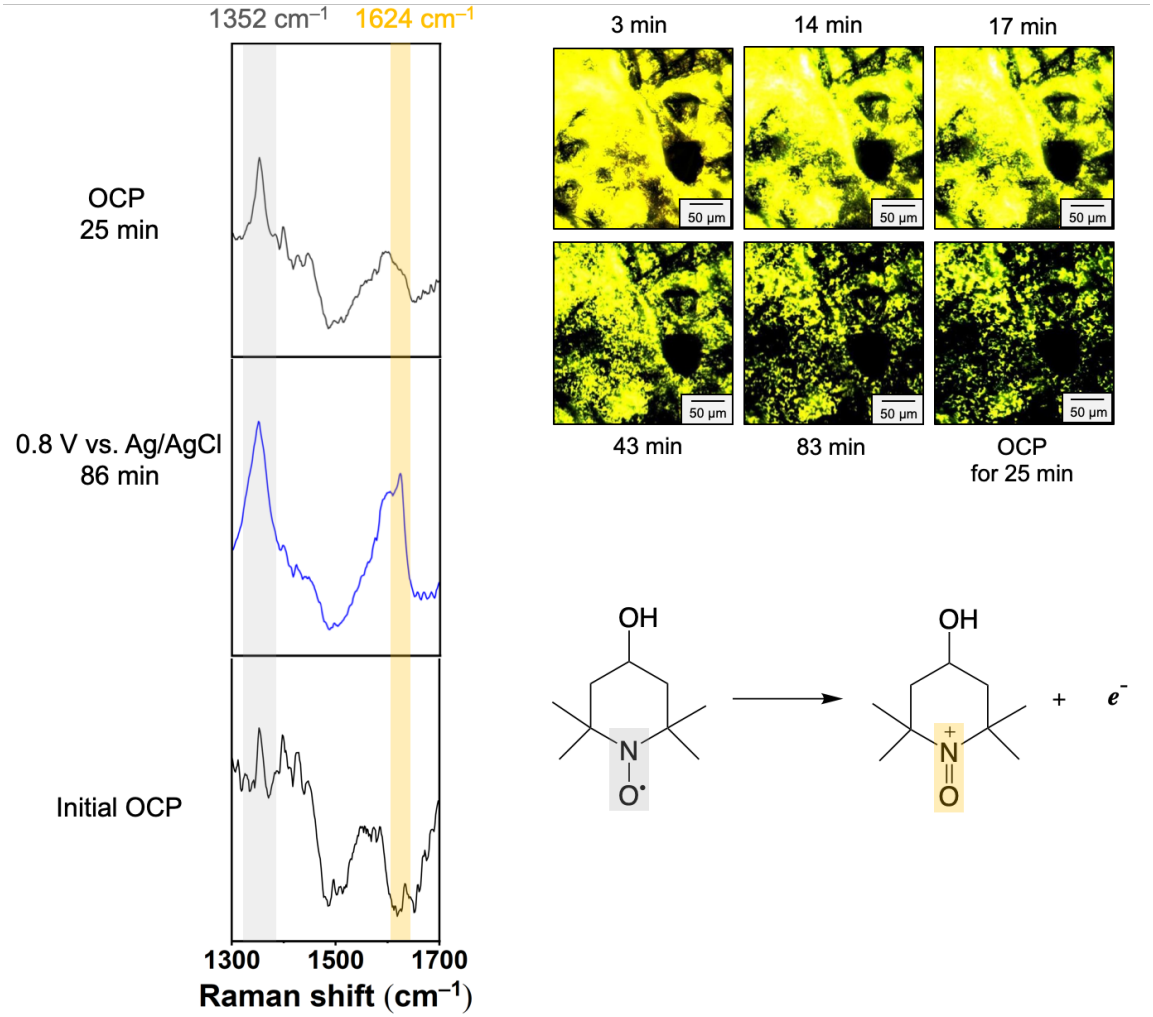

Figure 3.3. (*left*) *In situ* surface–enhanced Raman spectra collected in a solution of 200 mM HT in 500 mM $NaCl_{aq}$ and on an electrochemically roughened Au working electrode. The reference electrode was a passivated Ag wire, and the counter electrode was a Au wire. (*right*) Real–time optical images of the Au electrode during HT oxidation that show the time–evolution of HT^+ accumulation on the electrode surface. Spectra and optical images indicate the presence of adsorbed HT^+ 25 min after the electrode was released to open circuit conditions, suggesting slow desorption of HT^+ from the electrode.

3.4. Electrochemically probing surface–adsorbed species in HT electro–oxidation

3.4.1. Short time scales: slope of the potential transient

The above eSERS study confirmed the presence of surface–adsorbed species during HT electro–oxidation. To further investigate their effects, chronopotentiometry was used

to probe for signatures of surface adsorption in the time–dependent response of the open circuit potential immediately following potentiostatic HT electro–oxidation. Quantifying the potential–relaxation after HT electro–oxidation is terminated benefits from the use of a tracer redox couple in the electrolyte, as shown in the analysis below. For potentiometry experiments, we chose $1\ \mathrm{mM}$ of CuCl (Cu^{1+}) and $1\ \mathrm{mM}$ of $\mathrm{CuCl_2}$ (Cu^{2+}) as the couple present in the electrolyte alongside HT. At a Au electrode, this couple establishes the following equilibrium state: $\mathrm{Cu}^{1+} \rightleftharpoons \mathrm{Cu}^{2+} + e^{-}$, with an equilibrium potential of $0.25\ \mathrm{V\ vs.\ Ag/AgCl}$. Two cases are considered: (i) Chronopotentiometry following the electro–oxidation of Fe^{2+} in which surface–adsorption is absent and $\alpha_{\mathrm{a}}^{\mathrm{Fe}} \sim 0.5$,[61,68] and (ii) Chronopotentiometry following the electro–oxidation of HT in which surface–adsorbed HT^{+} is formed and $\alpha_{\mathrm{a}}^{\mathrm{HT}} \sim 1$.[20]

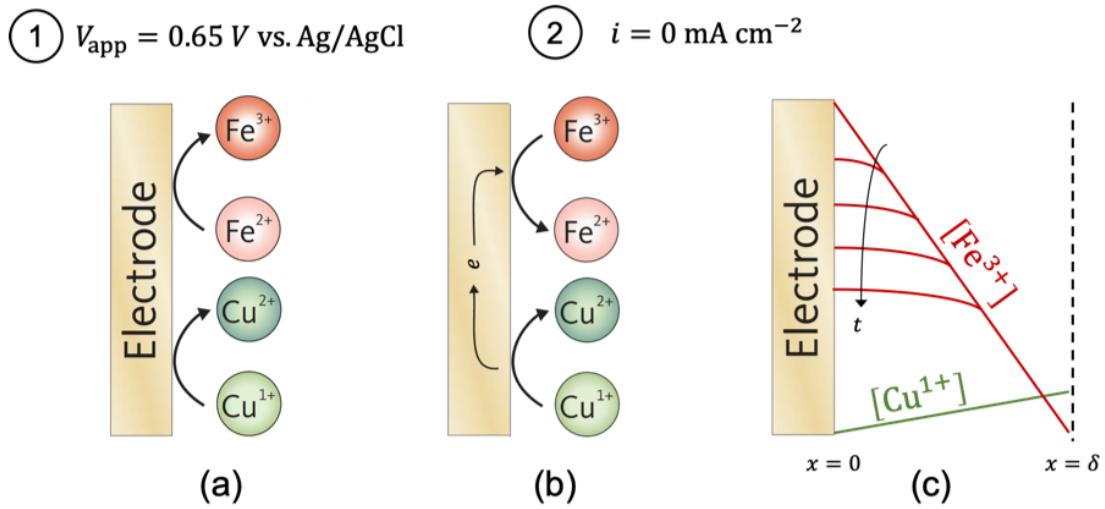

Figure 3.4. (a) In step 1, an oxidative potential (0.65 V vs. Ag/AgCl) is applied to the working electrode such that Cu^{1+} and Fe^{2+} are oxidized to Cu^{2+} and Fe^{3+}, respectively, (b) In step 2, under open circuit conditions, Cu^{1+} is spontaneously oxidized to Cu^{2+} causing reduction of the Fe^{3+} generated in step 1, (c) The time–dependent concentration profile evolution of Fe^{3+} in step 2 (*red*) causes the surface mixed potential to gradually change until the surface equilibrium ($Cu^{1+} \rightleftharpoons Cu^{2+} + e^{-}$) is eventually re–established. During the early stages of this re–equilibration, the concentration profile of Cu^{1+} (*green*) remains relatively unaltered because Cu^{1+} oxidation is transport–limited and near steady–state.

Case (i): Fig. 3.4 describes the two–step experiment in which an oxidative potential (step 1, 0.65 V vs. Ag/AgCl) is first applied to the Au working electrode for 120 s such that electro–oxidation of Fe^{2+} is facilitated. In the presence of Cu^{1+} in the electrolyte, two reactions proceed at this applied potential (**Fig. 3.4a**):

$$Fe^{2+} \rightarrow Fe^{3+} + e^{-} \qquad [3.1]$$

$$Cu^{1+} \rightarrow Cu^{2+} + e^{-} \qquad [3.2]$$

Because Cu^{1+} is present at a very low concentration (1 mM), diffusion–limitations imply that its concentration near the electrode surface at the end of step 1 approaches zero:

$[Cu^{1+}]_{x=0} = 0$ mM. Following Fe^{2+} electro–oxidation, the Au electrode was released to open circuit conditions (step 2 in **Fig. 3.4b**) and the time–evolution of the surface mixed potential was recorded. Under open circuit conditions, the surface potential depends on the rates of the following oxidation–reduction reactions which occur spontaneously:

$$\text{Oxidation: } Cu^{1+} \rightarrow Cu^{2+} + e^{-} \quad [3.3]$$

$$\text{Reduction: } Fe^{3+} + e^{-} \rightarrow Fe^{2+} \quad [3.4]$$

$$\text{Overall reaction: } Fe^{3+} + Cu^{1+} \rightarrow Fe^{2+} + Cu^{2+} \quad [3.5]$$

Reaction 3.5 leads to consumption of the Fe^{3+} generated in reaction 3.1. The gradual decrease of Fe^{3+} near the electrode surface in step 2 is depicted schematically in **Fig. 3.4c**. The change in surface concentration causes the gradual shift in the mixed potential towards the eventual equilibrium state fixed by the redox couple $Cu^{1+} \rightleftharpoons Cu^{2+} + e^{-}$ (0.25 V vs. Ag/AgCl). This measured mixed potential transient is shown in **Fig. 3.5**. At the start of step 2, an instant shift of ~0.16 V is noted which is attributed to activation (charge transfer) processes which have a very fast response time. Then, a slow change in the mixed potential is recorded over a time–scale of ~10 s. This surface mixed potential is determined by charge balance during oxidation–reduction such that the rate of Cu^{1+} oxidation (Eq. 3.3) matches that of Fe^{3+} reduction (Eq. 3.4):

$$r_{ox} = r_{red} \quad [3.6]$$

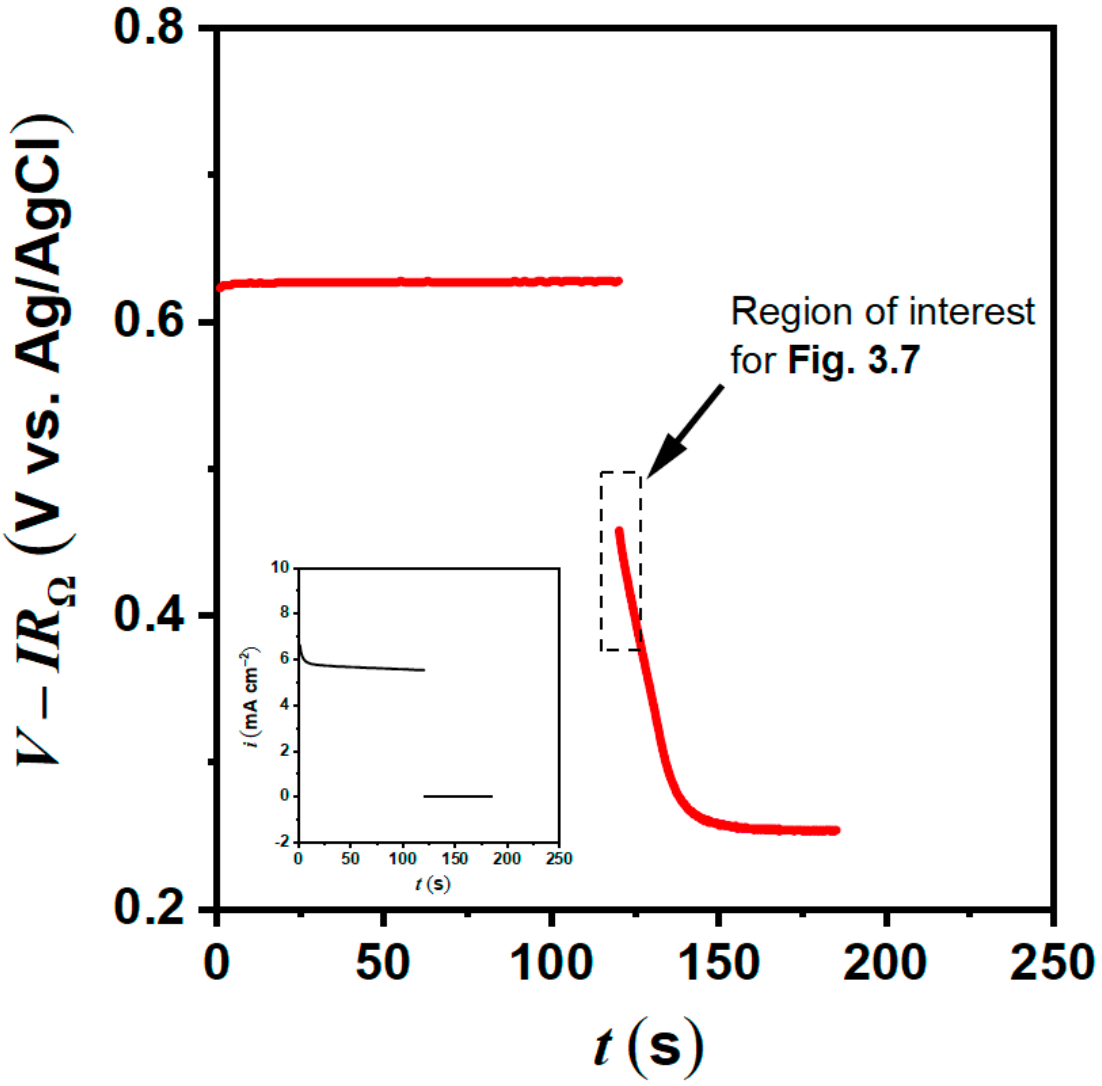

Figure 3.5. The potential transient for 200 mM $FeCl_2$ in 500 mM $NaCl_{aq}$ collected on a Au RDE rotating at 50 RPM. The electrode was held at 0.65 V vs. Ag/AgCl for 120 s in step 1, and released to open circuit conditions in step 2. The region of interest for **Fig. 3.7** is highlighted. Inset shows the current–time response.

Since Cu^{1+} is present at very low concentrations, its oxidation rate can be assumed to be equal to its diffusion–limited oxidation current density. For kinetically–limited Fe^{3+} reduction, Tafel kinetics can be assumed. Thus, Eq. 3.6 takes the form:

$$i_{\mathrm{L}}^{\mathrm{Cu}} = \beta[\mathrm{Fe}^{3+}]_{\mathrm{x=0}} \exp\left(-\alpha_{\mathrm{c}}^{\mathrm{Fe}} f\left(E - E_{\mathrm{eq}}^{\mathrm{Fe}}\right)\right) \quad [3.7]$$

where $i_{\mathrm{L}}^{\mathrm{Cu}}$ is the limiting current density of reaction 3.3, $\beta = i_0^{\mathrm{Fe}}/[\mathrm{Fe}^{3+}]_{\mathrm{ref}}$, $[\mathrm{Fe}^{3+}]_{\mathrm{x=0}}$ is the concentration of Fe^{3+} at the electrode surface, and i_0^{Fe}, $\alpha_{\mathrm{c}}^{\mathrm{Fe}}$, and $E_{\mathrm{eq}}^{\mathrm{Fe}}$ are the exchange current density, cathodic charge transfer coefficient, and equilibrium potential corresponding to the reduction reaction (Eq. 3.4). Here, β is a parameter reflecting the ratio between typical[68] values of the exchange current density of reaction 3.4 and the reference concentration of Fe^{3+} ($\sim$200 mM).

In addition to Fe^{3+} consumption at the electrode surface via reaction 3.5, it also undergoes transient diffusion away from the electrode. Here, consumption of Fe^{3+} via the homogeneous reaction with Cu^{1+} is assumed to be negligible. A rationale for this assumption is provided in section 3.4.3. Briefly, we consider diffusional transport only so as to calculate the slowest rate of change of potential, and show that this predicted rate agrees with the experimentally observed rate. Concentration profile of Fe^{3+} thus obeys Fick's second law:

$$\frac{\partial C_{3+}}{\partial t} = D_{3+} \frac{\partial^2 C_{3+}}{\partial x^2} \quad [3.8]$$

where t is time (initiated at the start of step 2), x is distance from the electrode surface, and D_{3+} is the diffusion coefficient of Fe^{3+} (refer to **Fig. B.2**). At the end of step 1, the Cu^{1+} and Fe^{3+} concentration profiles are linear (because steady–state is reached) as shown

schematically in **Fig. 3.4c**. The reader is reminded of the general relationship between current density and diffusional flux to the electrode:

$$i = -nFD_{3+}\,\frac{C_{\mathrm{b}} - C_{3+}}{\delta - x} \qquad [3.9]$$

Rearranging Eq. 3.9,

$$C_{3+}(x) = C_{\mathrm{b}} - \frac{i_1}{nFD_{3+}}(x - \delta) \qquad [3.10]$$

At the outer edge of the boundary layer ($x = \delta$), the concentration of Fe^{3+} is approximately equal to the bulk concentration (≈ 0). Therefore, the initial condition is:

$$t = 0{:}\;\; x \le 0 \le \delta,\;\; C_{3+} = -\frac{i_1}{nFD_{3+}}(x - \delta) \qquad [3.11]$$

where i_1 represents the steady–state current density for Fe^{3+} generation (reaction 3.1) recorded in response to the applied potential in step 1. Note here that the current density recorded in step 1 may also contain contributions from reaction 3.2; however, given the dilute concentrations of Cu^{1+}, the latter contribution is rather small compared to that from reaction 3.1. At the outer edge of the boundary layer ($x = \delta$), the concentration of Fe^{3+} is nearly equal to zero since it is absent in the base electrolyte. Therefore,

$$t > 0: \;\; x = \delta, \;\; C_{3+} \approx 0 \qquad [3.12]$$

At the electrode surface ($x = 0$) during step 2, Fe^{3+} is consumed at a rate equal to i_L^{Cu} per Eq. 3.7. An estimate of i_L^{Cu} available through experiments (refer to **Fig. 3.6**) is $0.16\ \text{mA cm}^{-2}$.

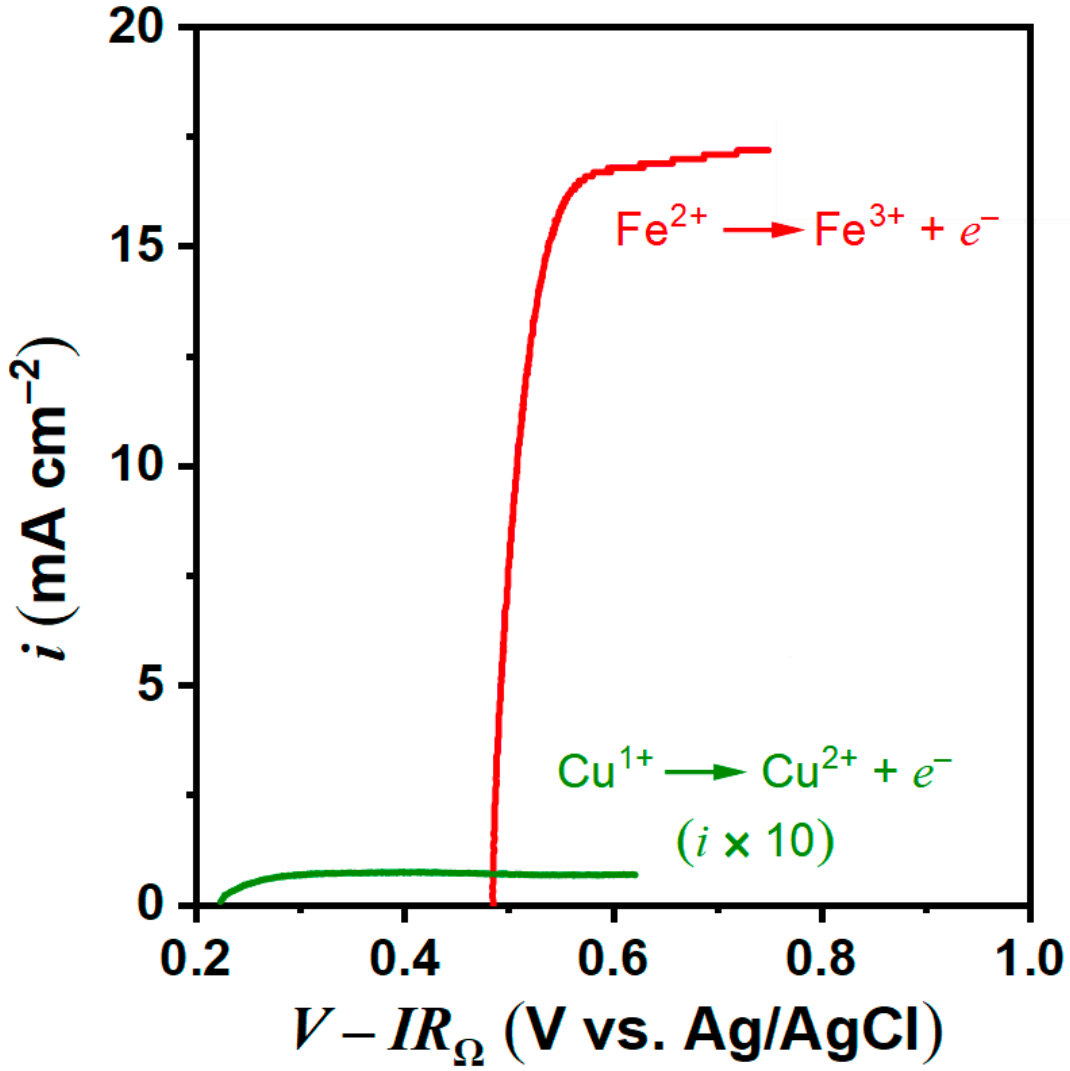

Figure 3.6. Slow–scan voltammograms of equimolar concentrations of 200 mM $FeCl_2$ and $FeCl_3$ (*red*, collected at 10 mV/s) and 1 mM CuCl (*green*, collected at 5 mV/s). In each case, the electrolyte was 500 mM $NaCl_{aq}$ and scans were collected on a Pt RDE rotating at 50 RPM. Due to the low bulk concentration of CuCl, the $Cu^{1+} \rightleftharpoons Cu^{2+} + e^-$ reaction is predominately under diffusion–limitations.

Thus, the boundary condition is:

$$t > 0: \;\; x = 0, \qquad -FD_{3+}\frac{\partial C_{3+}}{\partial x} = 0.16 \times 10^{-3} \qquad [3.13]$$

This provides a concentration gradient of Fe^{3+} near the electrode surface of 0.66 mM cm^{-1}, which is negligibly small in comparison to the average gradient of Fe^{3+} across the boundary layer ($= 44$ M cm^{-1}) implying that the predominant reason for the Fe^{3+} concentration drop is out–diffusion and not interfacial reaction. Given this, a reasonable approximation to the boundary condition at the electrode is:

$$t > 0: \;\; x = 0, \;\; \frac{\partial C_{3+}}{\partial x} \approx 0 \qquad [3.14]$$

Eq. 3.3, together with the initial condition (Eq. 3.11) and boundary conditions (Eqs. 3.12 and 3.14), can be solved by assuming the solution takes the form:

$$C_{3+}(x,t) = \xi(x)\phi(t) \qquad [3.15]$$

The boundary conditions outlined in Eqs. 3.12 and 3.14 then become:

$$C_{3+}(\delta,t) = \xi(\delta)\phi(t) = 0 \qquad [3.16]$$

$$\frac{\partial C_{3+}(0,t)}{\partial x} = \phi(t)\frac{d\xi(0)}{dx} = 0 \qquad [3.17]$$

Using an arbitrary separation constant λ, Eq. 3.8 can be written as:

$$\frac{1}{\phi D_{3+}}\frac{d\phi}{dt} = \frac{1}{\xi}\frac{d^2\xi}{dx^2} = \lambda \qquad [3.18]$$

Solving the temporal derivative, we get:

$$\phi(t) = \exp(\lambda D_{3+} t\,) \qquad [3.19]$$

The spatial derivative is then,

$$\frac{d^2\xi}{dx^2} - \lambda\xi = 0 \qquad [3.20]$$

To avoid the trivial solution, $-\mu^2 = \lambda < 0$. The general solution to Eq. 3.20 is:

$$\xi(x) = c_1\cos(\mu x) + c_2\sin(\mu x) \qquad [3.21]$$

Applying the boundary conditions outlined in Eqs. 3.16–17:

$$c_1 = \cos(\mu_k \delta) = 0, c_2 = 0 \quad [3.22]$$

Therefore,

$$\lambda = -\mu_k^2 = -\left[\frac{(2k+1)\pi}{2\delta}\right]^2 \quad [3.23]$$

Combining Eqs. 3.16, 3.19, 3.21, and 3.22:

$$C_{3+}(x,t) = b_k \sum_{k=0}^{\infty} \cos(\mu_k x) \exp\left(-\mu_k^2 D_{3+} t\right) \quad [3.24]$$

Where b_k is a coefficient given by,

$$b_k = -\frac{2}{\delta} \int_0^{\delta} \frac{i_1}{nFD_{3+}} (x - \delta) \cos(\mu_k x) dx \quad [3.25]$$

Solving Eq. 3.25,

$$b_k = -\frac{2i_1}{nFD_{3+}} \frac{1}{\lambda_k \delta} \quad [3.26]$$

The transport model represented by Eqs. 3.8, 3.11, 3.12, and 3.14 has the following analytical solution for the time–dependent Fe^{3+} concentration at the electrode surface:

$$C_{3+}(0,t) = -\sum_{\mathrm{k}=0}^{\infty} \frac{2i_1}{\lambda_{\mathrm{k}} F \delta D_{3+}} \exp(\lambda_{\mathrm{k}} D_{3+} t) \qquad [3.27]$$

The concentration of Fe^{3+} available from Eq. 3.27 can be inserted in Eq. 3.7 to compute the mixed electrode potential transient in step 2:

$$E = E_{\mathrm{eq}}^{\mathrm{Fe}} - \frac{1}{\alpha_{\mathrm{c}}^{\mathrm{Fe}} f} \ln \frac{i_{\mathrm{L}}^{\mathrm{Cu}}}{\beta [\mathrm{Fe}^{3+}]_{\mathrm{x}=0}} \qquad [3.28]$$

The variation of the mixed potential E as a function of dimensionless time ($t^* = \pi^2 D_{3+} t / 4\delta^2$) measured in experiments (region of interest in **Fig. 3.5**) and computed using the above transport model is shown in **Fig. 3.7**. Parameters needed to compute the potential transient are provided in **Table 3.1**. As noted, good agreement is observed with both approaches yielding a slope dE/dt^* of approximately -0.047 V at short times after step 2 is commenced ($t^* \leq 1$). The rationale for this slope is the time–dependence in Eq. 3.27. Neglecting all terms for which k $>$ 0, we get from Eq. 3.27:

$$[\mathrm{Fe}^{3+}]_{\mathrm{x}=0} \propto \exp\left(-\frac{\pi^2 D_{3+}}{4\delta^2} t\right) \qquad [3.29]$$

Thus, from Eq. 3.28, after differentiation, the expected slope in **Fig. 3.7** is:

$$m_{\text{diff}} = \frac{dE}{dt^*} \approx -\frac{1}{\alpha_c^{\text{Fe}} f} \qquad [3.30]$$

Taking a range of $38.7 \leq f \leq 39.2\ \text{V}^{-1}$ and the typical range of cathodic transfer coefficients $0.45 \leq \alpha_c^{\text{Fe}} \leq 0.55$, the slope $m_{\text{diff}} = dE/dt^*$ is within the range: $-0.0574 \leq m_{\text{diff}} \leq -0.0463$ V and is consistent with the experimentally observed slope seen in **Fig. 3.7**. Additionally, from Eqs. 3.28 and 3.30, the slope of the potential transient depends only on the precise values of α_c^{Fe} and f, whereas values of i_L^{Cu}, β, and $[\text{Fe}^{3+}]_{x=0}$ only alter the initial electrode potential. This case study ('no adsorption') demonstrates that the potential relaxation rate (step 2) after Fe^{2+} oxidation in the presence of $\text{Cu}^{1+}/\text{Cu}^{2+}$ is governed by diffusional transport (parameters in **Table 3.1**). If adsorbed species are present, and their desorption via reaction is slow, then the potential relaxation rate would be altered. In the subsequent section, this rate is measured in the presence of adsorption (of HT^+) so as to characterize its effects during chronopotentiometry.

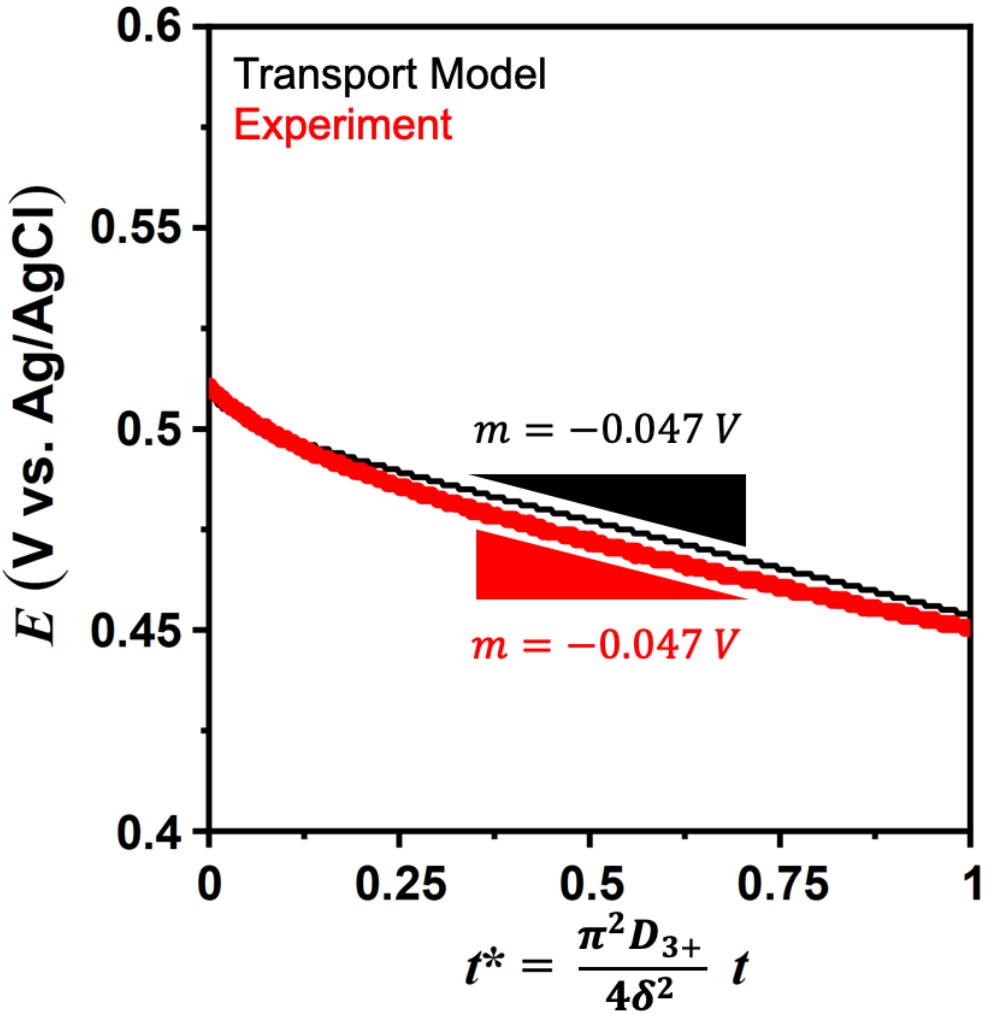

Figure 3.7. The experimental (*red*) and simulated (*black*) mixed potential of Fe^{3+} consumption and its evolution with time (dimensionless) for case (i), *i.e.*, re–equilibration of the Au electrode with Cu^{1+}/Cu^{2+} following Fe^{2+} oxidation. Here $t^* = 0$ when the open circuit step in **Fig. 3.5** is initiated. The slope of the experimental potential transient agrees well with that predicted by the transport model of Eq. 3.30.

Table 3.1. Parameters used in computing the potential transient in **Fig. 3.7** via Eq. 3.28.

Parameter	Value	Source
$i_{\mathrm{L}}^{\mathrm{Cu}}$	$0.16\ \mathrm{mA\ cm^{-2}}$	**Fig. 3.6**
$\beta = i_0^{\mathrm{Fe}}/[\mathrm{Fe}^{3+}]_{\mathrm{ref}}$	$1\ \mathrm{A\ cm\ mol^{-1}}$	Assumed
$\alpha_{\mathrm{c}}^{\mathrm{Fe}}$	0.55	Ref. 66
$E_{\mathrm{eq}}^{\mathrm{Fe}}$	$0.49\ \mathrm{V\ vs.\ Ag/AgCl}$	**Fig. B.2**
i_1	$5.5\ \mathrm{mA\ cm^{-2}}$	Inset of **Fig. 3.5**
D_{3+}	$2.4 \times 10^{-6}\ \mathrm{cm^2\ s^{-1}}$	**Fig. B.2**
δ	45 μm	Eq. B2

Case (ii): We now consider the case where adsorption onto to the electrode surface occurs during electro–oxidation. As shown via eSERS in **Fig. 3.3**, the HT–oxidation reaction involves adsorption of the product HT^+ on Au. Similar to case (i), a two–step experiment was performed in which first a constant potential of $0.65\ \mathrm{V\ vs.\ Ag/AgCl}$ was applied to facilitate HT oxidation. Since the electrolyte contained $200\ \mathrm{mM}$ HT and $1\ \mathrm{mM}$ each of CuCl and $\mathrm{CuCl_2}$, the following reactions proceed at the Au electrode (**Fig. 3.8a**):

$$\mathrm{HT} + \mathrm{S} \rightarrow [\mathrm{HT}_{\mathrm{ads}}^{+} - \mathrm{S}] + e^{-} \qquad [3.31]$$

$$\mathrm{Cu}^{1+} \rightarrow \mathrm{Cu}^{2+} + e^{-} \qquad [3.32]$$

where "S" refers to an adsorption site on the Au electrode surface, and "ads" refers to the adsorbed state of the oxoammonium cation. Following HT oxidation, the electrode

potential is released and the surface mixed potential under open circuit condition is tracked as a function of time. During this step of chronopotentiometry, the electrode undergoes the following redox process (**Fig. 3.8b**):

$$\text{Oxidation: } Cu^{1+} \rightarrow Cu^{2+} + e^{-} \quad [3.33]$$

$$\text{Reduction: } [HT^{+}_{ads} - S] + e^{-} \rightarrow HT + \text{site} \quad [3.34]$$

$$\text{Overall reaction: } [HT^{+}_{ads} - S] + Cu^{1+} \rightarrow HT + Cu^{2+} + S \quad [3.35]$$

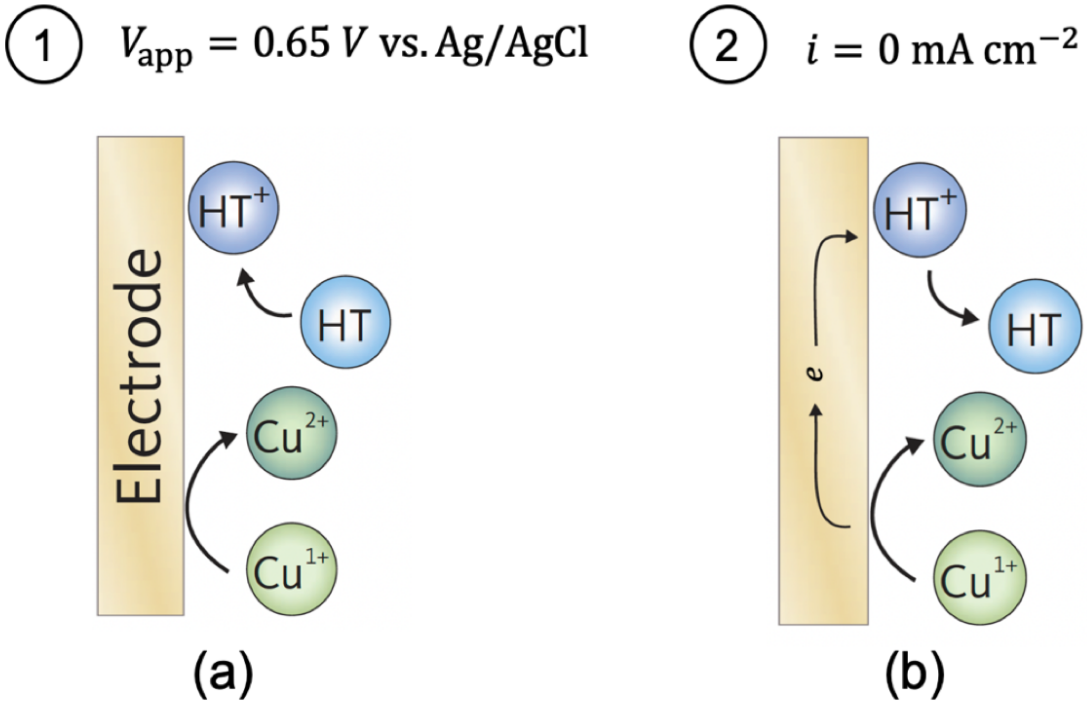

Figure 3.8. (a) In step 1, an oxidative potential (0.65 V vs. Ag/AgCl) is applied to the working electrode such that Cu^{1+} and HT are oxidized to Cu^{2+} and adsorbed HT^{+}, respectively, (b) In step 2, under open circuit conditions, Cu^{1+} is spontaneously oxidized to Cu^{2+}. Simultaneously, the adsorbed HT^{+} is reduced to HT, which is desorbed from the electrode.

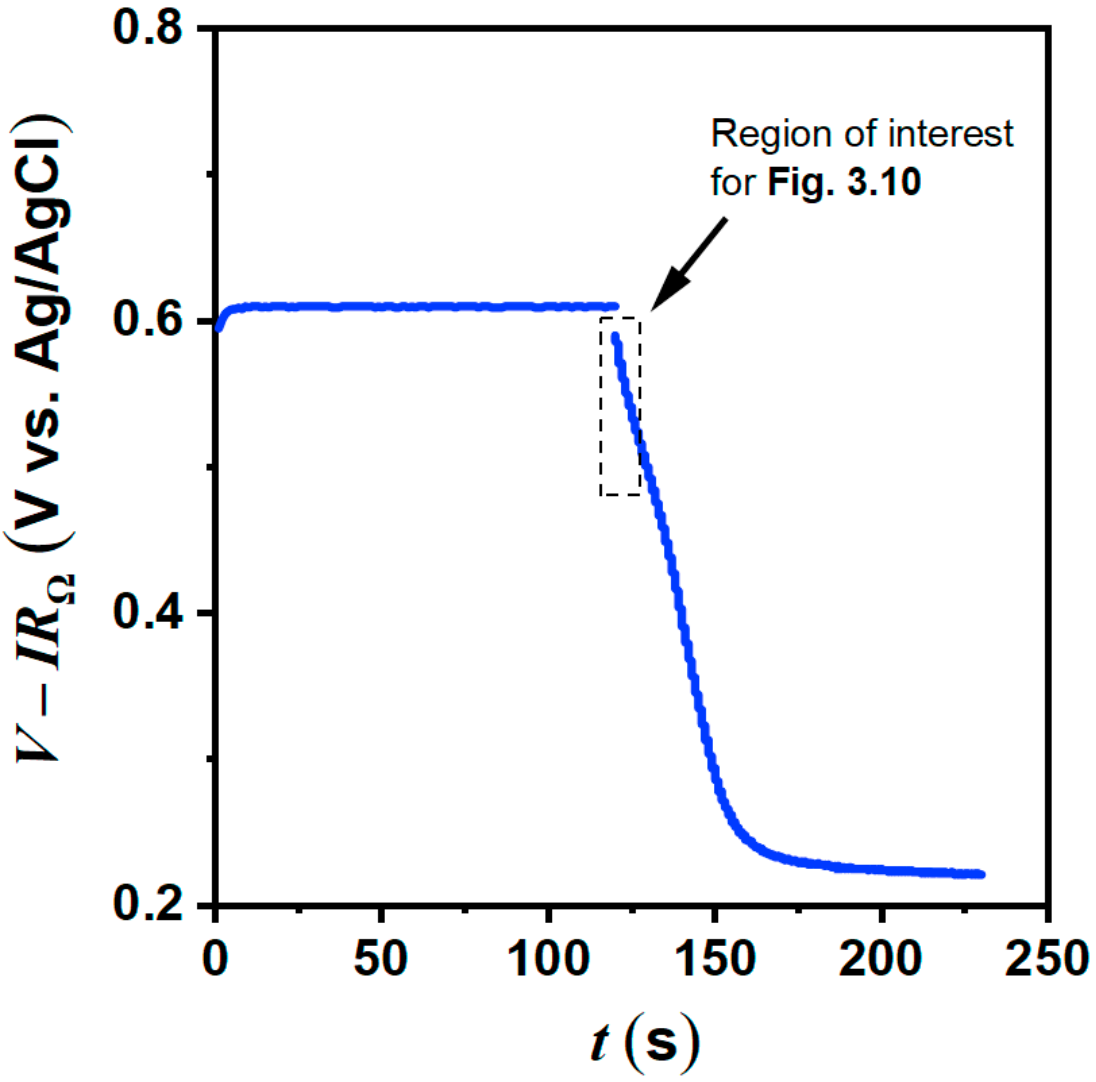

Figure 3.9. The potential transient for 200 mM HT in 500 mM $NaCl_{aq}$ collected on a Au RDE rotating at 50 RPM. The electrode was held at 0.65 V vs. Ag/AgCl for 120 s, and then released to open circuit conditions. The region of interest for **Fig. 3.10** is marked.

The measured potential versus time trend during this two–step experiment is shown in **Fig. 3.9**. The surface mixed potential when reactions 3.33 – 3.35 proceed is dictated by the charge balance:

$$r_{\text{ox}} = r_{\text{red}} \qquad [3.6] \text{ (revisited)}$$

Because the oxidation product HT^+ adsorbs on the electrode surface and a fraction θ of available adsorption sites become occupied, only a fraction $(1-\theta)$ of the sites are available for the $Cu^{1+} \rightarrow Cu^{2+} + e^-$ reaction. But, for relatively small values of θ, Cu^{1+} oxidation is still largely diffusion–limited. Applying the Tafel equation to represent the kinetics of individual reactions 3.33 and 3.34, we get:

$$i_{\mathrm{L}}^{\mathrm{Cu}} = i_0^{\mathrm{HT}}\theta \exp\left(-\alpha_{\mathrm{c}}^{\mathrm{HT}} f(E - E_{\mathrm{eq}}^{\mathrm{HT}})\right) \qquad [3.36]$$

where i_0^{HT} is the exchange current density, θ is the fractional surface coverage of HT^+, $\alpha_{\mathrm{c}}^{\mathrm{HT}}$ and $E_{\mathrm{eq}}^{\mathrm{HT}}$ are the cathodic charge transfer coefficient and equilibrium potential of reaction 3.34. During step 2, HT^+ coverage decreases via desorption. To a first–order approximation, the desorption rate is proportional to HT^+ coverage:

$$\frac{d\theta}{dt} \approx -k_{\mathrm{des}}\theta \qquad [3.37]$$

where k_{des} is the desorption rate constant. The approximation in Eq. 3.37 is introduced because other factors such as electrode potential which also influence desorption are ignored for the sake of simplicity. Initially $(t = 0)$, *i.e.*, at the beginning of step 2, the surface coverage θ of HT^+ is assumed to be an arbitrary selected value θ_0. Thus, the solution to Eq. 3.37 is:

$$\theta \approx \theta_0 \exp(-k_{\mathrm{des}}t) \qquad [3.38]$$

Eqs. 3.36 and 3.38 represent a set of coupled equations, which provide the time–evolution of the surface potential for a desorption–limited process:

$$E \approx E_{\mathrm{eq}}^{\mathrm{HT}} - \frac{1}{\alpha_{\mathrm{c}}^{\mathrm{HT}} f} \ln\left(\frac{i_{\mathrm{L}}^{\mathrm{Cu}}}{i_0^{\mathrm{HT}} \theta_0}\right) - \frac{k_{\mathrm{des}} t}{\alpha_{\mathrm{c}}^{\mathrm{HT}} f} \qquad [3.39]$$

Differentiating provides the rate of change of potential:

$$m_{\mathrm{des}} = \frac{dE}{dt^*} \approx -\frac{k_{\mathrm{des}} 4\delta^2}{\alpha_{\mathrm{c}}^{\mathrm{HT}} f \pi^2 D_{\mathrm{HT}}} \qquad [3.40]$$

Here, D_{HT} is the diffusion coefficient of HT (refer to **Fig. B.3**). This expression for m_{des} (for a process incorporating adsorption–desorption) is noticeably different than that for m_{diff} (Eq. 3.30, for a process involving diffusion but no adsorption effects). The following relationship emerges:

$$|m_{\mathrm{des}}| \approx |m_{\mathrm{diff}}| \frac{k_{\mathrm{des}}}{\left(\frac{\pi^2 D_{\mathrm{HT}}}{4\delta^2}\right)} = |m_{\mathrm{diff}}| \frac{k_{\mathrm{des}}}{k_{\mathrm{diff}}} \qquad [3.41]$$

Eq. 3.41 recognizes the fact that $\pi^2 D_{\mathrm{HT}}/4\delta^2$ is analogous to an equivalent diffusion rate constant. In a desorption–limited process, as in HT electro–oxidation, we expect $k_{\mathrm{des}} < k_{\mathrm{diff}}$ and thus $|m_{\mathrm{des}}| < |m_{\mathrm{diff}}|$. Indeed, **Fig. 3.10** confirms that this expected relationship is observed in the chronopotentiometry data. Specifically, the magnitude of the potential change (dE/dt^*) is 0.0321 V for potential relaxation following HT oxidation,

and thus lesser in magnitude compared to the diffusion–limited case of Fe^{2+} oxidation (0.0466 V).

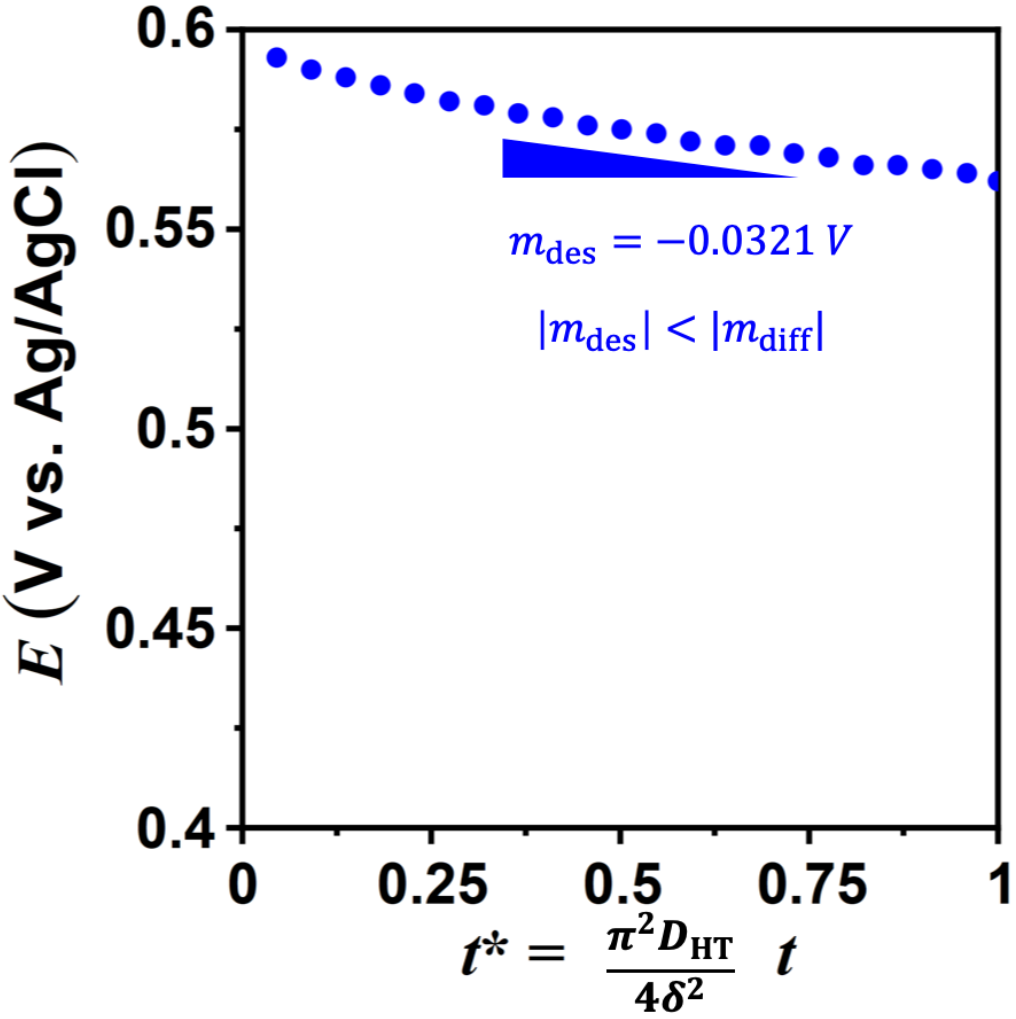

Figure 3.10. The experimentally measured mixed potential during HT^+ desorption and its evolution with time (dimensionless) for case (ii), i.e., re–equilibration of the Au electrode with Cu^{1+}/Cu^{2+} following HT oxidation. Here, $t^* = 0$ when the open circuit step in **Fig. 3.9** is initiated. Note that the rate of change of potential is smaller in magnitude compared to case (i).

Similar slopes were also measured on Pt and GC electrodes (**Fig. 3.11**). The lower magnitude of the rate of potential change suggests that slow desorption of adsorbed HT^+

(via reaction with Cu^{1+}) and not out–diffusion is the rate–limiting process during gradual re–equilibration of the Au electrode surface following HT oxidation.

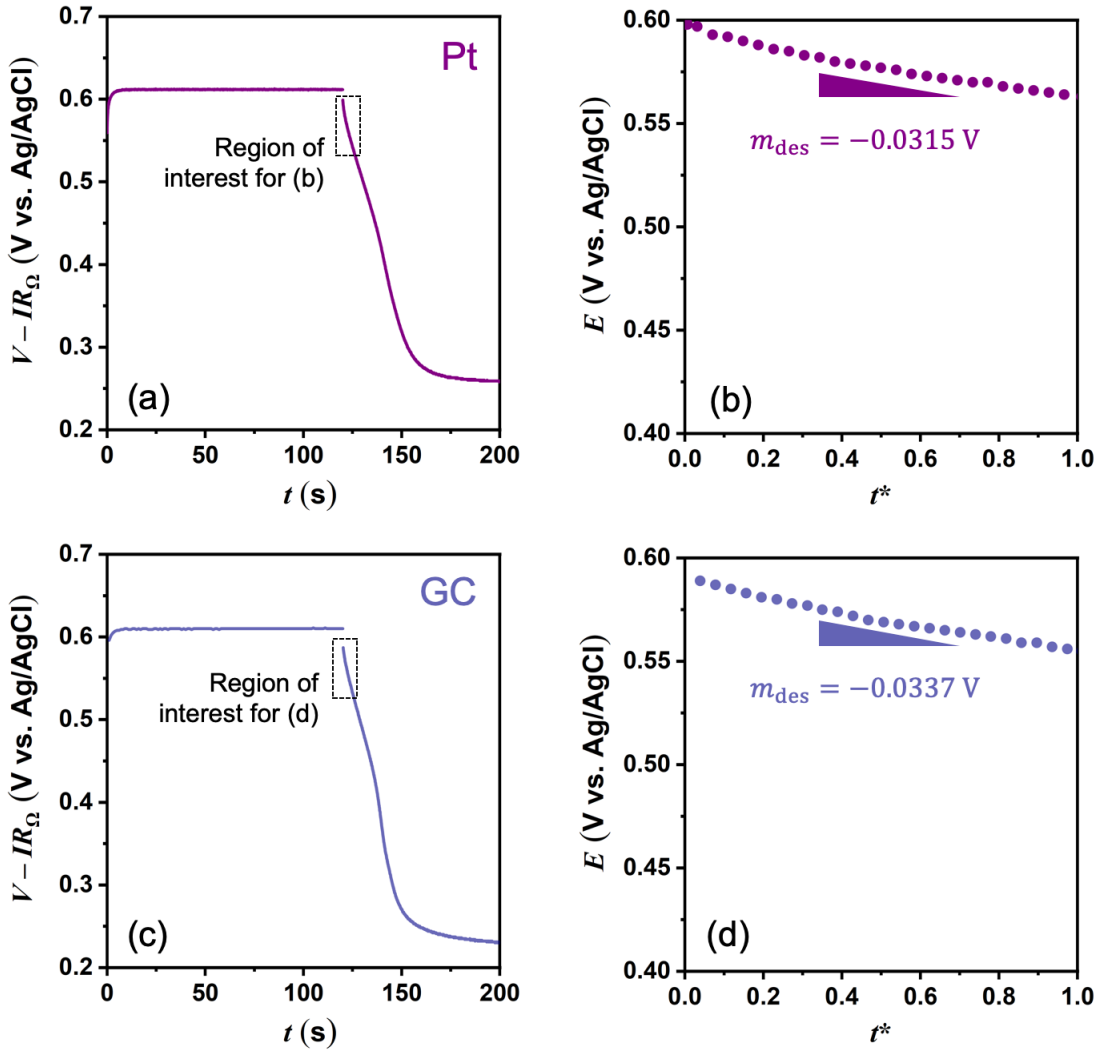

Figure 3.11. In step 1, a potential step (0.65 V vs. Ag/AgCl) is applied to the (a) Pt and (c) GC working electrode for 120 s such that Cu^{1+} and HT are oxidized to Cu^{2+} and HT^{+}, respectively. In step 2, the potential transient is recorded at open circuit conditions. The potential transient recorded in step 2 is plotted against dimensionless time t^* for (b) Pt and (d) GC.

3.4.2. Long time scales: variable potential transient response

Fig. 3.12 compares the potential transient at long time scales of the (a) diffusion– and (b) desorption–limited cases at various applied potentials. As expected, in the diffusion–limited case, the potential response is independent of the applied potential in step 1. In the desorption–limited case, the potential transient appears to vary with variable applied potential. In Chapter 2, it was shown that the surface coverage θ of HT^+ increases with increasing electrode potential E. Thus, in the desorption–limited case, we can expect the re–equilibration time to increase with an increase in applied potential. Rearranging Eq. 3.38,

$$t \approx \frac{1}{k_{\mathrm{des}}} \ln\left(\frac{\theta_0}{\theta}\right) \qquad [3.42]$$

Eq. 3.42 recognizes that for a fixed value of θ, t is large when θ_0 is large. **Fig. 3.12b** confirms that this expected relationship is observed, as the electrode re–equilibrates after a much longer time when released from a higher oxidative potential.

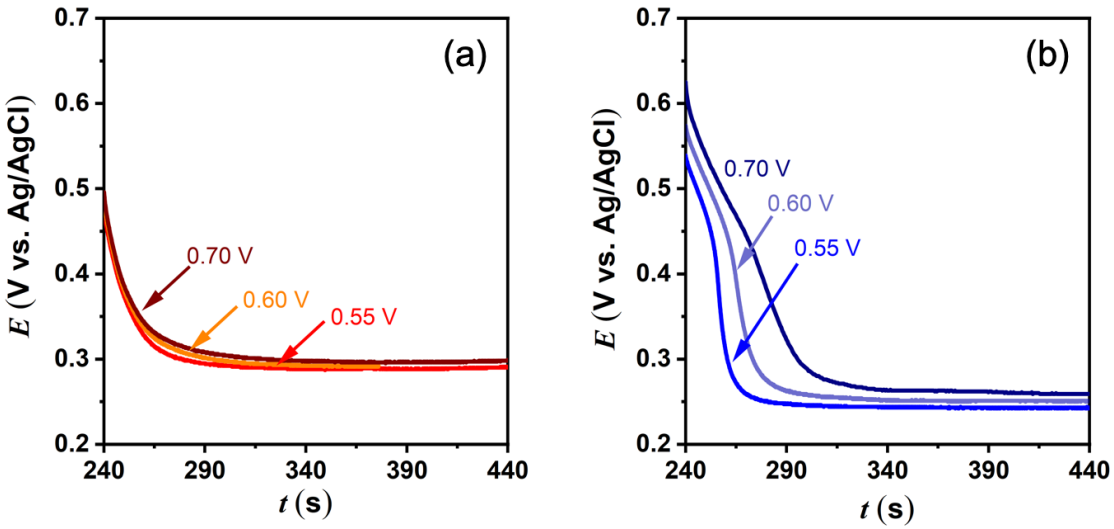

Figure 3.12. The potential transient for (a) 200 mM $FeCl_2$ and (b) 200 mM HT in 500 mM $NaCl_{aq}$ collected on a Pt RDE rotating at 50 RPM. The electrode was held at various oxidative potentials (0.70, 0.60, or 0.55 V vs. Ag/AgCl) for 120 s, and then released to open circuit conditions. In the diffusion–limited case, the potential–transient response is independent of applied potential. In the desorption–limited case, the re–equilibration time increases as the applied potential increases.

3.4.3. Contributions from the homogeneous reaction

In section 3.4.1, the slope of the potential transient was determined analytically and compared against experiment, and excellent agreement between theory and experiment are noted. However, in the transport model, we neglect contributions from the homogeneous reaction: $Fe^{3+} + Cu^{1+} \rightarrow Cu^{2+} + Fe^{2+}$. This reaction occurs away from the electrode surface and is illustrated in **Fig. 3.13**.

We remind the reader that, in the 'no adsorption' case, the slope of the potential transient $m_{\text{diff}} = dE/dt^*$ ranges from: $-0.0574 \leq m_{\text{diff}} \leq -0.0463$ V. Incorporating the homogeneous reaction given by Eq. 3.5 in the transport model would only accelerate the consumption of Fe^{3+}. This manifests as an increase in the magnitude of the slope m_{diff}, and further exacerbate the departure of the desorption–limited case ($m_{\text{des}} \sim -0.03$ V) from that predicted by the transport model.

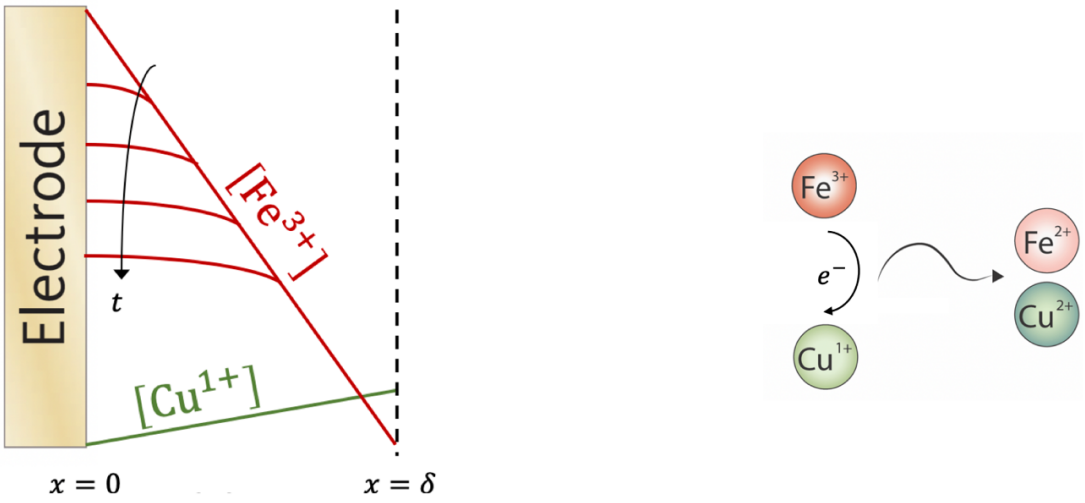

Figure 3.13. Schematic representation of step 2 (i = 0 mA cm^{-2}) of the 'no adsorption' case. Fe^{3+} near the electrode surfaces diffuses away from the electrode surface (x = 0), and away from the electrode Fe^{3+} is consumed through the homogeneous electron transfer reaction given in Eq. 3.5.

3.5. Conclusions

The adsorption–desorption mechanism proposed in Chapter 2 for electro–oxidation of nitroxide radical containing organics was investigated further using transient electrochemical techniques. This study led to the following key conclusions:

(i) At short time scales after electrochemical oxidation is terminated, the normalized time–derivative of the potential relaxation curve for a diffusion–limited process is shown to be $-0.0466\ \mathrm{V}$. However, the slope for the case of HT oxidation is only $-0.0321\ \mathrm{V}$, *i.e.*, slower relaxation than that for the diffusion case, suggesting that the potential transient is controlled by sluggish non–diffusional processes such as desorption of adsorbed species.

(ii) At long time scales, the potential transient for a desorption–limited approaches a shoulder prior to relaxing to the initial open circuit potential ($0.25\ \mathrm{V}$ vs. Ag/AgCl). This shoulder is not observed in the diffusion–limited case. This suggests that a transient equilibrium is established between the adsorbed organic and the electrolyte.

(iii) The magnitude of the potential relaxation rate is largely independent of the substrate material, and differs only by a few millivolts between Au, Pt, and GC electrodes. This implies that the adsorption–desorption mechanism may be inherent to the molecule itself, and that synthetically tuning its structure may be necessary to mitigate desorption limitations for practical applications of nitroxide–containing redox active organics in batteries.

In summary, the eSERS and electrochemical investigations reported herein and their analysis further provide support to the adsorption–desorption mechanism for HT electro–oxidation proposed in Chapter 2.

Chapter 4. Electrochemical and spectroscopic investigation of electrode passivation during electro–oxidation of HT

In Chapter 3, spectroscopic and electrochemical evidence was presented in support of the adsorption–desorption mechanism proposed in Chapter 2. Mathematical modeling of the electrochemical data was used to highlight the slow desorption of HT^+ from the electrode surface.

In this chapter, electrochemical evidence is presented that suggests the presence of a surface passivating film. Through Fourier transform infrared spectroscopy (FTIR), the presence of carbonyl functional groups implies the chemical oxidation of the hydroxyl moiety.

4.1. Experimental procedure

4.1.1. Materials

Sodium chloride (NaCl, $\geq 99\%$ purity, Sigma–Aldrich), TEMPO (T, $C_9H_{18}NO$, 99%, Sigma–Aldrich), 4–hydroxy–TEMPO (HT, $C_9H_{18}NO_2$, $> 99\%$ purity, Alfa Aesar) and 4–oxo–TEMPO (OT, $C_9H_{16}NO_2$, $\geq 90\%$ purity, Sigma–Aldrich) were used as received.

4.1.2. Methods

Electrolyte preparation: Aqueous electrolytes containing 500 mM NaCl were prepared using Millipore ultrapure (18.2 MΩ · cm) deionized water and de–aerated by purging Ar gas. Appropriate amounts of the electroactive materials were dissolved in the aqueous electrolyte.

Electrochemical measurements: Steady–state polarization and chronoamperometry experiments were performed in a standard three–electrode configuration. The working electrode was a 5 mm diameter polycrystalline Pt rotating disk electrode (RDE, Pine Research Instrumentation). Prior to each electrochemical experiment, the exposed electrode surface was mechanically polished first using 1 μm followed by 0.3 μm alumina slurry, then sonicated in deionized water. The counter electrode was a graphite rod, and the reference electrode was saturated Ag/AgCl (Fisher Scientific). An AutoLAB PGSTAT302N was used for all electrochemical experiments. IR_{Ω}– correction was applied to steady–state data during post–processing using $R_{\Omega} = 20\ \Omega$.

Fourier Transform Infrared Spectroscopy (FTIR): A Nicolet iS50 FTIR (Thermo Scientific) spectrometer equipped with a MCT–high D* detector and KBr beamsplitter was used to collect *ex situ* spectra of the samples. Each measurement consisted of 400 scans collected at 8 cm^{-1} resolution. Aliquots of solutions containing HT or OT were drop cast directly onto the Pt electrode. To ensure the spectrum of the passivated electrode was representative of the surface film, the electrode was rinsed with excess de–ionized water and dried under a stream of Ar gas.

4.2. Voltage–induced electrode passivation investigated using electrochemical cycling and amperometry

Fig. 4.1 shows 5 cycles of slow–scan ($0.5\ \mathrm{mV/s}$) voltammograms corresponding to the electrochemical oxidation of HT on a Pt RDE rotating at 900 RPM. Under such conditions, pseudo steady–state behavior is expected wherein the limiting current density i_{L} is observed at high overpotentials. However, during the first scan in **Fig. 4.1**, a peak in the current density is observed at $0.85\ \mathrm{V\ vs.\ Ag/AgCl}$. At this potential, the measured current density is $i = 40\ \mathrm{mA\ cm^{-2}}$, *i.e.*, approximately $0.5 \cdot i_{\mathrm{L}}$. Moreover, the magnitude of the current density decays with each subsequent cycle. Such observations have been previously reported in literature[69–71] and attributed to the formation of passivating films on the electrode surface. In one study, Kiss et al.[71] conducted a similar cycling experiment to investigate electrode passivation during electro–oxidation of phenol. Similar to **Fig. 4.1**, they show a significant current decay in cycles $2-5$ in comparison to cycle 1. It is important to note that phenols are known to weakly adsorb to electrode surfaces.[69] The passivation hypothesis is further supported by analyzing the overpotential required to drive a current density of $i = 2\ \mathrm{mA\ cm^{-2}}$. Between cycles 1 and 5, the overpotential increases by $0.16\ \mathrm{V}$, further highlighting the blocking effect of the surface film.

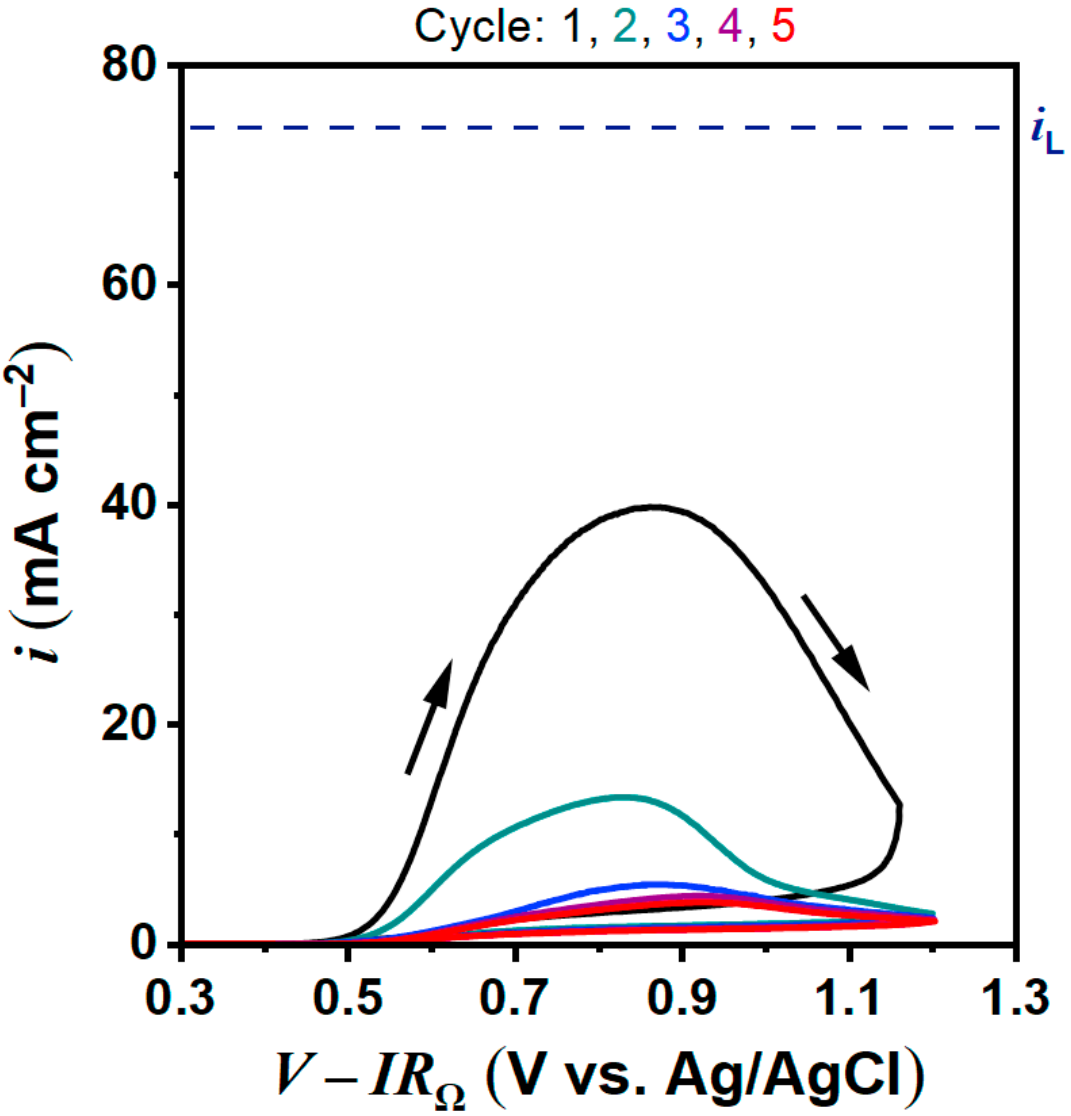

Figure 4.1. Slow–scan (0.5 mV/s) cyclic voltammetry of 200 mM HT in 500 mM $NaCl_{aq}$ collected on a Pt RDE rotating at 900 RPM. The voltammogram deviated from the expected steady–state behavior and showed signatures of a surface passivating film.

Now, we revisit the adsorption–desorption mechanism proposed in Chapter 2 wherein the overall rate expression for HT electro–oxidation is:

$$i = Fk_{\mathrm{des}}\theta \approx Fk_{\mathrm{des}}\mathrm{K_{eq}}C_{\mathrm{HT}}e^{f(E-E_{\mathrm{eq}})} \qquad [2.15] \text{ (revisited)}$$

From Eq. 2.15, we expect a steady–state current density i during a fixed potential E step experiment. This was previously observed throughout Chapter 3. **Fig. 4.2** shows the current response to various applied potentials. As expected from Eq. 2.15 and **Fig. 3.11a**, when a low anodic potential (0.65 V vs. Ag/AgCl) was applied, a constant current density i was recorded. However, when the applied potential increased to 1.1 and 1.25 V vs. Ag/AgCl, the current rapidly decayed toward zero. From **Figs. 4.1** and **4.2**, it is clear that a voltage–induced film has formed and is blocking the surface.

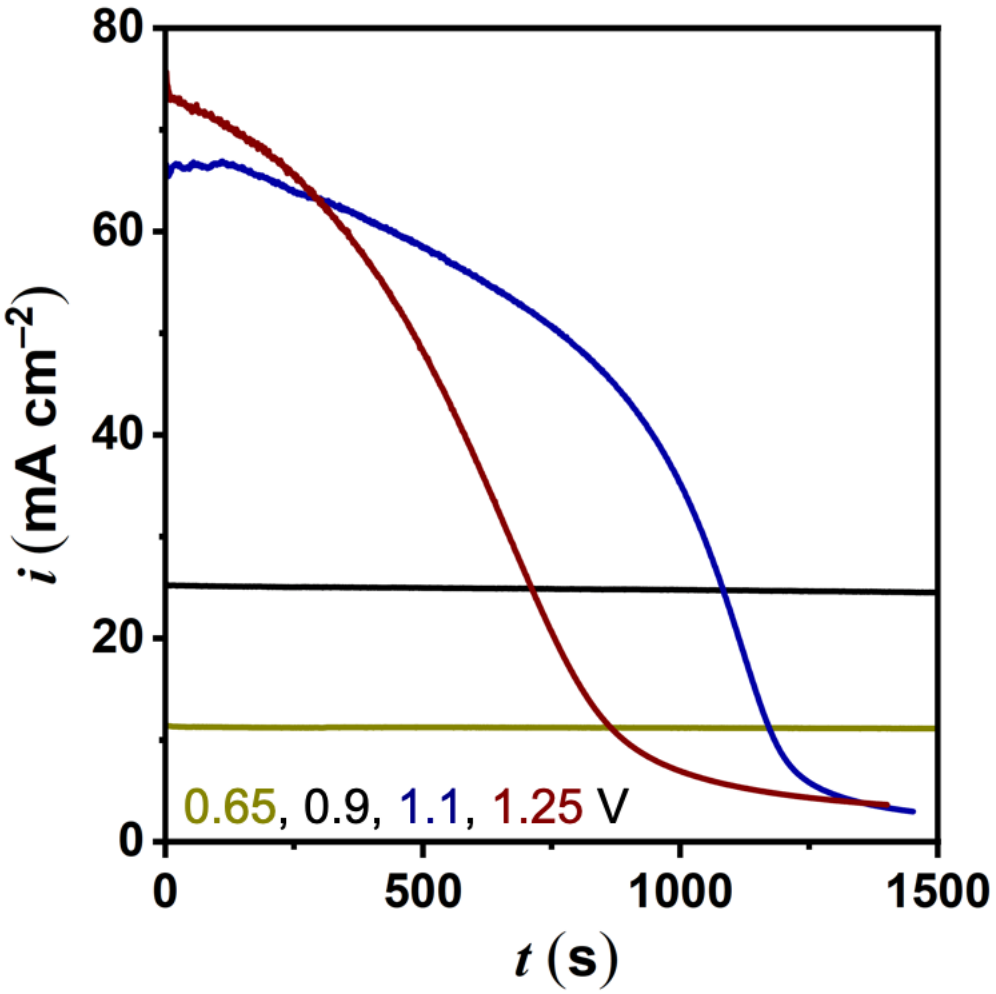

Figure 4.2. The current transient response to various applied potentials on a Pt RDE rotating at 900 RPM. The electrolyte contained 200 mM HT in 500 mM $NaCl_{aq}$. The electrode was passivated when a large anodic potential was applied.

Further building upon the adsorption–desorption mechanism (Eqs. 2.8 and 2.9), we now propose the electrode deactivation reaction (Eq. 4.1):

$$\mathrm{HT} + \mathrm{S} \rightleftharpoons [\mathrm{HT}^{+}_{\mathrm{ads}} - \mathrm{S}] + e^{-} \qquad [2.8]\ \text{(revisited)}$$

$$[\mathrm{HT}^{+}_{\mathrm{ads}} - \mathrm{S}] \rightarrow \mathrm{HT}^{+} + \mathrm{S} \qquad \text{[2.9] (revisited)}$$

$$[\mathrm{HT}^{+}_{\mathrm{ads}} - \mathrm{S}] + \mathrm{R_u} \rightarrow \mathrm{P_{ads}} \qquad [4.1]$$

Here, $\mathrm{P_{ads}}$ is the surface passivating product adsorbed to the electrode and $\mathrm{R_u}$ is an unknown reactant ($\mathrm{HT}^{+}_{\mathrm{ads}}$, HT, or $\mathrm{H_2O}$). When $\mathrm{P_{ads}}$ accumulates on the electrode surface, it passivates θ_{P} sites. These sites are blocked from participating in the electro–oxidation reaction, thereby decreasing θ and ultimately i. This process is illustrated schematically in **Fig. 4.3** below.

.

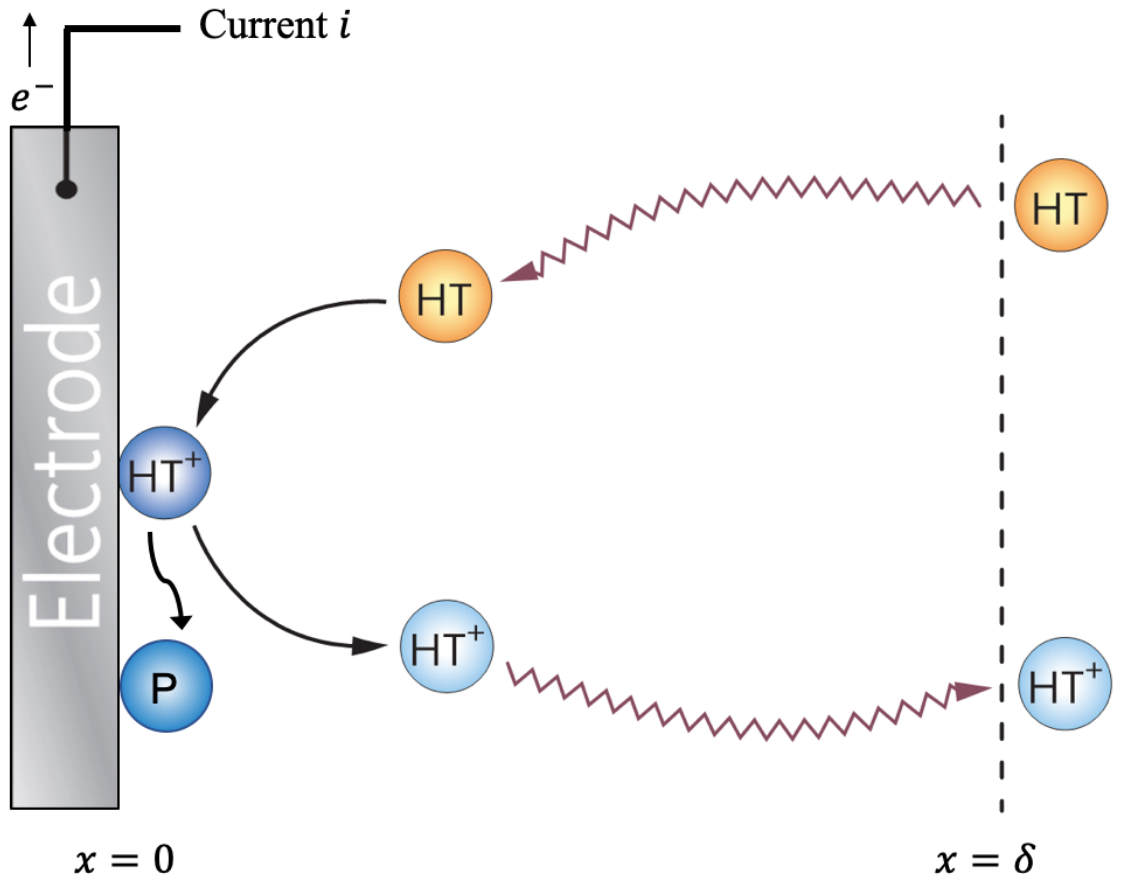

Figure 4.3. Schematic of the proposed adsorption–desorption–deactivation model for HT electro–oxidation involving charge transfer and adsorption of product HT^+, followed by two competing steps (i) slow desorption of HT^+ which then diffuses away from the electrode, and (ii) formation of product P that passivates the electrode surface.

To deconvolute factors contributing to the formation of the passivating film, chronoamperometry within the mass transport limited region ($V_{app} = 1.25$ V vs. Ag/AgCl) was performed. The current transient response is shown in **Fig. 4.4** for high (200 mM) and low (50 mM) concentrations of HT and T. Note that, regardless of bulk concentration of HT, the current decays rapidly to ~4 mA cm^{-2}. This decay occurs over similar time scales suggesting electrode passivation is largely independent of C_b. In

comparison, the current transient of T (*black*) remains constant and in good agreement with the diffusion–limited current density reported in literature.[20] This suggests that the hydroxyl functional group present in the para (or 4) position of HT participates in the passivation reaction. The role of the $-OH$ moiety was investigated further using spectroscopic techniques discussed in the proceeding section.

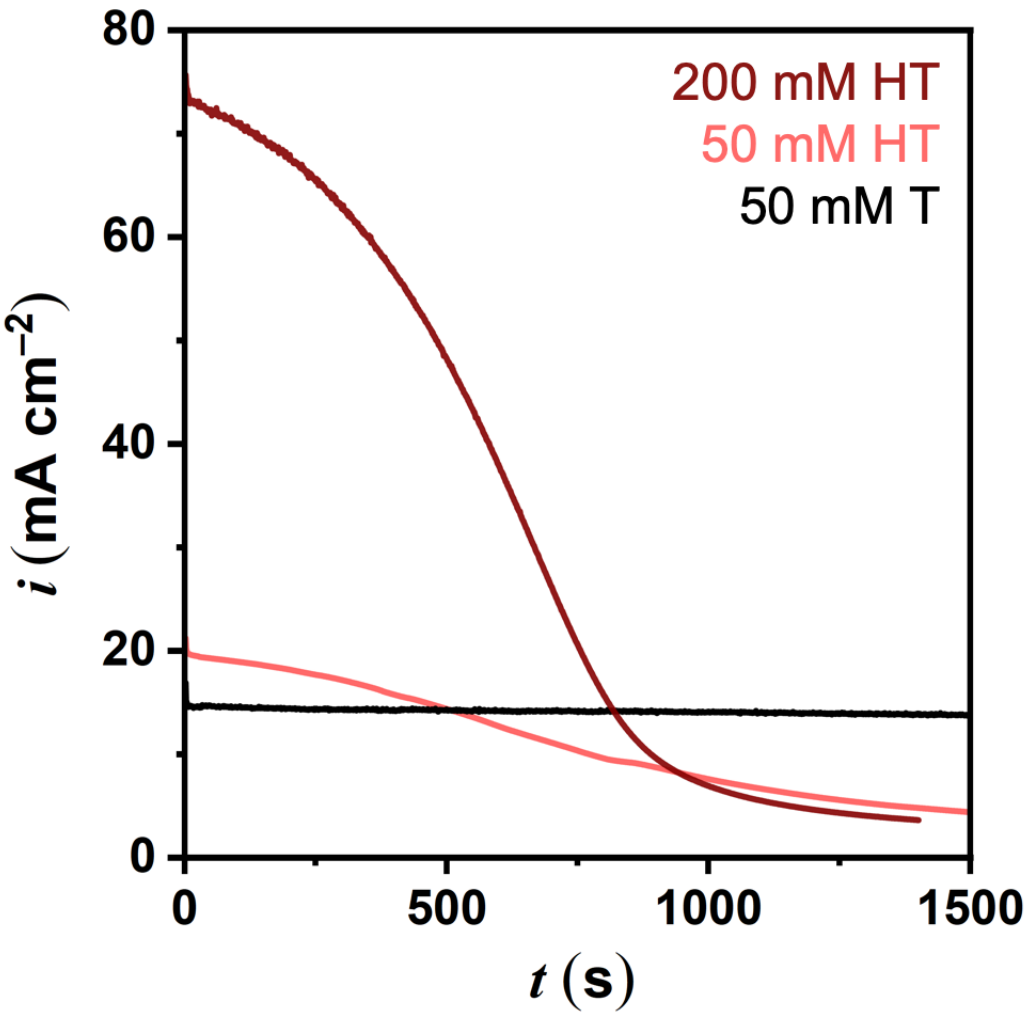

Figure 4.4. The current transient response to an applied potential V_{app} = 1.25 V vs. Ag/AgCl on a Pt RDE rotating at 900 RPM. The electrolyte contained the appropriate amount of T (*black*) or HT (200 mM – *maroon*, 50 mM – *red*) in 500 mM $NaCl_{aq}$. The electrode was passivated only in the HT–containing electrolyte, suggesting the hydroxyl functional group mediates electrode passivation.

4.3. Film characterization

Fourier transform infrared (FTIR) spectroscopy was used to characterize the structure of the blocking film. **Fig. 4.5** compares three cases: (1) HT (top – *green*), (2) the passivating film formed at 1.25 V (middle – *maroon*), and (3) OT (bottom – *black*).

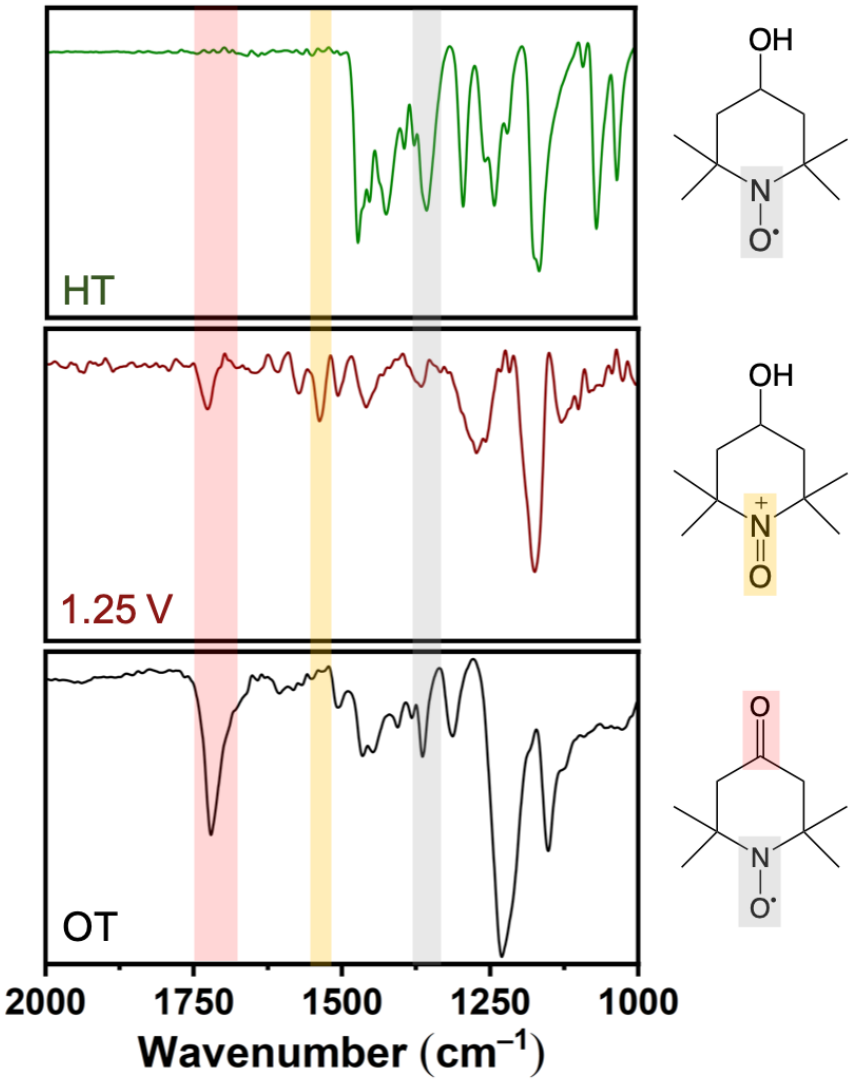

Figure 4.5. *Ex situ* FTIR spectra of HT (top panel – *green*), the passivated electrode (middle panel – *maroon*), and OT (bottom panel – *black*). Following electro–oxidation of HT at 1.25 V vs. Ag/AgCl, a FTIR peak at 1721 cm^{-1} appears, suggesting chemical oxidation of the –OH moiety.

In the top and bottom panels, a peak at $1353\ cm^{-1}$ and $1363\ cm^{-1}$ can be assigned with reasonable certainty to the $N-O^{\cdot}$ stretching vibration of HT and OT, respectively.[72,73] A peak at $1537\ cm^{-1}$ is observed in the passivated electrode's spectrum and represents the $N^{+}=O$ stretching vibration.[74] This peak is expected given the adsorption–desorption

mechanism proposed in Chapter 2 and the experimental evidence presented in Chapter 3. Finally, a sharp peak is observed at $1727\ \mathrm{cm}^{-1}$, suggesting the formation of a carbonyl–containing species. This is in good agreement with the peak at $1721\ \mathrm{cm}^{-1}$ in the bottom panel corresponding to the carbonyl stretching vibration of OT. It is important to note that the oxoammonium cation is known to catalyze the oxidation of primary and secondary alcohols.[75] Given this, an analogous mechanism is expected wherein autocatalysis of $\mathrm{HT}^{+}_{\mathrm{ads}}$ produces a carbonyl containing species.

4.4. Conclusions

In this chapter, evidence of a surface passivating film forming is presented:

(i) During ultra–slow–scan electrochemical cycling, the overpotential required to drive an equivalent amount of current increased with each subsequent cycle. Additionally, a peak was observed in the current density, *i.e.*, a significant deviation from the expected steady–state limiting current plateau.

(ii) The current decayed during electro–oxidation of HT at time scales of several hundred seconds. This current decay was not observed in the case of T electro–oxidation. This suggests the electrode passivation is mediated by the $-\mathrm{OH}$ moiety.

(iii) The presence of a carbonyl functional group was observed using *ex situ* FTIR spectroscopy. This further supports the electrochemical data wherein HT electro–oxidation passivated the electrode, whereas T did not.

5.1. Summary

Pseudo steady–state voltammograms collected under a variety of conditions were used to extract the anodic charge transfer coefficient α_a associated with the electro–oxidation of HT. To explain the unusual value of α_a ($\rightarrow 1$) regardless of operating condition, an adsorption–desorption mechanism wherein the electro–oxidation of HT is adsorption–mediated and desorption–limited. Numerical modeling captured the implications of the mechanism on transient CV characteristics.

Evidence in support of the mechanism was then collected using a combination of *in situ* electrochemical surface enhanced Raman spectroscopy (eSERS), potentiometry, and mathematical modeling. *In situ* eSERS confirmed the slow desorption of the oxidation product from the electrode surface. A tracer couple was used to track the slow desorption of the oxoammonium ion from the electrode during potentiometry. Mathematical modeling comparing the diffusion– and desorption–limited cases was conducted, and further captured the adsorption–desorption mechanism.

Signatures of a passivating film were observed during electrode cycling of the model ROM: a higher overpotential was required to drive the same current, and the current decayed with successive cycling. The current decayed toward zero in amperometry performed at various operating conditions for HT. In comparison, the current density did not decay in the case of TEMPO. *Ex situ* FTIR confirmed the oxidation of the hydroxyl group to a carbonyl, further supporting the amperometry and cycling data.

5.2. Future outlook

RFBs provide an inexpensive and safe route for grid–scale energy storage. However, wide–spread use of RFBs is currently limited due to efficiency and energy density limitations. Due to the ability to tailor the molecular structure to enhance electrochemical performance, ROMs have gained attention as electro–active species for high energy density RFBs. However, literature investigating redox reactions involving ROMs at high concentrations necessary for practical applications is limited.

While this thesis presented the adsorption–desorption mechanism (Chapters 2 and 3) for a model ROM at high concentrations (> 50 mM), deeper insight of the mechanism is needed to inform future efforts in molecular synthesis. Spectroscopic and electrochemical experiments, coupled with molecular dynamics simulations would inform the adsorption site of the ROM. Such insight is critical to mitigating desorption limitations in TEMPO–based ROMs. Moreover, molecular orientation of the adsorbed ROM is presently unknown. With implications on surface coverage and electrochemical reaction rate, such information would be critical for quantifying ROM performance. Further investigation is also necessary to deduce the reaction pathway leading to electrode deactivation (Chapter 4). For example, in a specific case wherein HT^+ adsorbs perpendicularly at the $N^+ = O$ site, the $-OH$ group is oriented away from the electrode and toward the bulk. This could potentially lead to autocatalysis by desorbed HT^+, and therefore deactivate the electrode. In such a case where a passivating film could be formed, X–ray photon spectroscopy could be used to delineate changes in chemical bonding. Insights developed through these activities could also inform the engineering of a

reversible HT/HT^+ electrode. Here, passivation is mitigated such that the adsorbed film remains electro–active. In such a case, the surface concentration of HT^+ is high and electro–reduction is facile, thereby promoting the realization of high energy density RFBs. Furthermore, this work focused exclusively on HT as a representative molecule of the TEMPO family. However, a wide range of ROMs, including phenothiazines and quinones, are currently investigated for both RFB and redox shuttle applications. Mechanistic insights developed by investigating the TEMPO family will further support our understanding of other ROM families.

Additionally, developing such a rigorous understanding of ROMs in well–studied aqueous systems would inform efforts in non–aqueous electrolytes, namely deep eutectic solvents. As discussed in section 1.3 of this thesis, deep eutectic solvents have gained attention as organic electrolytes for RFBs. However, the high viscosity of DESs has limited their commercial adoption. To circumvent viscosity–induced limitations, recent efforts focusing on developing redox–active DESs have been reported.[76] Goeltz and Matsushima reported on a viologen–ethylene glycol DES which undergoes adsorption and dimerization,[76] further highlighting the complex nature of ROM electrochemistry. Here, fundamental understanding of structural changes near the electrode–electrolyte interface during a redox reaction is critical to understanding bulk properties, particularly as it relates to the hydrogen bond network of DESs. Such an understanding could be developed by a combination of *in situ* spectroscopy, simulations, and electrochemical tests.

Appendix A. Hysteresis effects and roughness suppression efficacy of polyethylenimine additive in cu electrodeposition in ethaline

---

A.1. Introduction and motivation

Deep eutectic solvents (DESs) are gaining interest as emerging electrolytes for next–generation energy storage and thin–film deposition applications.[31,32,37] A DES is formed by mixing a hydrogen bond donor with a hydrogen bond acceptor. At the eutectic composition, the mixture exhibits a freezing point depression that renders it liquid–like physical properties under ambient conditions.[32] DESs are advantageous over organic electrolytes due to their large electrochemical stability windows[37] biodegradability[34,77] low–cost of constituent materials,[34] and environmental benignity[32,37] Despite the considerable interest in DESs, practical applications of DESs are limited by their highly viscous nature which manifests in inferior transport properties, *i.e.*, low ionic conductivity and low diffusivity.

Ethaline, a mixture of choline chloride and ethylene glycol (ChCl:EG = 1:2 molar ratio), is a commonly studied DES particularly owing to its low viscosity ($\sim$50 cP at 25°C) compared to other DES mixtures. Physical properties of ethaline are known,[77] and it exhibits an electrochemical stability window of $\sim$2V.[35] A variety of metals including Zn and Ni have been electrodeposited using ethaline as the electrolyte medium.[36,42,78] Cu too has been electroplated successfully with high current efficiencies ($>$ 90%).[38,39] While researchers have studied the effect of electrolyte additives in DESs on the electrodeposition of a variety of metals, including Zn[79] and Ni,[80] a limited number of researchers have investigated the effect of additives on Cu electrodeposition in ethaline.[81]

Metal electrodeposition under conditions approaching the mass transport limit produces morphological changes such as roughness evolution and dendrite formation.[82] Mechanisms underlying roughness evolution were first investigated by Ibl et al.[83] Under practical conditions, micro–scale irregularities or 'roughness elements' are present on an electrode surface undergoing electrodeposition. When deposition is carried out under mass–transport limited conditions, the tips of the roughness elements experience enhanced local plating relative to the recessed portions. This amplifies roughness as plating progresses. While a variety of methods are available to mitigate roughness evolution, ppm levels of additives are routinely included in electrolytes to act as leveling agents.[82,84,85] Polymeric additives with polarizing characteristics such as polyethylene glycol (PEG) and polyethylenimine (PEI) are commonly used in Cu electrodeposition in aqueous media.[84,86] Roha and Landau[87] modeled the steady–state mass transport of leveling agents to an electrode surface during metal electrodeposition. They studied the specific case of a strongly adsorbing additive molecule that is buried into the deposited metal at a rate proportional to the current density. Other modes of electrode potential–dependent additive deactivation have also been proposed.[86,88] The additives adsorption–deactivation processes are known to produce unique features in voltammograms such as hysteresis.

In the present work, Cu electrodeposition in ethaline DES is reported. We investigate the effect of an additive, *i.e.*, branched PEI, on voltammetric response and roughness evolution during electrodeposition. Unlike typical polarizing additives used in electrodeposition in DES,[42,79,80] PEI introduces hysteresis behavior during cyclic voltammetry (CV). A mathematical model describing the interplay between the additive

adsorption–deactivation processes is presented. The model qualitatively explains the observed hysteresis and its relevance to the efficacy of PEI in suppressing roughness evolution during Cu electrodeposition.

A.2. Experimental Procedure

A.2.1. Materials

Ethaline was prepared by mixing choline chloride (ChCl, 99% purity, Acros Organics) and ethylene glycol (EG, anhydrous, 99.8% purity, Sigma–Aldrich) in a $1:2$ molar ratio at $80°C$ for 3 hours until a homogeneous, clear solution formed. The resulting DES was allowed to cool down to room temperature. Cuprous chloride (CuCl, anhydrous, 99% purity, Acros Organics) was added to ethaline to obtain 100 mM Cu^{1+}–containing electrolyte. Branched polyethyelenimine (PEI, average MW: $1300\ g\ mol^{-1}$, 50% w/v in H_2O, Sigma–Aldrich) was added to the electrolyte from a stock solution containing 10,000 ppm PEI in ethaline.

A.2.2. Methods

All electrochemical measurements were performed on a rotating disc electrode (RDE, Pine Research). An electrochemical cell with a 3–electrode configuration was used. The working, counter and references electrodes were connected to a Princeton Applied Research PARSTAT–4000 potentiostat. The Ag/AgCl reference electrode was prepared using a Ag wire (99.9% purity, Rio Grande) anodized in ethaline using the procedure described by Shen et al.[37] The counter electrode was a porous graphite rod (Graphite store). Electrolyte temperature was maintained at $25 \pm 1°C$.

Cyclic voltammograms were collected on a 5 mm diameter Cu RDE working electrode. Prior to each experiment, the exposed Cu surface was polished in a stepwise manner using 600 grit and 1000 grit sandpapers followed by 1 μm and lastly 0.3 μm alumina slurries. The electrode potential was scanned cathodically from the initial equilibrium potential E_{eq} to various switching potentials E_{λ} then returned back to the initial potential. As the electrode potential was scanned, the activation overpotential η_{a} varied as:

$$\eta_{\mathrm{a}} = V_{\mathrm{app}} - IR_{\Omega} - E_{\mathrm{eq}} - \eta_{\mathrm{c}} \qquad [A1]$$

where V_{app} is the applied potential, IR_{Ω} is the ohmic loss due to electrolyte resistance, and η_{c} is the concentration overpotential. The ohmic resistance, R_{Ω} ($= 110\ \Omega$) was measured using electrochemical impedance spectroscopy (EIS), and remained unchanged with the addition of PEI. E_{eq} (-0.187 V vs. Ag/AgCl) was measured under open circuit conditions.

Roughness evolution was quantified using chronopotentiometry in which the Cu RDE was sequentially held at three fixed currents: (i) -0.05 mA for 250 s; (ii) -0.6 mA for 250 s; (iii) -0.05 mA for 250 s. The low current and prolonged time in steps (i) and (iii) allowed for uniform Cu deposition over the electrode, whereas the high current in step (ii) evolved roughness. By comparison of the measured overpotentials in steps (i) and (iii), surface area evolution during step (ii) could be quantified.

A Zygo NewView 7300 optical profilometer was also used to quantify surface roughness. Samples for profilometry were prepared using a silicon wafer substrate (1 cm

diameter) coated with 100 nm of sputter–deposited Cu. Prior to Cu deposition from the DES electrolyte, surface oxides were electrochemically reduced in a 100 mM $HClO_4$ electrolyte. Here, a 3–electrode configuration was used with saturated Ag/AgCl (Fisher Scientific) reference electrode, a porous graphite counter electrode, and the substrate mounted on RDE set at a rotation speed of 500 RPM. The potential of the RDE working electrode was scanned in the cathodic direction from 0 to −1 V vs. Ag/AgCl to reduce surface oxides. The electrode was then removed from the acidic electrolyte, rinsed with 18 MΩ deionized water, and dried with nitrogen before transferring it to the DES electrolyte. Cu was electrodeposited from the Cu^{1+}–containing ethaline at −2.1 mA for 250 s. The substrate was then removed from ethaline, submerged in 18 MΩ deionized water to remove residual ethaline, then dried in a vacuum oven at 30°C for 20 hours. Optical images were collected immediately after drying.

A.3. Results and discussion

A.3.1. Hysteresis during cu electrodeposition from ethaline in the presence of PEI

Fig. A.1 (*red* curves) shows the CV responses obtained under different conditions, *i.e.*, varying PEI concentrations (*left* column), rotation speeds (*middle* column), and switching potentials (E_λ, *right* column). For comparison, the additive free CV responses (in *black*) are also shown. With the addition of 10 ppm PEI, the current during the cathodic (forward) scan direction is lowered compared to the additive free electrolyte indicating surface polarization by PEI. Increasing the PEI concentration to 200 ppm further suppresses the deposition current and polarizes the surface. Interestingly, PEI does not further polarize the surface at 1000 ppm, suggesting that the Cu surface is saturated with

PEI at concentrations in excess of 200 ppm. While the surface is polarized in the cathodic (forward) scan, it exhibits depolarization on the reverse scan, particularly for 200 ppm PEI. This hysteretic signature is absent in the additive free CVs, which suggests that hysteresis caused by PEI is not the result of electrochemically active surface area changes during CV. At very low PEI concentration (*e.g.*, 10 ppm), polarization is weak whereas at high PEI concentrations (*e.g.*, 1000 ppm) polarization is strong but hysteresis is dampened. The switching potential has been shown previously to affect hysteresis.[86] Here too, we observed that the switching potential modulated the degree of hysteresis (*right* column of **Fig. A.1**) with essentially no hysteresis observed when the potential scan was switched at more positive potentials (*i.e.*, lower overpotentials in magnitude) to a gradual increase in the hysteresis as the switching potential was shifted to more negative values. The effect of hydrodynamics on the CV response is shown in the *middle* column of **Fig. A.1**. While the current is suppressed in the cathodic scan direction under all conditions, hysteresis is magnified at moderate rotation speeds (500 RPM); however, the effect of hydrodynamics is convoluted with that of the switching potential since increasing the RDE speed produced higher rates of Cu deposition. This impacts the post–experimentally compensated ohmic drop, and thus shifts the switching overpotential per Eq. A1.

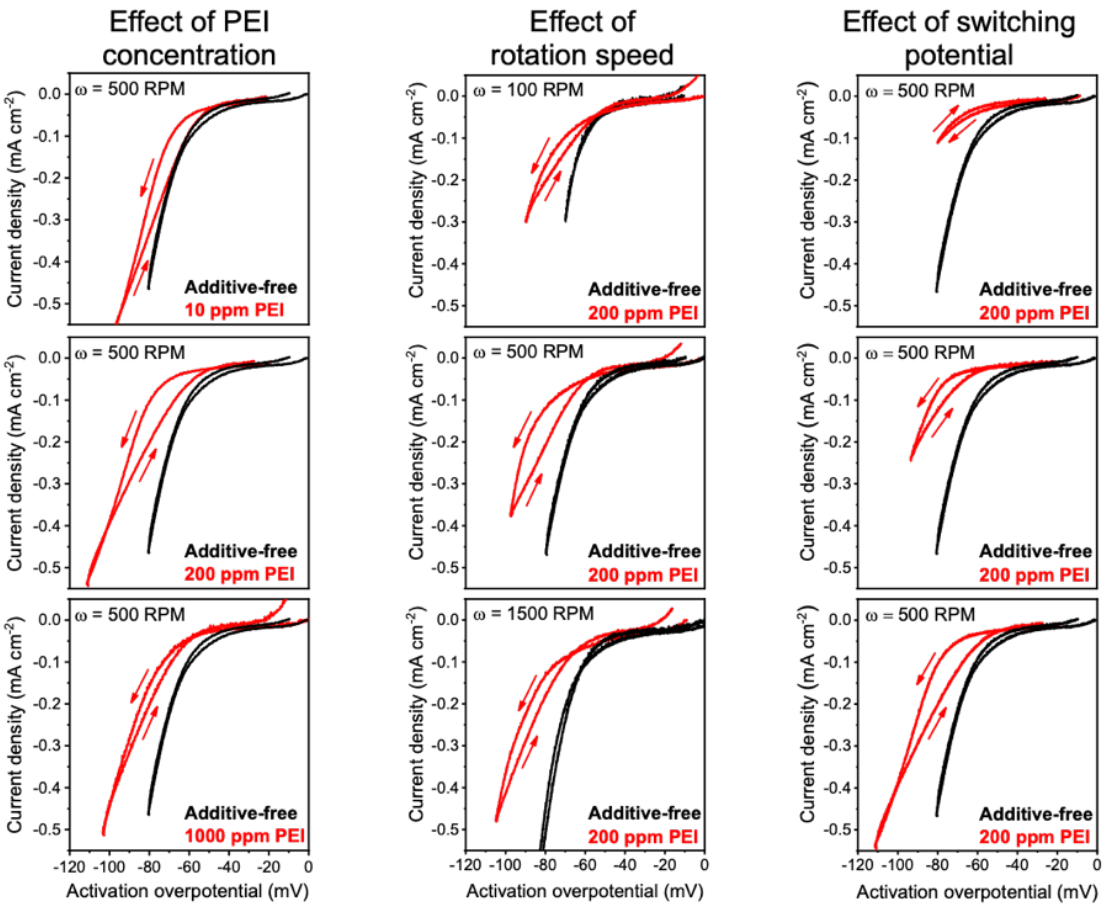

Figure A.1. Cyclic voltammetry (scan rate = 1 mV/s) during Cu electrodeposition on RDE in ethaline electrolyte containing 100 mM Cu^{1+}. CVs obtained in the additive–free electrolyte are shown in black, and those obtained in the PEI–containing electrolyte are in red. The three columns depict the effect of PEI concentration, RDE rotation speed, and switching potential on CV response.

A.3.2. Modeling of PEI transport, adsorption and deactivation processes

To characterize the hysteresis observed in CVs in the presence of PEI (**Fig. A.1**), a quantitative analysis of the PEI adsorption and surface deactivation processes is required. Here, we follow the modeling approach presented by Liu and co–workers[89] for investigating the additive–induced hysteresis behavior in Zn electrodeposition. Following their approach, a mass balance providing the PEI coverage θ of the electrode surface at steady–state may be written as:

$$k_{\mathrm{ads}} C_{\mathrm{b}} (1 - \theta) = k_{\mathrm{deac}} \theta i_{\mathrm{Cu}} \qquad [A2]$$

In Eq. A2, the expression on the left–hand side represents 1$^{\mathrm{st}}$–order adsorption of PEI onto the Cu electrode whereas the expression on the right–hand side represents PEI deactivation. The parameters k_{ads} and k_{deac} represent the PEI adsorption and deactivation rate constants, respectively. The concentration of PEI near the electrode is assumed to be its bulk value (C_{b}). The deactivation rate is assumed to be proportional to the magnitude of the Cu deposition current density (i_{Cu}) and the PEI surface coverage (θ) consistent with the approach taken by Liu et al.[89] The current density i_{Cu} is related to the surface overpotential η and PEI coverage:

$$i_{\mathrm{Cu}} = i_0 (1 - \theta) e^{-b\eta} \qquad [A3]$$

where i_0 is the exchange current density of Cu deposition under additive–free conditions, and b is a constant relating to the Tafel slope. Combining Eqs. A2 and A3:

$$\xi\theta^2 - (1+\xi)\theta + 1 = 0 \qquad \text{[A4]}$$

Eq. A4 is a quadratic in θ in which the dimensionless parameter ξ is defined as the ratio of the PEI deactivation rate to its adsorption rate:

$$\xi = \frac{k_{\text{deac}} i_0 e^{-b\eta}}{k_{\text{ads}} C_{\text{b}}} \qquad \text{[A5]}$$

Eq. A4 has two roots: (i) $\theta = 1$ which is stable only when $\xi < 1$, and (ii) $\theta = \xi^{-1}$ which is stable only when $\xi > 1$. A plot of θ vs. ξ is shown in **Fig. A.2**. In a CV experiment, as the electrode potential is scanned in the negative direction, ξ gradually increases as the overpotential η increases (Eq. A5). The maximum ξ represents the maximum overpotential (η_{max}) reached:

$$\xi_{\text{max}} = \frac{k_{\text{deac}} i_0 e^{-b\eta_{\text{max}}}}{k_{\text{ads}} C_{\text{b}}} \qquad \text{[A6]}$$

From **Fig. A.2**, it is evident that, if ξ_{max} is small ($\xi_{\text{max}} < 1$ because η_{max} is small, or C_{b} is large), the PEI coverage of the electrode remains at $\theta = 1$ implying that the surface remains polarized during the entire CV scan. A small ξ_{max} represents PEI adsorption that is much faster than its deactivation – a condition that would saturate the surface with PEI and not result in hysteresis. If ξ_{max} is large ($\xi_{\text{max}} > 1$ because η_{max} is large, or C_{b} is small), the PEI coverage of the electrode would evolve with the surface potential and eventually reach a low value of ξ_{max}^{-1}. For example, if $\xi_{\text{max}} = 4$, $\theta = 0.25$.

The depolarized surface condition is the result of gradual dominance of the rate of PEI deactivation over its adsorption. This surface coverage evolution manifests as hysteresis during a CV experiment. **Fig. A.2** can be used to explain qualitatively the observations in **Fig. A.1**. For example, the dampening of hysteresis at very high concentrations of PEI (*i.e.*, $C_{\mathrm{b}} = 1000\,\mathrm{ppm}$) is the result of smaller $\xi_{\max}$ per Eq. A6. Furthermore, the gradual amplification of hysteresis as the switching potential is shifted to more negative values (higher $\eta_{\max}$) is again the result of an increase in $\xi_{\max}$ per Eq. A6.

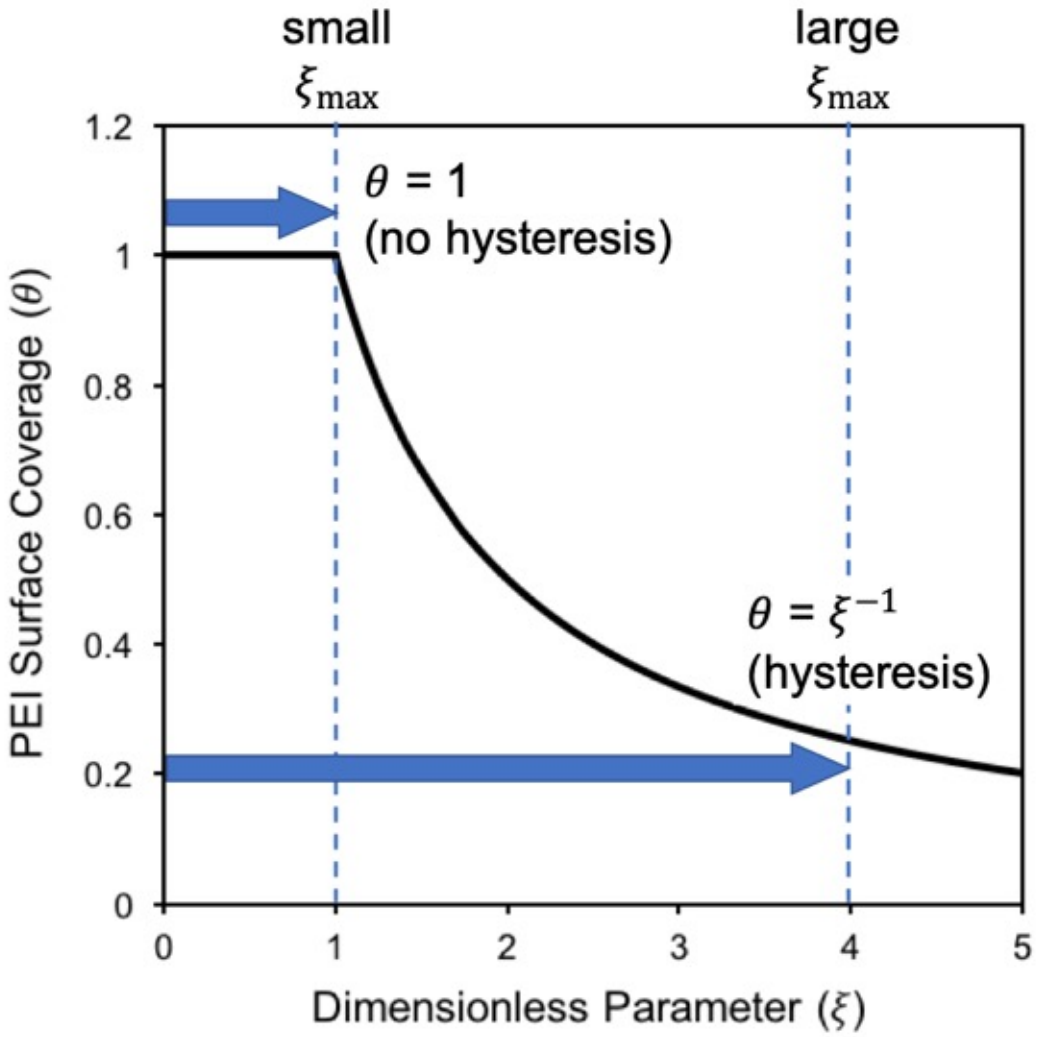

Figure A.2. PEI surface coverage as a function of the dimensionless parameter ξ. When ξ_{max} is low, PEI adsorption dominates over its deactivation and the Cu surface remains saturated (θ = 1) and thus polarized. When ξ_{max} is large, the PEI is deactivated at a rate faster than its adsorption resulting in a low surface coverage.

A.3.3. Effect of PEI on roughness evolution

The above dimensionless parameter ξ (**Fig. A.2**) assists one in understanding how the interaction between PEI adsorption and deactivation rates results in a polarized (large θ) or depolarized (small θ) surface condition. The PEI surface coverage θ is responsible for modulating deposit properties such as roughness. Following the work of Barkey[90] and

Landau,[91] a dimensionless parameter L representing the micro–scale non–uniform current distribution leading to roughness evolution can be defined as:

$$L = \left(\frac{i_{\mathrm{L}} - i}{i_0}\right)\left(\frac{1}{1-\theta}\right) \qquad [A7]$$

In Eq. A7, i_{L} is the limiting current and assumes linear kinetics of Cu deposition with exchange current density i_0. The second term in Eq. A7 represents the surface blocking effect of PEI which can be viewed as an apparent lowering of the deposition exchange current density. Roughness amplification is minimal when $L \gg 1$ and it is significant when $L \ll 1$. Under fixed hydrodynamic conditions and applied current density, roughness can be suppressed by increasing the PEI surface coverage θ.

An electrochemical diagnostic test was performed to better understand conditions that favor polarization (roughness suppression) over depolarization (roughness amplification). The test comprised of galvanostatically depositing Cu using a waveform shown in the top panel of **Fig. A.3**. First, Cu was plated at -0.05 mA for 250 s to uniformly coat the substrate electrode. Next, Cu was deposited at a higher current -0.6 mA for 250 s to evolve roughness. This current was about 75% of the mass–transport limited deposition current. Following this step, current was returned back to -0.05 mA for 250 s to measure the change in the surface overpotential compared to that before evolving roughness. Since the first and the last steps were carried out at a very low current, the micro–scale current distribution is expected to be uniform and any changes in the measured overpotential can be attributed to surface area evolution due to roughness generated in the

intermediate step. The potential response corrected per Eq. A1 resulted in the time evolution of the activation overpotential which is given in **Fig. A.3** for PEI concentrations of 0, 10, 100, and 200 ppm.

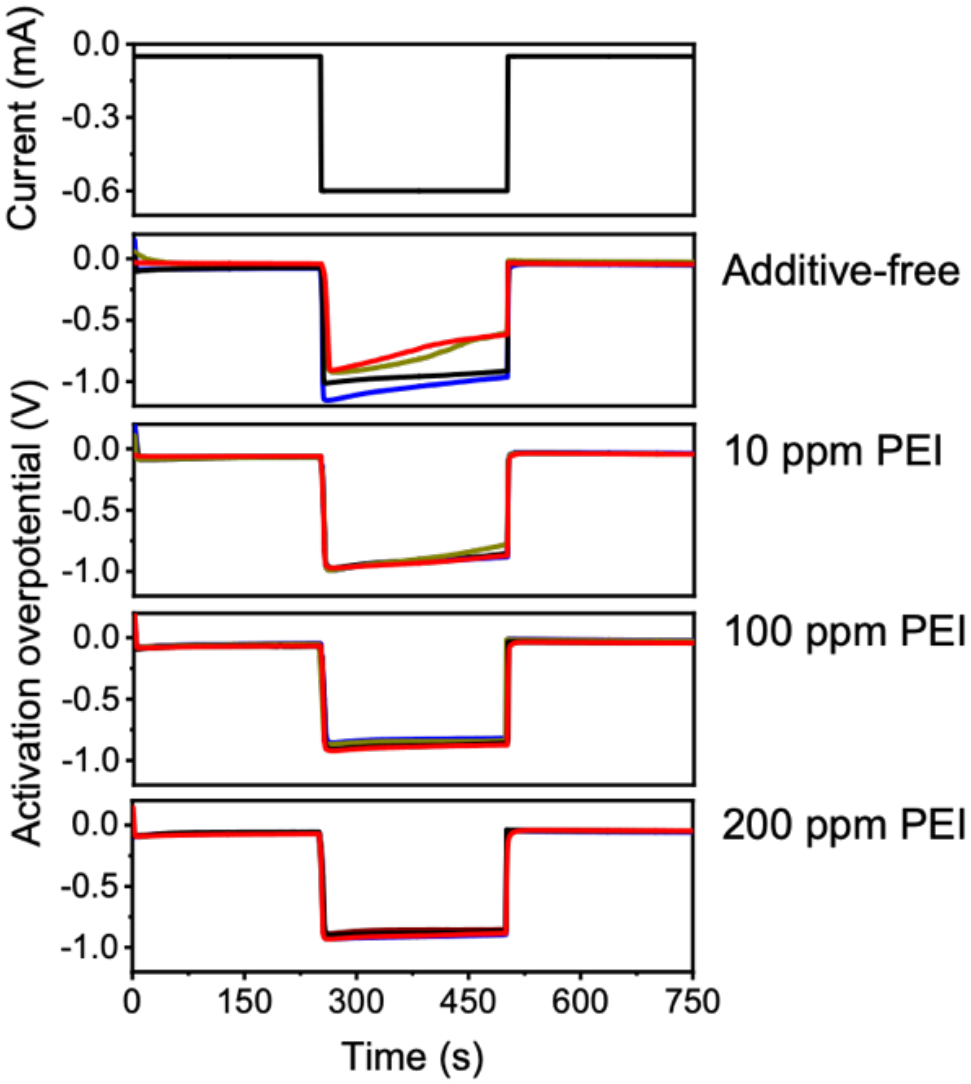

Figure A.3. Potential responses to the applied current step (*top*) during Cu electrodeposition from 100 mM Cu^{1+}–containing ethaline with 0, 10, 100, and 200 ppm PEI on Cu RDE (500 RPM). As the concentration of PEI increases toward 200 ppm, roughness evolution is suppressed. Colors represent multiple trial runs.

We observe in **Fig. A.3** that the activation overpotential during the intermediate roughness development step gradually decreases in the absence of PEI and becomes

relatively constant as the PEI concentration approaches 200 ppm. The changes in η_a with time are indicative of surface area evolution in the absence of PEI. Furthermore, the difference in activation overpotential measured between the first and third step can be used to compute the electrochemically active surface area ratio (*i.e.*, the roughness factor R_f) before and after roughness evolution:

$$R_f = \frac{A_{after}}{A_{before}} = e^{-b\Delta\eta_a} \quad [A8]$$

In Eq. A8, b was taken as $37\ V^{-1}$. This value was determined from polarization data in **Fig. A.1**. Taking $\Delta\eta_a$ from **Fig. A.3**, R_f was calculated for each PEI concentration (**Fig. A.4** *left*). R_f is observed to decrease gradually with increasing PEI concentration. The effect of PEI concentration on deposit roughness was also confirmed via RMS roughness analysis using an optical profilometer (**Fig. A.4** *right*) which also confirmed that roughness decreased with increasing PEI concentration. As the PEI concentration (C_b) increases, ξ decreases per Eq. A5. Since $\theta = \xi^{-1}$, we see that the PEI coverage of the Cu surface increases as PEI concentration increases. In accord with Eq. A7, the dimensionless parameter L increases (*i.e.*, roughness suppression) as θ increases. This explains how increasing PEI concentration lowers roughness during plating (**Fig. A.4**).

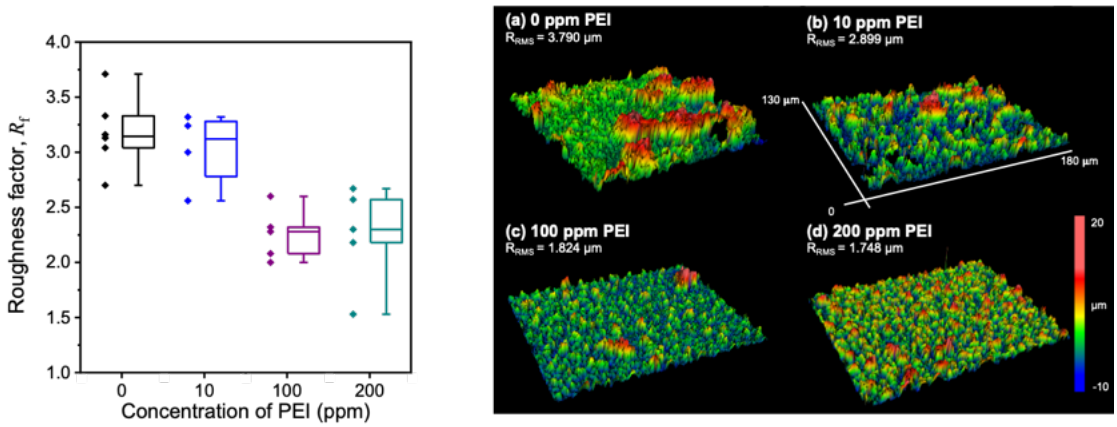

Figure A.4. Effect of PEI concentration on suppressing roughness during Cu deposition from a 100 mM Cu^{1+}–containing ethaline. The points represent individual data points, the whiskers represent 1 standard deviation, the box indicates interquartile range, and the inner bar indicates the median. (*left*) R_f was calculated using Eq. A8 and data in **Fig. A.3**; (*right*) RMS roughness measured using profilometry.

A.4. Conclusions

This study leads to the following conclusions:

(i) Electrolyte additive PEI exhibits hysteresis during CV studies of Cu electrodeposition in ethaline DES. Extent of hysteresis is modulated by the PEI concentration and the switching potential.

(ii) A mathematical model incorporating the PEI adsorption and deactivation processes is presented. The model explains why pronounced hysteresis is seen at low or moderate PEI concentrations and more cathodic switching potentials.

(iii) PEI suppresses roughness amplification during Cu electrodeposition in ethaline DES. Suppression occurs when PEI adsorbs on the Cu surface at a rate that exceeds its deactivation rate, *i.e.*, ξ is small.

Appendix B. Levich analysis to determine diffusion coefficients

---

The diffusion coefficient of electro–active species ($FeCl_3$ and HT) was determined via measurement of the mass–transport limited current density, i_L, and application of the Levich equation:[92]

$$i_L = 0.62\, nFD^{2/3} \left(\frac{\mu}{\rho}\right)^{-1/6} C_b\, \omega^{1/2} \qquad [B1]$$

where F is Faraday's constant (96485 C mol^{-1}), μ is the viscosity and ρ is the density of the electrolyte, and ω is the RDE rotation speed. **Figs. B.1a, B.2a,** and **B.3a** show the limiting current plateaus on a Pt RDE at various rotation speeds. The value of the limiting current density i_L was collected at potentials where the reaction has reached diffusion limitations. The linear dependence of i_L on $\omega^{1/2}$ is shown in **Figs. B.1b**, **B.2b**, and **B.3b**. From the slope of this linear dependence, the diffusion coefficient was calculated for each case. Additionally, on the RDE, the boundary layer thickness δ can be determined by:

$$\delta = 1.61\, D^{1/3} \left(\frac{\mu}{\rho}\right)^{1/6} \omega^{-1/2} \qquad [B2]$$

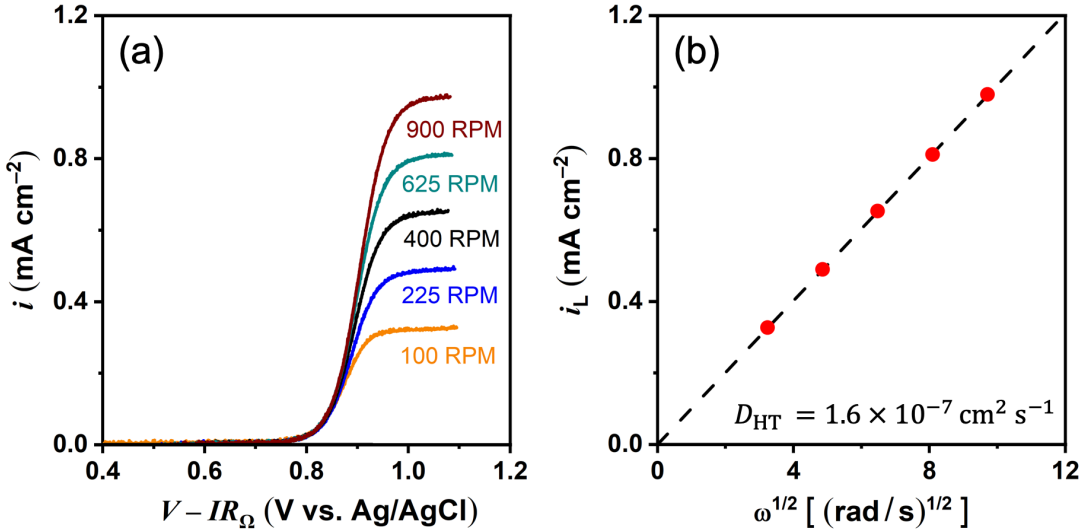

Figure B.1. (a) Slow scan (1 mV/s) linear sweep voltammogram of 50 mM HT in ethaline collected on a Pt RDE; (b) Levich plot showing the linear dependence of the limiting current density i_L on $\omega^{1/2}$. Here μ/ρ = 0.42 cm^2 s^{-1} at 25°C.

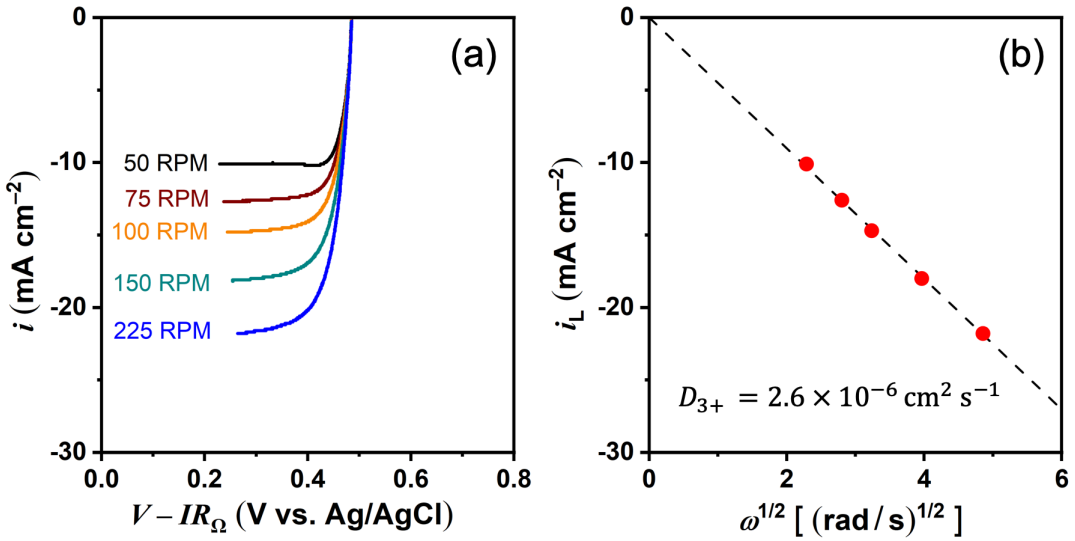

Figure B.2. (a) Slow scan (10 mV/s) linear sweep voltammogram of 200 mM $FeCl_3$ in 500 mM $NaCl_{aq}$ on a Pt RDE; (b) Levich plot showing the linear dependence of the limiting current density i_L on $\omega^{1/2}$. Here μ/ρ = 0.011 cm^2 s^{-1} at 25°C.

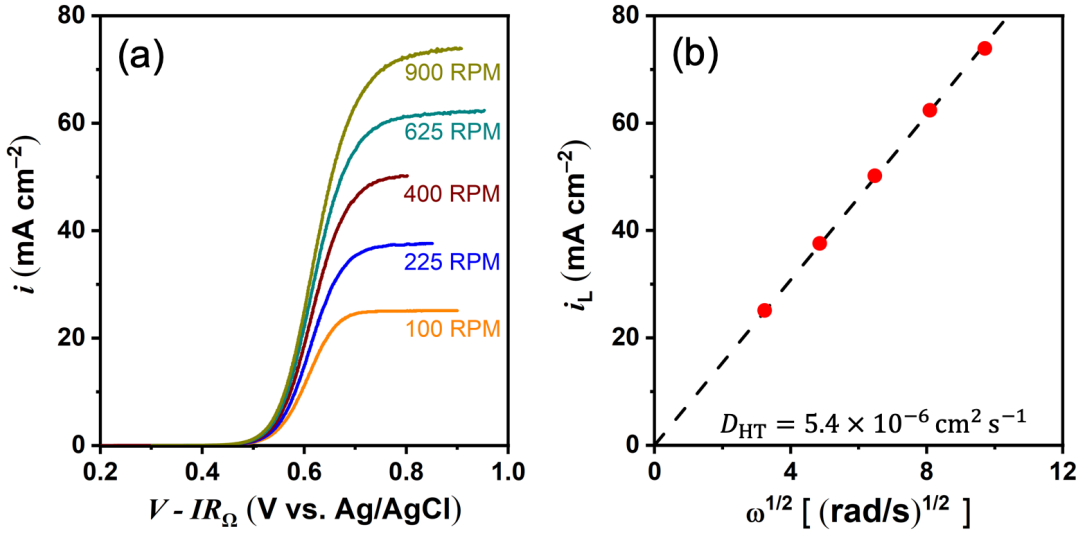

Figure B.3. (a) Slow scan (10 mV/s) linear sweep voltammogram of 200 mM HT in 500 mM $NaCl_{aq}$ on a Pt RDE; (b) Levich plot showing the linear dependence of the limiting current density i_L on $\omega^{1/2}$. Here $\mu/\rho = 0.011$ cm^2 s^{-1} at 25°C.

Bibliography

1. A. Z. Weber, M. M. Mench, J. P. Meyers, P. N. Ross, J. T. Gostick, and Q. Liu, *J. Appl. Electrochem.*, **41**, 1137 (2011).
2. M. O. Bamgbopa, Y. Shao–Horn, and S. Almheiri, *J. Mater. Chem. A*, **5**, 13457 (2017).
3. S. E. Waters, B. H. Robb, and M. P. Marshak, *ACS Energy Lett.*, **5**, 1758 (2020).
4. H. S. Lim, A. M. Lackner, and R. C. Knechtli, *J. Electrochem. Soc.*, **124**(8), 1154 (1977).
5. M. Rychcik and M. Skyllas–Kazacos, *J. Power Sources*, **22**, 59 (1988).
6. S. Kumar and S. Jayanti, *J. Power Sources*, **307**, 782 (2016).
7. D. Aaron, C. N. Sun, M. Bright, A. B. Papandrew, M. Mench, and T. A. Zawodzinski, *ECS Electrochem. Lett.*, **2**, 29 (2013).
8. J. Yu, T. S. Zhao, and D. Pan, *J. Phys. Chem. Lett.*, **11**, 10433 (2020).
9. T. Liu, X. Wei, Z. Nie, V. Sprenkle, and W. Wang, *Adv. Energy Mater.*, **6**, 1501449 (2016).
10. E. V. Carino, J. Staszak–Jirkovsky, R. S. Assary, L. A. Curtiss, N. M. Markovic, and F. R. Brushett, *Chem. Mater.*, **28**, 2529 (2016).
11. N. S. Sinclair, D. Poe, R. F. Savinell, E. J. Maginn, and J. S. Wainright, *J. Electrochem. Soc.*, **168**, 020527 (2021).
12. N. H. Attanayake, Z. Liang, Y. Wang, A. P. Kaur, S. R. Parkin, J. K. Mobley, R. H. Ewoldt, J. Landon, and S. A. Odom, *Mater. Adv.*, **2**, 1390 (2021).
13. W. Duan, R. S. Vemuri, J. D. Milshtein, S. Laramie, R. D. Dmello, J. Huang, L. Zhang, D. Hu, M. Vijayakumar, W. Wang, J. Liu, R. Darling, L. Thompson, K. Smith, J. S. Moore, F. Brushett, and X. Wei, *J. Mater. Chem. A*, **4**, 5448 (2016).
14. T. Janoschka, C. Friebe, M. D. Hager, N. Martin, and U. S. Schubert, *ChemistryOpen*, **6**, 216 (2017).
15. B. Hu, Y. Tang, J. Luo, G. Grove, Y. Guo, and T. Leo Liu, *Chem. Commun*., **54** 6871 (2018).
16. B. Chen, S. Mitchell, N. Sinclair, J. Wainright, E. Pentzer, and B. Gurkan, *Mol. Syst. Des. Eng.*, **5**, 1147 (2020).

17. T. Suga, Y. Pu, K. Oyaizu, and H. Nishide, *Bull. Chem. Soc. Jpn.*, **77**, 2203 (2004).
18. F. Kato, A. Kikuchi, T. Okuyama, K. Oyaizu, and H. Nishide, *Angew. Chem. Int. Ed.*, **51**, 10177 (2012).
19. Y. Liu, M. A. Goulet, L. Tong, Y. Liu, Y. Ji, L. Wu, R. G. Gordon, M. J. Aziz, Z. Yang, and T. Xu, *Chem.*, **5**, 1861 (2019).
20. N. A. Shaheen, M. Ijjada, M. B. Vukmirovic, and R. Akolkar, *J. Electrochem. Soc.*, **167**, 143505 (2020).
21. S. K. Park, J. Shim, J. Yang, K. H. Shin, C. S. Jin, B. S. Lee, Y. S. Lee, and J. D. Jeon, *Electrochem. Commun.*, **59**, 68 (2015).
22. X. Wei, W. Xu, M. Vijayakumar, L. Cosimbescu, T. Liu, V. Sprenkle, and W. Wang, *Adv. Mater.*, **26**, 7649 (2014).
23. D. S. Gnanamuthu and J. V. Petrocelli, *J. Electrochem. Soc.*, **114**, 1036 (1967).
24. B. E. Conway and L. Bai, *J. Electroanal. Chem.*, **198**, 149 (1986).
25. J. O'M. Bockris, *J. Chem. Phys.*, **24**(4), 817 (1956).
26. D. B. Sepa, M. V. Vojnovic, M. Stojanovic, and A. Damjanovic, *J. Electroanal. Chem.*, **218**, 265 (1987).
27. T. Shinagawa, A. T. Garcia–Esparza, and K. Takanabe, *Sci. Rep.*, **5**, 13801 (2015).
28. A. Kahyarian, B. Brown, S. Nesic, *J. Electrochem. Soc.*, **164**(6), H365 (2017).
29. Y. Ding, C. Zhang, L. Zhang, Y. Zhou, and G. Yu, *Chem. Soc. Rev*., **47** 69 (2018).
30. D. Shen, K. Steinberg, and R. Akolkar, *J. Electrochem. Soc*., **165**(14), E808 (2018).
31. D. Lloyd, T. Vainikka, and K. Kontturi, *Electrochim. Acta*, **100**, 18 (2013).
32. E. L. Smith, A. P. Abbott, and K. S. Ryder, *Chem. Rev.*, **114**, 11060 (2014).
33. Y. Wang and H. Zhou, *Energy Environ. Sci.*, **9**, 2267 (2016).
34. Q. Zhang, K. De Oliveira Vigier, S. Royer, and F. Jérôme, *Chem. Soc. Rev*., **41**, 7108 (2012).
35. R. Costa, M. Figueiredo, C. M. Pereira, and F. Silva, *Electrochim. Acta*, **55**, 8916 (2010).
36. A. H. Whitehead, M. Pölzler, and B. Gollas, *J. Electrochem. Soc.* **157**, D328 (2010).
37. D. Shen, M.B. Vukmirovic, R. Akolkar, *J. Electrochem. Soc.*, **166**, E526 (2019).
38. S. Ghosh and S. Roy, *Surf. Coatings Technol.*, **238**, 165 (2014).

39. A. P. Abbott, K. El Ttaib, G. Frisch, K. J. McKenzie, and K. S. Ryder, *Phys. Chem. Chem. Phys.*, **11**, 4269 (2009).
40. N. A. Shaheen, I. Mahesh, M. B. Vukmirovic, and R. Akolkar, *Electrochem. Comm.*, **115**, 106721 (2020).
41. A. D. Ballantyne, R. Barker, R. M. Dalgliesh, V. C. Ferreira, A. R. Hillman, E. J. R. Palin, R. Sapstead, E. Smith, N. J. Steinke, and K. S. Ryder, *J. Electroanal. Chem.*, **819**, 511 (2018).
42. N. M. Pereira, C. M. Pereira, J. P. Araújo, and A. F. Silva, *J. Electroanal. Chem.*, **801**, 545 (2017).
43. J. M. Klein, H. Squire, W. Dean, and B. E. Gurkan, *J. Phys. Chem. B*, **124**, 6348 (2020).
44. X. Shen, N. Sinclair, J. Wainright, and R. F. Savinell, *J. Electrochem. Soc.*, **168**, 056520 (2021).
45. J. O. Bockris, A. K. N. Reddy, and M. Gamboa–Aldeco, Modern Electrochemistry, Kluwer Academic Publishers, New York (2000).
46. J. O'M. Bockris and Z. Nagy, *J. Chem. Educ.*, **50**(12), 839 (1973).
47. E. Laborda, M. C. Henstridge, C. Batchelor–McAuley, and R. G. Compton, *Chem. Soc. Rev.*, **42**, 4894 (2013).
48. J. Koutecky and V. G. Levich, *Zh. Fiz. Khim*., **32**, 1565 (1956).
49. A. J. Bard and L. R. Faulkner, Electrochemical Methods Fundamentals and Applications, John Wiley & Sons, New York (2001).
50. J. O'M. Bockris, I. A. Ammar, and A. K. M. S. Huq, *J. Phys. Chem.*, **61**, 879 (1957).
51. J. O'M. Bockris and T. Otagawa, *J. Phys. Chem.*, **87**, 2960 (1983).
52. P. Karabinas and D. Jannakoudakis, *J. Electroanal. Chem.*, **160**, 159 (1984).
53. J. W. Johnson, H. Wroblowa, and J. O'M. Bockris, *Electrochim. Acta,* **9** 639 (1964).
54. W. Schmickler and E. Santos, Interfacial Electrochemistry, Springer–Verlag, Berlin (2010).
55. R. Guidelli, R. G. Compton, J. M. Feliu, E. Gileadi, J. Lipkoswki, W. Schmickler, and S. Trasatti, *Pure Appl. Chem.*, **86**(2), 245 (2014).
56. A. Ševčik, *Collect. Czech. Chem. Commun*., **13**, 349 (1948).

57. J. E. B. Randles, *Trans. Faraday Soc.*, **44**, 327 (1948).
58. R. S. Nicholson and I. Shain, *Anal. Chem.*, **36**, 706 (1964).
59. I. Fried and P. J. Elving, *Anal. Chem.*, **37**(7), 803 (1965).
60. P. H. Daum and C. G. Enke, *Anal. Chem.*, **41**(4), 653 (1969).
61. N. C. Hung and Z. Nagy, *J. Electrochem. Soc.*, **134**(9), 2215 (1987).
62. J. Newman, *J. Electrochem. Soc.*, **113**(12), 1235 (1966).
63. A. C. West and J. Newman, *J. Electrochem. Soc.*, **136**(1), 139 (1989).
64. E. A. Stricker, K. W. Kreuger, R. F. Savinell, and J. S. Wainright, *J. Electrochem. Soc.*, **165**, A1797 (2018).
65. M. B. Vukmirovic, R. R. Adzic, and R. Akolkar, *J. Phys. Chem. B*, **124**, 5465 (2020).
66. N. A. Shaheen, W. Dean, D. Penley, B. Kersten, J. Rintamaki, M. B. Vukmirovic, B. E. Gurkan, and R. Akolkar, *J. Electrochem. Soc.*, **169**, 053511 (2022).
67. O. Guselnikova, P. Postnikov, S. R. A. Marque, V. Švorčík, and O. Lyutakov, *Sens. Actuators B Chem.*, **300**, 127015 (2019).
68. Z. Galus and R. N. Adams, *J. Phys. Chem.*, **67**, 866 (1963).
69. L. Kiss, D. Bösz, F. Kovács, H. Li, G. Nagy, S. Kunsági–Maté, *Polym. Bull.*, **76**, 5849 (2019).
70. S. Ahmed, M. Ahmad, and S. B. Butt, *Res. Chem. Intermed.*, **38**, 705 (2012).
71. A. Safavi, N. Maleki, and F. Tajabadi, *Analyst*, **132**, 54 (2007).
72. C. Morat and A. Rassat, *Tetrahedron*, **28**, 735 (1972).
73. L. Rintoul, A. S. Micallef, S. E. Bottle, *Spectrochim. Acta – A: Mol. Biomol.*, **70**, 713 (2008).
74. X. Hou, Z. Zhang, K. Shen, S. Cheng, Q. He, Y. Shi, D. Y. W. Yu, C. Y. Su, L. J. Li, and F. Chen, *J. Electrochem. Soc.*, **166**(12), A2419 (2019).
75. M. Rafiee, K. C. Miles, and S. S. Stahl, *J. Am. Chem. Soc.*, **137**, 14751 (2015).
76. J. C. Goeltz and L. N. Matsushima, *Chem. Commun.*, **53**, 9983 (2017).
77. G. García, S. Aparicio, R. Ullah, and M. Atilhan, *Energy Fuels*, **29**, 2616 (2015).
78. A. P. Abbott, A. Ballantyne, R. C. Harris, J. A. Juma, K. S. Ryder, and G. Forrest, *Electrochim. Acta* **176**, 718 (2015).

79. A. P. Abbott, J. C. Barron, G. Frisch, K. S. Ryder, and A. F. Silva, *Electrochim. Acta*, **56**, 5272 (2011).
80. A. P. Abbott, A. Ballantyne, R. C. Harris, J. A. Juma, and K. S. Ryder, *Phys. Chem. Chem. Phys.*, **19**, 3219 (2017).
81. C. D. Gu, Y. H. You, X. L. Wang, and J. P. Tu, *Surf. Coatings Technol.*, **209**, 117 (2012).
82. S. J. Banik and R. Akolkar, *J. Electrochem. Soc.*, **160**, D519 (2013).
83. N. Ibl, P. Javet, and F. Stahel, *Electrochim. Acta*, **17**, 733 (1972).
84. S. J. Banik, K. K. Rao, and R. Akolkar, *J. Electrochem. Soc.*, **163**, E241 (2016).
85. L. Oniciu and L. Mureşan, *J. Appl. Electrochem.*, **21**, 565 (1991).
86. T. P. Moffat, J. E. Bonevich, W. H. Huber, A. Stanishevsky, D. R. Kelly, G. R. Stafford, and D. Josell*, J. Electrochem. Soc.*, **147**, 4524 (2000).
87. D. Roha and U. Landau, *J. Electrochem. Soc.*, **137**, 824 (1990).
88. C. Madore, M. Matlosz, and D. Landolt, *J. Electrochem. Soc.*, **143**, 3927 (1996).
89. X. Liu, O. Bolton, and R. Akolkar, *J. Electrochem. Soc.*, **166** D583 (2019).
90. D. P. Barkey, R. H. Muller, and C. W. Tobias, *J. Electrochem. Soc.*, **136**, 2199 (1989).
91. U. Landau, *Proceedings of the Douglas Bennion Memorial Symposium,* PV94–22, The Electrochemical Society (1995) page 77.
92. V. G. Levich, Physicochemical Hydrodynamics, Prentice–Hall, New Jersey (1962).